DEVELOPMENT OF GRAPHENE-BISMUTH TELLURIDE BASED NANOSTRUCTURED MATERIALS FOR THERMOELECTRIC ENERGY HARVESTING

Dissertation submitted in partial fulfillment of the requirements for the degree of

Doctor of Philosophy (Ph.D.)

in

MATERIALS ENGINEERING

Submitted by

NAVEEN NISCHAL PILLALA

Reg. No. 11ETMM10

Under the guidance of

Dr. RAJ KISHORA DASH

SCHOOL OF ENGINEERING SCIENCES AND TECHNOLOGY

UNIVERSITY OF HYDERABAD

HYDERABAD, INDIA-500046

DECLARATION

I hereby declare that the work reported in this Ph.D. dissertation entitled **"Development of graphene-bismuth telluride based nanostructured materials for thermoelectric energy harvesting"** submitted to **University of Hyderabad** for the award of Doctor of Philosophy in **Materials Engineering** is original and wascarried out by me during my tenure as a Ph.D. scholar under the supervision of **Dr. Raj Kishora Dash**, Associate Professor, School of Engineering Sciences and Technology, University of Hyderabad, India. This dissertation has not formed the basis for the award of any degree, diploma, associateship, membership or similar title of any university or institution. Finally, plagiarism of this dissertation has been checked and satisfied the requirements.

Naveen Nischal Pillala
School of Engineering Sciences and Technology
University of Hyderabad
Hyderabad 500046, India

Place:

Date:

CERTIFICATE

This is to certify that the dissertation entitled **"Development of graphene-bismuth telluride based nanostructured materials for thermoelectric energy harvesting"** submitted by **Naveen Nischal Pillala**,bearing registration number **11ETMM10**in partial fulfilment of the requirements for the award of **Doctor of Philosophy** in the **School of Engineering Sciences and Technology** is a bonafide work carried out by him under my supervision and guidance.

This dissertation is free from plagiarism and has not been submitted previously in part or in full to this or any other University or Institute for the award of any degree or diploma.

Outcome of the dissertation

A. Parts of this dissertation have been published in the following publications:

1. **Naveen Nischal Pillala***et al*, J. of Crystal Growth, 533(**2020**)125474.

B. Parts of this dissertation have been presented at the following conferences:

1. **Naveen Nischal Pillala***et al.*, presented ''Study of structure and morphology of graphene oxide/reduced graphene oxide-based Bi_2Te_3 nano-composites'' at ICANN-2015, IIT Guwahati, Guwahati.

2. **Naveen Nischal Pillala** *et al.*, presented ''Influence of graphene oxide/reduced graphene oxide on the structure, morphology and band gap of go/rgo-Bi_2Te_3 nanocomposites'' at CEMAT-2016 IISc Bangalore, Bangalore.

3. **Naveen Nischal Pillala***et al.*, Presented poster ''Fabrication of r-GO bismuth telluride nano-composites for energy harvesting applications'' at ICFM-2016, IIT- Kharagpur, Kharagpur.

4. **Naveen Nischal Pillala***et al.*, Presented ''Development of 1D Bi_2Te_3 thermoelectric nanocomposites for energy harvesting applications'' at A.P. Science Congress-2017, Andhra University, Vishakapatnam.

The student has passed the Research Methodology course towards the fulfilment of the requirement for Ph.D. work.

Course Code	Name	Credits	Pass/Fail
MT601	Research Methodology	4.00	Pass

Further, the student has passed the following courses towards the fulfilment of coursework requirement for Ph.D.

Course Code	Name	Credits	Pass/Fail
MT401	Thermodynamics and Phase Equilibria	4.00	Pass
MT402	Concepts of Materials Science	4.00	Pass
MT403	Metal forming: Science and Technology	4.00	Pass
MT404	Characterization of Materials	4.00	Pass
MT405	Seminar	2.00	Pass
MT406	Design & Selection of Engineering Materials	4.00	Pass
MT407	Advanced Engineering Mathematics	2.00	Pass
MT408	Materials Processing & Characterization Lab	4.00	Pass
MT451	Materials & Technologies for Energy Systems	4.00	Pass
MT452	Diffusion, Phase Transformations & Kinetics	4.00	Pass
MT453	Modelling and Simulation	4.00	Pass
MT454	Powder Metullurgy & Ceramics	4.00	Pass
MT455	Surface Engineering	4.00	Pass
MT456	Polymer Science and Technology	2.00	Pass
MT457	Laboratory	4.00	Pass
MT458	Seminar	2.00	Pass
MT460	Dissertation	18.00	Pass

Supervisor

(Dr. RajKishora Dash)

DEAN

(School of Engineering Sciences and Technology)

ACKNOWLEDGEMENTS

I would like to express my sincere thanks to my supervisor, Dr Raj Kishora Dash for his continuous encouragement and support throughout my research work, without whom this would not be completed. His guidance helped me to acquire knowledge in doing this research work. I am very grateful to him for leading me to fulfil my Ph.D. degree.

I would also like to thank Prof. Rajender Singh, former Dean, School of Engineering Sciences and Technology (SEST), Prof. M Ghanashyam Krishna former Dean, School of Engineering Sciences and technology (SEST), and Prof. Dibakar Das Dean, School of Engineering Sciences and technology (SEST) for their extended support to me.

I also express my sincere gratitude to all the faculty members of School of Engineering Sciences and Technology for their sharing of knowledge and support.

I also want to acknowledge all the lab technicians from SEST, Center for nano-technology and school of physics for their extended support in carrying out this research work.

I especially thank my lab mate Balaji K for his support in the research work and also Demudu Babu D, Debobrat B, Bikash B, Vasundara G, Rajitha G and Swati S for sharing their ideas and co-operation while working with them. I also wish all the best for their future endeavours.

I would also like to thank all my classmates and friends of SEST who are always there to share, discuss any sort of problems during course work and also in research work. I wish them all the best for their future laurels.

At the end I would especially thank and dedicate this thesis work to my Grandfather and my parents for their continuous support to me.

Naveen Nischal Pillala

CONTENTS

LIST OF FIGURES

Fig. 3.10. Comparative TEM images of (a-c) 0.8-NW neat Bi_2Te_3 NWs and the corresponding GO/rGO-Bi_2Te_3-nanostructured material, (d-f) 3.2-NT neat Bi_2Te_3 larger diameter nanotubes and the corresponding GO/rGO-Bi_2Te_3-nanostructured material and (g-i) 8-NT neat Bi_2Te_3 smaller diameter nanotubes and the corresponding GO/rGO-Bi_2Te_3-nanostructured material synthesized by the mechanical alloying method.1

Fig.3.11EDS spectra of (a) 0.8NW-GO-BM1, (b) 0.8NW-rGO-BM2, (c) 3.2NT-GO-BM3, (d) 3.2NT-rGO-BM4, (e) 8NT-GO-BM5 and (f) 8NT-rGO-BM6 samples synthesized by mechanical alloying method.

Fig.3.12 EDS regions of (a-c) the 0.8-NW-Neat Bi_2Te_3 NWs and the corresponding GO/rGO-Bi_2Te_3 nanocomposites, (d-f) the 3.2-NT-Neat Bi_2Te_3 larger diameter nanotubes and the corresponding GO/rGO-Bi_2Te_3 nanocomposites and (g-i) the 8-NT-Neat Bi_2Te_3 smaller diameter nanotubes and the corresponding GO/rGO- Bi_2Te_3- nanocomposites synthesized by mechanical alloying method.

Fig. 3.13 Raman spectrum of synthesized (a) 0.8-NW neat Bi_2Te_3 NWs and the corresponding GO/rGO-Bi_2Te_3-nanocomposites, (b) 3.2-NT neat Bi_2Te_3 larger diameter nanotubes and the corresponding GO/rGO-Bi_2Te_3- nanocomposites and (c) 8-NT neat Bi_2Te_3 smaller diameter nanotubes and the corresponding GO/rGO-Bi_2Te_3-nanocomposites synthesized by the mechanical alloying method.(d) neat Bi_2Te_3 synthesized at 0.8 mL, 3.2 mL and 8 mL RA (20-200 cm^{-1} range).

Fig. 3.14 Typical FT IR spectra of the synthesized (a) 0.8-NW neat Bi_2Te_3 NWs and the corresponding GO/rGO-Bi_2Te_3-nanocomposites, (b) 3.2-NT neat Bi_2Te_3 larger diameter nanotubes and the corresponding GO/rGO-Bi_2Te_3-nanocomposites and (c) 8-NT neat Bi_2Te_3 smaller diameter nanotubes and the corresponding GO/rGO-Bi_2Te_3- nanocomposites synthesized by mechanical alloying method.

Fig. 4.1 Flow chart for the synthesis procedure of GO/rGO doped bismuth telluride nanomaterials.

Fig. 4.2 X-ray diffraction pattern of (a) 0.8NW- Bi_2Te_3 (neat), CD2, CD1 and (b) 0.8NW- Bi_2Te_3 (neat), CD4, CD3samples.

LIST OF TABLES

List of acronyms, abbreviations and units of measure

- Å-- Angstrom
- Bi – Bismuth
- Bi_2Te_3 – Bismuth Telluride
- Bi $(NO_3)_3.5H_2O$ – Bismuth Nitrate Pentahydrate
- C-rGO – Chemically reduced –reduced graphene oxide
- CNT – Carbon Nanotubes
- CVT – Chemical Vapor Transport
- DI water – Deionized water
- EDS – Energy Dispersive Spectroscopy
- FESEM – Field Emission Scanning Electron Microscopy
- FTIR – Fourier-Transform Infrared Spectroscopy
- GO – Graphene Oxide
- gm – Gram
- H_2SO_4 – Sulphuric Acid
- H_2O_2 – Hydrogen peroxide
- HCL – Hydrocholric acid
- hr – Hour
- HRTEM – High Resolution Transmission Electron Microscopy
- H.H – Hydrazine Hydrate
- ID – Identity
- I-V – Current - Voltage
- I_d/I_g ratio – Intensity ratio of D band and G band
- K -- Kelvin
- $KMnO_4$ – Potassium Permanganate
- Min – Minute
- mL – Millilitre
- mg – Milligram
- MW – Molecular weight
- Mmol – Millimole

- mm – Millimetre
- µm – Micrometre
- mV – Milli Volt
- µV – Micro Volt
- $NaNO_3$ – Sodium nitrate
- NaOH – Sodium hydroxide
- NW – Nanowires
- NT – Nanotubes
- NR – Nanorods
- nm – Nanometre
- N_2 – Nitrogen
- pH – Potential for Hydrogen
- rGO – Reduced Graphene Oxide
- rpm – rotations per minute
- RT – Room temperature
- RA – Reducing agent
- SAED – Selected Area Electron Diffraction
- SEM – Scanning electron microscopy
- SWCNT – Single walled Carbon Nanotubes
- Th-rGO – Thermally reduced reduced Graphene oxide
- TC – Thermal conductivity
- Te -- Tellurium
- TeO_2 – Tellurium Dioxide
- TE – Thermoelectric
- TEM – Transmission electron microscopy
- Wt % -- Weight percentage
- XRD – X-Ray Diffraction
- ZT – Figure of merit
- 1D – One Dimensional
- 2D – Two Dimensional
- °C – Celsius or Centrigrade

List of publications/Conferences

1. K Balaji, **Naveen Nischal Pillala** and Raj Kishora Dash, "Influence of the reducing agent on the formation and morphology of the bismuth telluride nanostructures by using template assisted chemical process: From nanowires to ultrathin nanotubes", J. of Crystal Growth, 533(**2020**)125474.
2. **N. N. Pillala**, D. Dommisa and R. K. Dash,"Influence of morphology of the source bismuth telluride nanomaterials on the thermophyscial properties of the cold pressed graphene oxide(GO) and reduced graphene oxide(rGO) incorporated bulk nanostructured thermoelectric materials(submitted, IOP- Nanotechnology)
3. **Naveen Nischal Pillala,** Demudu Babu, K Balaji, and Raj Kishora Dash, "In-situ Chemical Doping of Graphene Oxide/Reduced Graphene Oxide-bismuth telluride based one dimensional Thermoelectrics''(Manuscript submitted J of Mat. Sc.: Materials in Electronics).

Conferences

1. ''Study of structure and morphology of graphene oxide/reduced graphene oxide-based Bi_2Te_3 nano-composites'' ICANN-2015, IIT Guwahati, Guwahati, 8^{th} -11^{th} Dec 2015.
2. ''Influence of graphene oxide/reduced graphene oxide on the structure, morphology and band gap of go/rgo-Bi_2Te_3 nanocomposites'' CEMAT-2016 IISc Bangalore, Bangalore, 18^{th}-19^{th} July 2016.
3. ''Fabrication of r-GO bismuth telluride nano-composites for energy harvesting applications'' ICFM-2016, IIT- Kharagpur, Kharagpur, 12^{th} -14^{th} Dec 2016.
4. ''Development of 1D Bi_2Te_3 thermoelectric nanocomposites for energy harvesting applications'' A.P. Science Congress-2017, Andhra University, Vishakapatnam, 7^{th} -9^{th} Nov 2017.

ABSTRACT

Recently, it has been notified that there is a shortage of fossil fuels in the near future and an alternative source of fuel is required to overcome the future energy crisis. In this context, subsequent research efforts have been carried out around the globe such as hydroelectric, solar power, fuel cell and so on. Among all, thermo-electric based devices are a promising area of research and have shown advantages for being used as an alternative source of energy for portable devices such as laptops, cell phones, electronic devices and so on. Thermoelectric devices are based on the energy conversion from the waste heat energy to electrical energy by using the Seebeck phenomena. Also such devices don't emit any harmful gases and work without any moving parts. Thus these devices are more eco-friendly, portable, compact and self-reliable and can be directly utilized for portable electronic devices, smart devices and medical appliances.Though significant research is being carried out by different research groups, still the main drawback is the low energy conversion efficiency which is generally expressed in the figure of merit(ZT).

Recently, it has been suggested that low dimensional thermoelectric materials such as nanowires, nanorods, nanoparticles have the ability to improve the figure of merit (ZT) by decoupling the Seebeck Coefficient, electrical conductivity and thermal conductivity. It has been also demonstrated that fabrication of nanocomposites by using the conducting nanofillers such as nanoparticles, nanorods, nanowires, CNT and graphene improve the thermoelectric energy conversion efficiency(ZT). Nanofiller helps to increase the electrical conductivity and at the same time reduce the thermal conductivity due to phonon blocking phenomena.

In this research work, the first part of the thesis work mainly involves with the preparation of the three different bismuth telluride 1D nanomaterials and graphene oxide(GO). Different types of 1D bismuth telluride nanomaterials such as nanowires, larger and smaller size nanotubes were synthesized by using a wet chemical method by adjusting the amount of reducing agent. Graphene oxide(GO) was synthesized by modified Hummers method and then reduced to obtain

reduced graphene oxide(rGO) by thermal and chemical reduction. All the synthesized nanomaterials were analyzed by using different characterization methods such as XRD, RAMAN and TEM for structural, molecular and morphology analysis. The experimental results evidenced that few layers of GO and three different morphologies of the bismuth telluride(Bi_2Te_3) nanostructures such as nanowires, larger diameter nanotubesand smaller diameter nanotubes were successfully obtained those were later utilized as fillers for preparation of GO/bismuth tellrude and rGO/bismuth telluirde based nanocomposites.

The second part of this thesis work presents the synthesis and characterizations of a set of GO/bismuth telluride and rGO/bismuth telluride nanocomposites by using the mechanical alloying process by varying the amount of GO and rGO. The obtained different morphologies 1D bismuth telluride nanomaterials such as nanowires, smaller diameter and larger diameter nanotubes were employed as source materials to investigate the impacts of morphologies of the starting 1D nanomaterials on the structural, molecular and morphologies of the obtained GO/bismuth telluride and rGO/bismuth telluride nanocomposites. The experimental analysis results from FESEM and TEM indicated that a high energetic ball-milling process breaks the larger diameter nanotubular structures during the process and possibly help to establish a strong contact between the nanofiller and matrix material as compared to the nanotubes with a smaller diameter. However, the nanowire or smaller diameter nanotubular structures are mostly decorated on the surface of the reduced graphene oxide that leads to no-perfect contact between the filler and matrix material. The thermo-physical properties of the fabricated GO/bismuth telluride and rGO/bismuth telluride nanocomposites were carried out later part of this thesis work.

In the next part of this work, GO and rGO doped bismuth telluride nanostructures were synthesized by using the in-situ chemical rational approach. For this purpose, two different amounts of GO and rGO such as 5 mg and 10 mg were used as dopants to investigate the impacts of chemical doping process on the structure, morphology and composition of the GO and rGO doped bismuth telluride nanostructures. TEM and FESEM analysis results revealed that different morphologies 1D TE nanomaterials such as nano-screws, nanoplates/nanowires, and rough

surface thick wall nanotubes are obtained by controlling the concentration of the GO and rGO. XRD and Raman analysis results clearly indicated that GOs are reduced to rGO during the in-situ doping synthesis process. HRTEM analysis also indiacted the embedment of GO/rGO in the matrix bismuth telluride nanostructures. FT IR analysis results further indicate the formation of GO/rGO-bismuth telluride nanomaterials.

The final part of this work presents the investigation of the thermo-physical properties such as Seebeck coefficient, thermal conductivity(k) and electrical conductivity of all synthesized neat bismuth telluride samples such as 0.8NW, 3.2NT, 8NT and the obtained GO and rGO based bismuth telluride nanomaterials prepared by mechanical alloying and in-situ doping process to ensure the best synthesis process to obtain the high figure of merit(ZT). The impacts of different morphological bismuth-telluride 1D nanomaterials as a source materials on the thermo-physical properties were also studied. All the obtained samples in the powder form were cold-pressed into disk-shaped pellets. Our experimental findings suggested that the inclusion of the higher amount of rGO either by ball-milling or in-situ chemically doping process improves the figure of merit(ZT). Furthermore, the experimental results indicated that the morphological(nanowires, smaller or larger nanotubes) of the source bismuth telluride has a vital role in the thermo-physical properties. The inclusion of rGO with the bismuth telluride opens a pathway for improving the figure of merit by decreasing the lattice thermal conductivity,simultaneously improving the electrical conductivity. However, more research efforts still require by using different pellet preparation processes to improve the electrical conductivity so that a high-value figure of merit(ZT) can be achieved.

Chapter 1

Introduction

Chapter 1

Introduction

1.1 Introduction

The necessity for cleaner and sustainable energy is increasing day by day due to the exhaustion of fossil fuel supply and also due to the global warming effect[1]. Therefore, an alternative way of energy source is required to fulfill the shortage of energy in the future. Though several approaches have been carried out globally such as hydroelectricity, biofuel etc. more focus is to investigate different methods to generate cleaner and sustainable energy. Among all, thermoelectric based devices have shown great promise for producing electricity by conversion of heat energy to electrical energy[2][3][4][5]. Thermoelectric devices are solid-state energy convertors of thermal energy to electrical energy without any moving parts and harmful gas emissions, eco-friendly, portable, compact and self-reliable[6][7][8] and can be directly utilized for portable devices, smart devices and medical appliances[9].

Thermoelectric effect

The direct conversion of thermal energy to electrical energy by inducing temperature difference in a material is called a thermoelectric effect. The materials those have potential to convert heat energy to electrical energy by inducing temperature difference are known as thermoelectric materials(TE)[10]–[20] such as Bismuth telluride[21], Antimony telluridecomposites[22], Bismuth Bi,Selenium(Se) and Tellurium(Te) based composites[23], lead telluride (PbTe) [24], cobalt and antimony (MCoSb) based compounds where M=Hf,Zr[25], antimony-telluride[26]and SiGe[27].

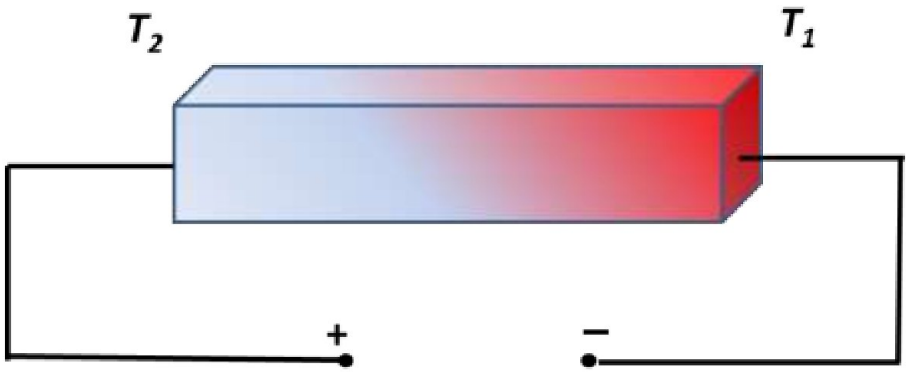

Fig. 1.1. Basic demonstration of Thermoelectric effect in a single material.

The Seebeck effect:

When two different types of thermoelectric materials are joined together as shown in Fig 1.1 and heat is supplied to one end of the material, then it produces a potential difference between the two ends, which is explained by the Seebeck effect[28]. It was discovered by Alessandro Volta in 1794 and later independently rediscovered in 1821 by Thomas Johann Seebeck. The Seebeck effect occurs in a single isolated thermoelectric material when it is subjected to temperature difference in itself. The ratio of generated voltage to the temperature difference is known as the Seebeck coefficient S[29]and is defined as,

$$S = \frac{\Delta V}{\Delta T}$$

Where ΔV is the generated potential difference and ΔT is the temperature difference.

Figure of merit (ZT):

The dimensionless parameter which is defined as the energy conversion efficiency of the thermoelectric material and is expressed as ZT[30][31]. It is given by the equation

$$ZT = \frac{S^2 \sigma T}{k}$$

Where S is the Seebeck coefficient, σ is the electrical conductivity, k is the thermal conductivity and T is operational temperature. The term '$S^2\sigma$' is known as the power factor of the TE material. Thus the efficiency of the thermoelectric material is directly proportional to the power generated or the power factor, that the electrical conductivity of the material should be high so that the energy lost by joule heating can be reduced with high electrical conductivity. Simultaneously the thermal conductivity of the material should be lower so that temperature conduction or the heat conduction can be minimized to maintain the temperature difference in the material. It is also important to consider the temperature at which these parameters are measured as ZT varies with temperature.

Hence a good thermoelectric material should possess high electrical conductivity, high Seebeck coefficient and low thermal conductivity. Semi-conductor materials have a scope of changing the properties with different doping methods without affecting other properties [28]. Therefore, extensive research efforts have been carried out to improve the figure of merit of the TE materials. Though some progress has already been established to obtain bulk thermoelectric materials still, the energy conversion efficiency is very low[32]. Furthermore, very few thermo-electric materials have been reported at room temperature [33][34].

1.2 Literature Review

Recently, it has been demonstrated that low dimensional thermoelectric materials [35] such as nanowires, nanorods, nanoparticles etc. have the ability to improve the figure of merit (ZT) by decoupling the Seebeck Coefficient, electrical conductivity and thermal conductivity[36]. Due to the quantum confinement effect at the nanoscale, it is possible to enhance the density of states that can increase the Seebeck coefficient without degrading the value of electrical conductivity [37]. In addition to this, due to phonon blocking effect, thermal conductivity can be further reduced without decreasing the electrical conductivity[38][39]. In this context, significant research efforts have already been carried out to improve energy conversion efficiency (ZT). By synthesizing nanoscale thermoelectric materials[40]. Few reported nanoscale thermoelectric materials with ZT value are shown in Table 1.

Table. 1 Current literature in TE materials

Author	TE Material	Synthesis Process	Densification Process	K (W/mK)	Peak ZT
Cheng-Lung Chen [41]	Bi_2Te_3 NW thin films	Electro deposition	-	~0.75	0.45 at 300K, 0.9 at 350K
Ming Tan[42]	$(Sb,Bi)_2Te_3$ NW arrays	Evaporation	-	0.93	1.72
Nhlakanipho Mntungwa[43]	Bi_2Te_3 and Bi_2Se_3 Nano crystals	Wet chemical	-	-	-
Han Xu [44]	Composites of Bi_2Te_3 with CNT	Potentiostatic electro deposition	-	-	-
Fang Wu[45]	Bi_2Te_3 nanopowder with Ce, Sm and Y doping	Hydrothermal	Hot pressed	~0.9	1.29 at 398K
Fang Wu [46]	$Bi_2Te_{3-x}–I_x$ nanopowder	Hydrothermal	Hot pressed	~0.8	1.1 at 448K
Kaleem Ahmad [47]	Bi_2Te_3 by incorporating the SWCNT	Ultrasonicationand magnetic stirring	Hot pressed	~0.25	0.55 at 400K
Xin Qi [48]	Bi_2Te_3 Nanoplatelets	Solvothermal	Hot pressed	0.4	-
Thomas Ludwig [49]	Bi_2Te_3 Nanoplatelets	Solvothermal	-	-	-
Y.Q.Cao[50]	Bi_2Te_3 Nanotubes	Aqueous chemical method	-	-	-
Michael Thompson Pettes[51]	Bi_2Te_3 Nanoplates	Vapour –solid growth	-	~1.2	~0.2
Yimin Zhao [52]	Bi_2Te_3 2D Nanosheets	Surface assisted CVT	-	-	-
X. B.Zhao [53]	Bi_2Te_3 Nanotubes	Hydrothermal	-	~0.8	~1
I.Bejenari [54]	Bi_2Te_3 Nanowires	Theoritical	-	-	~ 3.4
Desheng Kong[55]	Bi_2Se_3, Bi_2Te_3 Nanoplates	Vapor-solid	-	-	-
Y.H.Zhang [56]	Bi_2Te_3 Nanopowders	Hydrothermal	Hot pressed	~ 0.9	0.58 at 480K
Fei Ren [57]	Bi-Sb-Te	Ball milling	Hot pressed	~ 1	1.2 at 350K
Y.Q.Cao [58]	$(Bi,Sb)_2Te_3$ bulk Nanostructure	Hydrothermal	Hot pressed	0.9	1.28 at 303 K
Bed Poudel [59]	Nanostructured BiSbTe	Ball milling	Hot pressing	~ 1	1.4 at 373K
Xinfeng Tang[60]	Nanostructured Bi_2Te_3	Melt spinning	Spark plasma sintering	0.58 (K_l)	1.35 at 300 K
Jiaqing He [61]	PbTe–$PbSnS_2$	Hot furnace melting	-	0.8 (K_l)	-
Jiaqing He [62]	PbTe-2%Sb nanoparticle	Hot furnace melting	-	1.4	-
Allon I. Hochbaum [63]	Si Nanowires	Aqueous electroless etching (EE)	-	-	0.6
Kanishka Biswas[64]	Nanostructured SrTe-PbTe	Hot furnace melting	-	~ 1	1.7 at 800K
J. Jaćimović[65]	$ZnMnO_3$Nanoflakes	Melting	Cold-pressed	-	-

Furthermore, it has been also demonstrated that fabrication of nanocomposites by using the conducting nanofillers such as nanoparticles [66], nanorods, nanowires[67], CNT [68] and graphene could improve the thermoelectric energy conversion efficiency by increasing the electrical conductivity and at the same time by reducing the thermal conductivity due to the contribution from the conducting nanofillers and lattice scattering from the increasing number of the interface in the nanocomposites [69].

Recently, graphene incorporated TE materials have drawn significant interest to improve the efficiency of TE materials as it acts as the phonon-blocking barrier as it possesses inferior through-plane thermal conductivity[70][71][72].

Hyun Ju etal., have fabricated hybrid composites with nanowires of n-type Bi_2Te_3 and graphene by arranging ultrathin nanowires of Bi_2Te_3 between the layers of graphene in a layer by layer arrangement. They have taken Bi_2Te_3 nanowires and graphene in solution medium and ultrasonicated to form the hybrid structure, subsequently sintering at varying temperatures such as 573, 623, 673, 723, and 773 K. They have reported that with the increase of sintering temperature, the properties of the hybrid composite like electrical conductivity, grain size, as well as relative density, have also increased by decreasing interfacial density. Consequently, there is a reduction in the Seebeck coefficient and an improved ZT value to 0.25 at 623K[73].

Fangfang Tu et. al., have reported a novel wet chemical approach to synthesize hybrid of Bi_2Te_3-nanoplates and the nanosheets of graphene in a sandwich structure by arranging bismuth telluride nanoplates between two graphene sheets which were prepared previously by Hummer's synthesis procedure[74].

Daewoo Suh etal., have developed a composite of expanded graphene and $Bi_{0.5}Sb_{1.5}Te_3$ by ball milling methods followed by spark plasma sintering. Initially, the $Bi_{0.5}Sb_{1.5}Te_3$ was synthesized by the wet-chemical process. At room temperature, 0.1 vol% of expanded graphene increases both carrier concentration and electrical conductivity up to 44% and 67% respectively, whereas the lattice thermal conductivity has decreased. At 360k, the highest ZT value is reported as 1.13[75].

A.H. Li et. al., have investigated a comparative study of thermoelectric properties and electronic structures for single crystals of $Bi_2Te_3$and graphene doped Bi_2Te_3 polycrystalline material. As compared to the single crystal of Bi_2Te_3, graphene/Bi_2Te_3 material possessed reduced thermal conductivity of 12 mW/cm Kwith an improvement in ZT value 1.5 times greater than Bi_2Te_3 single crystals[76]. *Bin Feng et al.*have synthesized the $CoSb_3$-Graphene nanocomposites by preparing graphene and then adding the Co and Sb precursors to it. They have achieved a peak ZT of 0.6 and the lowest thermal conductivity of around 1.0 W/m-K[77].

Beibei Liang etal., have synthesized Graphene /Bi_2Te_3 composite by the hydrothermal procedure followed by the spark plasma sintering route to investigate the thermoelectric property of the composite materials. They have reported that, by a rise in temperature, the electrical conductivity of the composite has decreased from 1.03×10^5S/m to 0.91×10^5S/m and in similarly thermal conductivity of the composite materials has also decreased with a rise in temperature. At 475K they have achieved the highest ZT of 0.21 for 0.2 vol % graphene concentration present in the composite material[78]

In a similar way, *Cong Li et al.,* have reported the development of graphene nanosheets incorporated into $Bi_{0.4}Sb_{1.6}Te_3$ nanocomposite by wet chemical synthesis approach. At a low concentration of graphene nanosheets, they have shown that a rise in electrical conductivity measured. On the contrary thermal conductivity reduced to 20 to 30%. They have reported the ZT value of 1.29 at 300 k and 1.54 at 440K for 0.3 vol.% and 0.4 vol.% graphene concentration in the composite structure[79]. *Eun Sun Kim et al.*have recently developed the bismuth telluride thin film on graphene substrate with silicon dioxide as an underlying substrate and have achieved significant thermoelectric power factor[80]. *Chang wan lee et al.*havereported bismuth telluride and antimony telluride on graphene substrates with SiO_2 as an underlying substrate and achieved 35μW/cmK[81].

*Jingdu dong et al.*synthesized an in situ developed PbTe-graphene composite by uniformly sonicating graphene in DI water, subsequently adding Pb and Te precursors. They have achieved a low thermal conductivity of 0.6 W/mK[82]. *Hyun Ju et.al.,* have fabricated composites consisting of nanowires of Bi_2Te_3 (diameter of ~15 nm and ~1μm long) and graphene. They formed nanostructured bulk composites by wet chemical routes like ultra-

sonication followed by sintering. 0.5 wt% concentration of graphene generated 688.9 μW/m K^2 thermoelectric power factor as reported[83].

Tsung-Han Chen et al. developed bismuth antimony telluride, carbon thin films on silicon dioxide substrates by a laser ablation process. They have achieved a considerable 40-50 μW/cm K^2 thermoelectric power factor[84].

Weon Ho Shin et al. have shown a melt spinning synthesis route for the fabrication of a composite material consisting of reduced GO and p-type $Bi_{0.36}Sb_{1.64}Te_3$ where reduced GO is uniformly dispersed in the matrix of $Bi_{0.36}Sb_{1.64}Te_3$. They have shown improvement in carrier mobility of the matrix with a 20% enhanced power factor. With an increase of reduced GO concentration, the grain size of the matrix of $Bi_{0.36}Sb_{1.64}Te_3$ reduced as a consequence; the lattice thermal conductivity decreased as there is increased grain boundary scattering. At 393K, for 0.4% reduced GO concentration, the optimum ZT value is 1.16[85].

Bartosz Trawiński et. al., have studied the TE properties of a composite consisted of CNT (0.15 wt %)/amorphous Carbon (0.30 wt %) and a matrix of bismuth telluride synthesized by sonication followed by ball milling method. As a consequence of the addition of CNT, amorphous Carbon in the matrix, the electric conductivity varied from 1120 S/cm to 77 S/cm. And the Seebeck coefficient value ranged from -113 μV/K to 2 μV/K due to the electron trapping by amorphous carbon[86]. *Khushboo Agarwal et al.*mixed pure bismuth telluride and single-layer graphene in an agate mortar and pestle thoroughly and made the composite into pellets for TE property measurement. They have achieved a peak ZT of 0.9 and the lowest thermal conductivity of 0.4 W/mK[87].

Mohamed etal., have synthesized $Bi_{85}Sb_{15}$ /commercial graphene composites with the help of mechanical alloying as well as a hot isostatic pressing route with different concentrations of commercial graphene materials like (wt % of 0.02, 0.04, 0.06, 0.08) and varying temperatures of 173–373 K. At the lowest temperature condition i.e., at 173K the optimum value of the power factor obtained is $3.7 \times 10^{-3} W.m^{-1}.K^{-2}$ for 0.08 wt % of graphene in the composite material[88].

Hyun Ju et al., have fabricated composites of nanostructured graphene/ Bi_2Te_3 with three different ways such as Bi_2Te_3 powder synthesized from beads of Bi_2Te_3 by ball milling process; with nanowires synthesized by solution-phase synthetic approach and also with different

concentrations of graphene. 0.5 wt.% of the concentration of graphene present in graphene/ Bi_2Te_3 composite leads to enhanced power factor, Seebeck coefficients but a reduced electrical conductivity as well as lattice thermal conductivity. At 300 K, for 1wt.% of graphene concentration present in the composite structure has given the optimum ZT value as 0.4 greater than Bi_2Te_3 powder and Bi_2Te_3 nanowires[89].

Jin Il Kim et al., have prepared n-type $Bi_2Te_{2.7}Se_{0.3}$/unoxidized graphene composites by using hydrazine hydrate subsequently followed by plasma-sintering of lamellar microstructure. While studying the thermoelectric property of the composite material it was found that there is a decrease in carrier concentration as well as an increase in Seebeck coefficient and thermal conductivity. The optimum ZT value was found as ~0.8 for 0.05 wt% concentration of unoxidized graphene[90]. *V.D. Blank et al.*mechanically alloyed bismuth antimony telluride and C_{60} materials in a planetary ball milling. They have achieved a peak ZT of around 1.1 and lowered thermal conductivity of around 0.7 W/mK[91].

Hyun Ju et al. have fabricated a hybrid structure of Bi_2Te_3 nanowire/graphene, both one-dimensional n-type nanowires of Bi_2Te_3 and graphene nanosheets individually with the help of wet chemical method and Hummers method respectively. Later Bi_2Te_3 nanowires of 1μm and approximate diameter of 15nm, have been homogeneously dispersed between the layers of graphene (17 μm) by following facile wet chemical synthesis and sintering process where the content of deposited Bi_2Te_3 nanowires on the surface of graphene film is 20 wt.% and 30 wt.%. In this reported nanocomposite, electrical conductivity has decreased from 310 to 247 S/cm with the increase of the content of Bi_2Te_3 nanowire from 0 to 30 wt.% credited to the large characteristic Seebeck coefficient and reduced electrical conductivity of Bi_2Te_3 nanowires ~ 210 S/cm. On an average of 20 wt.% Bi_2Te_3 nanowire content in the composite has shown an improved thermoelectric coefficient (ZT) of 0.2 at room temperature[92].

Dewen Xie et al. havezone-melted as well as spark plasma sintered and have followed to design p-type $Bi_{0.48}Sb_{1.52}Te_3$/ graphene composites. The electrical conductivity of the composite decreased with the increase of temperature from 300 to 550K. With the increase of graphene content, the value of electrical conductivity has decreased. On the contrary, there is an enhanced

power factor of 4.8×10^{-3} $Wm^{-1}K^{-2}$ with the increase of graphene content and an enhancement in the thermoelectric coefficient (ZT) of 1.25 at 320K[93].

Airul Azha et al p- and n-type bismuth telluride has been used to the doped organic hybrid film like PEDOT: PSS–glycerol. Later graphene particles of 0.02 to 0.1 wt% ranges have been used to optimize bismuth telluride–organic hybrid film using the spin coating method. As a result, electrical conductivity performance of the hybrid film enhanced with graphene dopant concentration have shownthe maximum value of 400 and 195 S/cm for both p- and n-type films respectively, at 0.08 wt% of graphene and a further increase of the graphene content showed a reduced value of electrical conductivity. With increasing in the doping concentration, p-type hybrid film possessed prominent enhancement in a thermoelectric property whereas n-type hybrid film exhibited a reversed phenomenon. P-type hybrid thin film exhibited seebeck coefficient and power factor value as 20 μV/K and 160 μW m^{-1} K^{-2}, as well as n type hybrid thin film, exhibited 10 μV/K and 19.5 μW m^{-1} K^{-2} respectively with graphene content 0.08 wt%[94].

Sunil Kumar et al. have studied Nanocomposites of Bi_2Te_3–graphene. They have synthesized the Nanocomposites by following the refluxing method where Bi_2Te_3 nanosheets were priorly synthesized with the help of the hydrothermal method. The graphene sheets were then added to the Bi_2Te_3 nanosheets solution on a refluxing method with atemperature of 373K for 4 hours, cooled and dried. This nanocomposite has shown an enhanced figure of merit (ZT) ~ 53 % with an increase in electrical conductivity of ~111 % by decreasing thermal conductivity of ~12 % after adding graphene[95].

1.3Challenges and current issues for improving the figure of merits in TE materials

Though several strategies have been utilized to improve the figure of merit(ZT) of the TE materials, the recent literature studies indicated that ZT is still very low. Several materials issues are still there and it needs more research efforts to develop highly efficient thermoelectric materials. Also, it has been found from the current literature studies that 2D carbon-based material i.e. graphene has some potential to be utilized as a nanofiller in the host TE materials. Though some progress has already been carried out to use graphene as filler materials, still very

limited literature is available as per our knowledge. Furthermore, there is not much-reported literature available to use graphene as a dopant to prepare graphene doped bismuth telluride thermoelectric materials. Moreover, it has been also found from the literature review that the final sample preparation process and process parameters such as pressure applied for preparation of pellets, directions of applying pressure[96]97][98]and also the sintering process plays a major role in the thermoelectric properties of the fabricated nanostructured TE materials.

Similarly, the orientation of filler nanomaterials in the matrix plays a major role in obtaining the desired properties which is a difficult parameter to control during fabrication/synthesis of the materials. Hence, careful observation and investigation are essential on synthesis procedures, alloying/doping elements by choosing appropriate doping materials and the matrix material with good electrical conductivity and possibly low electronegativity differences between the matrix and dopants. Different methods of sample preparation for characterizing the thermoelectric properties also play a major role i.e. the pressure applied for preparation of pellets, directions of applying pressure [97] and also the sintering methods as the densification happens during sintering and it is very important to carefully select the sintering methods which donot affect the material properties [98].

1.4The motivation of current work

From the literature review on the recent developments of the TE materials, it is found that there is a significant improvement in the figure of merits bynanostructuring[99]–[112]. Several studies were reported in this chapter with various nanostructured or nanomaterials embedded in matrix TE materials to block the phonons. Recently it is found that hybrid materials like graphene-bismuth telluride have the further scope of achieving a higher figure of merits. Also that, all the above-mentioned works on graphene/bismuth telluride composite has focused only on synthesis and variation of filler materials (Graphene/GO/rGO) into the matrix (Bi_2Te_3) or variation of sintering temperatures etc. This has been the motivation behind this current work in order to develop novel ways of synthesis procedures like in-situ doping of GO/rGO into bismuth telluride materials and also investigating the morphological effects of bismuth telluride on GO/rGO-bismuth telluride based nanocomposites.

1.5The objective of current work

The main objective of this research work is to develop graphene-based bismuth telluride (TE)nanostructured materials by using a cold sintering process and to investigate the best approach to achieve efficient TE materials for energy harvesting. For this purpose, two different approaches have been carried out to synthesize the graphene-based bismuth telluridenanomaterials. Firstly, by mechanical ball-milling graphene oxide (GO) and reduced graphene oxide(rGO) with one-dimensional bismuth telluride nanomaterials (nanorods and nanotubes) to prepare GO and rGO incorporated TE nanomaterials and secondly by in-situ chemically doping the graphene oxide (GO)/reduced graphene oxide (rGO) with bismuth telluride.

Finally, a comparative study of the impacts of the morphology of the starting bismuth telluride nanomaterials on the thermal conductivity, electrical conductivity and Seebeck coefficient of all the GO/rGO incorporatedand GO dopped bismuth telluride TE materials prepared by cold pressed process is presented.

1.6Research methodology/Plan

Following steps are executed to achieve the objectives of current work

1. Synthesis of graphene oxide(GO) and reduced graphene oxide(RGO). Also the synthesis of 1D $Bi_2Te_3$and materials with different morphologies.
2. Synthesis and study of conventional ball milling process of alloying different morphological $Bi_2Te_3$and GO/rGO i.e.., 1D materials and 2D materials respectively to form a Nano-compositeand their properties are presented in later chapters.
3. Development of a novel in-situ graphene doped process to obtain graphene doped bismuth telluride 1D nanomaterials.
4. Structural, compositional, morphological of all the synthesized 1D bismuth telluride nanomaterials and their corresponding nanomaterials are investigated.
5. Cold-pressed approach has been opted to obtain pellets for analysis of electrical and thermal conductivity of all the synthesized samples.
6. Thermal conductivity, Seebeck coefficient and electrical conductivity of all the synthesized graphene-bismuth telluride nanomaterials by two different approaches are presented.

Chapter -2

Synthesis and Characterization of GO/rGO and neat Bismuth Telluride Nanomaterials (Nanotubes and Nanorods)

Chapter -2

Synthesis and Characterization of GO/rGO and neat Bismuth Telluride Nanomaterials (Nanotubes and Nanorods)

2.1 Introduction

This chapter presents the synthesis and characterization of graphene oxide (GO), reduced graphene oxide (rGO) and neat bismuth telluride. The effect of the amount of reducing agent on the structure, morphology and composition is presented. The structural, molecular and morphological properties of all the synthesized neat samples were analyzed by XRD, EDS, TEM, FTIR, and RAMAN spectroscopy are presented in this chapter.

2.2 Synthesis and characterization of graphene oxide and reduced Graphene oxide

2.2.1 Synthesis of Graphene Oxide (GO):

Graphene oxide (GO) was synthesized by using pristine graphite flake powder (~45μm) by the modified Hummers method[113]. In a typical process, 5 gm graphite powder was taken in a 2000 mL beaker and 115 mL ofconcentrated H_2SO_4 (115 mL)and 2.5 gm of $NaNO_3$ (2.5gm) were added to it. The above mixture solution was stirred for few minutes by keeping the glass beakers under an ice bath. Once the temperature of the above mixture solution reached 5°C 15 gm of $KMnO_4$ (15gm) was added slowly. Later the ice bath was removed andthe mixture solution was stirred for one hour at room temperature on ahot plate. The solution temperature gradually increased from room temperatureto35°C in the next 2hr of continuous stirring. Then 230 mL of deionized water(DI) was added and stirred for another 15 min and again diluted with 700 mL of DI water.to it. Then, 50 mL of 30% $H_2O_2$was added to the mixture solution to reduce

the residual $KMnO_4$. The above mixture solution waswashedseveral times with DI water followed by 80 mL of 35% HCluntil the pH value reached to 7. The as-obtained graphene oxide (GO) was finally collected by centrifuging, filtering and drying.The resulting graphene oxide (GO) was dried at 100°C for 12 hr in a vacuumoven to obtain the final product.

2.2.2 Thermally reduced Graphene Oxide (rGO):

The reduced graphene oxide (rGO) was synthesized by using two different synthesis processes such as thermal reduction (at 300°C) and chemical reduction (using hydrazine hydrate as a reducing agent). In the first process, the dried GO was taken in a furnace and kept at 300°C to obtain the reduced graphene oxide (rGO).

2.2.3 Chemically reduced Graphene Oxide (rGO):

Hydrazine hydrate was used as a reducing agent to reduce the graphene oxide into reduced graphene oxide[114]. It was usually called an oxygen scavenger because it can convert many oxidized metals into its pure form and it is a very effective reagent that removes the functional groups from the compounds. Graphene oxide consists of several functional groups,alcohol groups and carboxyl groups which can be removed by using hydrazine hydrate as a reducing agent. This removal of functional groups from the graphene oxide results in the separation of layers and thereby few-layered reduced graphene oxides can be obtained.

For this process,250 mg of Graphene oxide was taken in a 500 mL beaker and 250 mL of DI water is added to it. It was sonicated for 60 minuntil a clearer solutionwas formed. Then 10 mL of hydrazine hydratewas added to the mixture solution and kept in stirring at 95°C in a silicone oil bath. The sample was filtered and washed with DI water until the pH of the sample reached 7. Finally, the obtained product was dried at 60°Cfor 12hr by using a vacuum oven and finally, the dried rGO was collected.

2.2.4. Characterization of Graphene Oxide and Reduced Graphene Oxide

Figure 2.1 shows the XRD analysis of synthesized graphene oxide(GO). It is observed from Fig 2.1 that the graphite basal plane (002) shifts to thehigher interplanar distance (2θ=13.5

and d=0.655 nm) due to the oxygen functional groups attached to graphite layers indicates the oxidation of graphite to graphene oxide (GO).

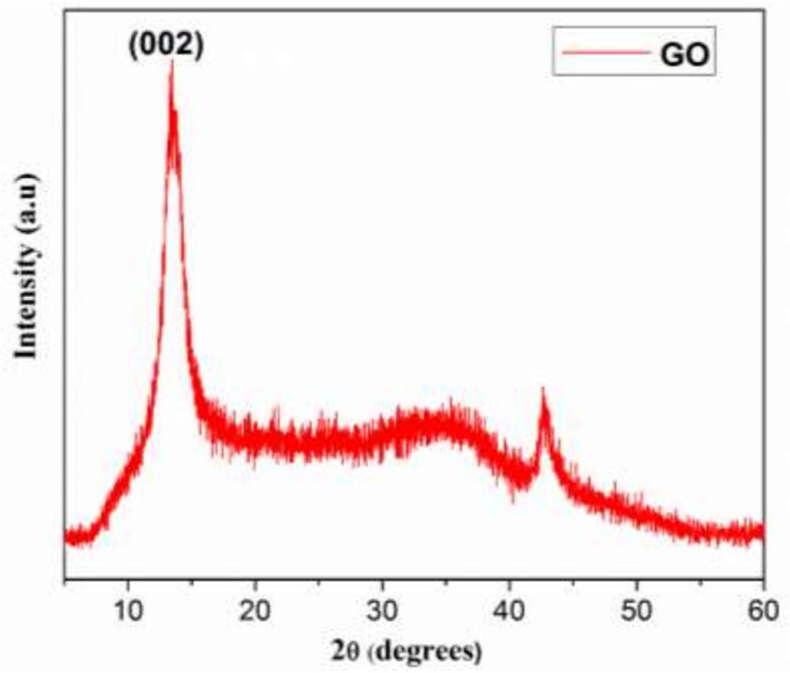

Fig. 2.1 *X-Ray Diffraction spectra of as-synthesized graphene oxide.*

RAMAN spectrum of the as-synthesized graphene oxide is presented in Fig. 2.2(a), which shows the broadening of the G and D peaks. This result indicates that the oxidation has happened and also shows the suppressal of the 2D band. A broad hump also appears in this region as shown in Fig. 2.2(a).Comparatively, with graphite, this graphene oxide shows a higher value of I_D/I_G ratio, which indicates the reduction in graphite domain size and formation of the disorder.It is also seen from Fig. 2.2(a), G band position redshifts while D band appears at 1342cm^{-1} (I_D/I_G = 0.97). The HRTEM analysis of the as-synthesized graphene oxide is shown in Fig. 2.2(b) which confirms a few layers of graphene oxide.

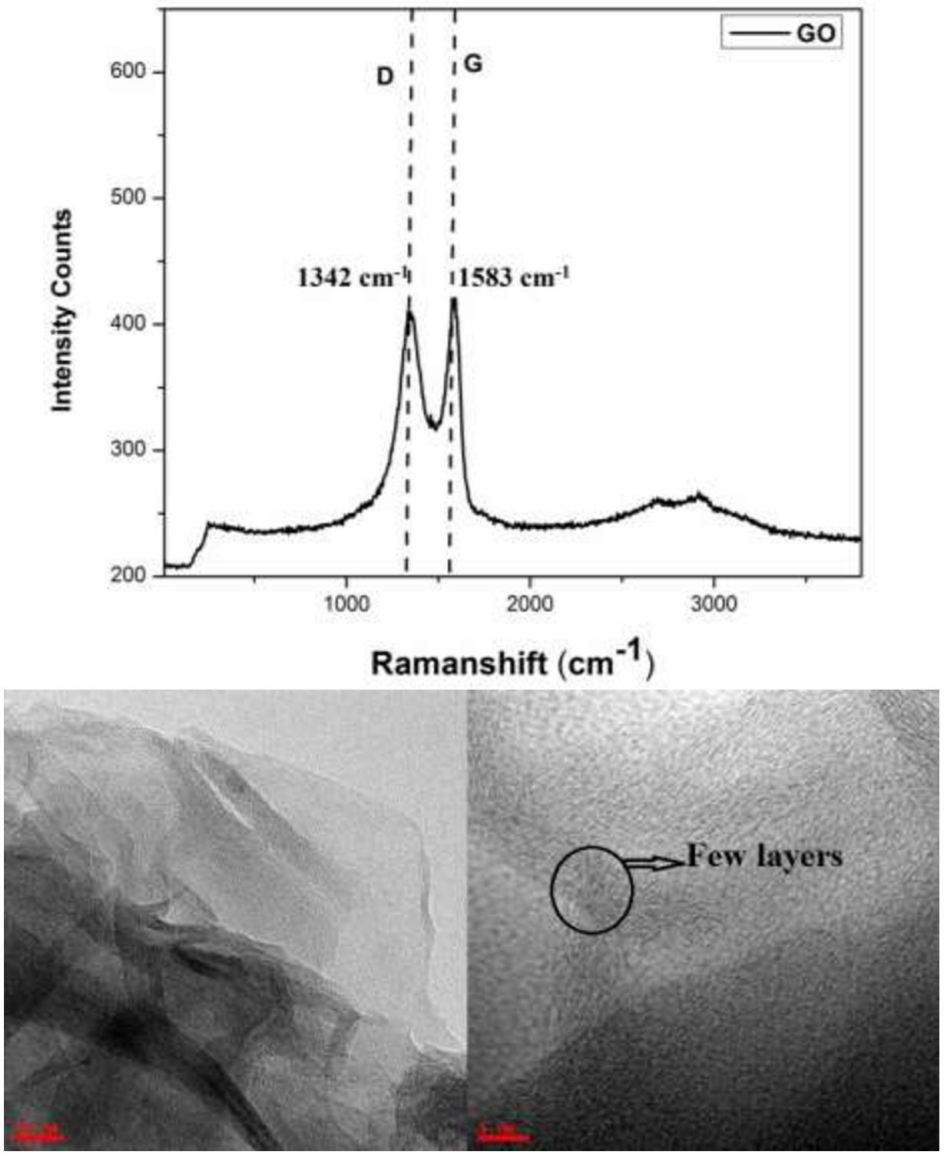

Fig. 2.2 *(a) RAMANspectrum and (b) HRTEM images of as-synthesized graphene oxide (GO).*

The higher resolutions of TEM micrographs of graphene oxide are shown in Fig. 2.2(b) which represents the interplanar distances existing in the Graphene oxide layers.

XRD pattern of thermally reduced graphene oxide (rGO) is shown in Fig. 2.3. It is found in Fig. 2.3 that GO (002) peak shifts to $2\theta = 24.4$, with interplanar distance about 0.364nm which indicates the removal of the oxygen-related functional groups.

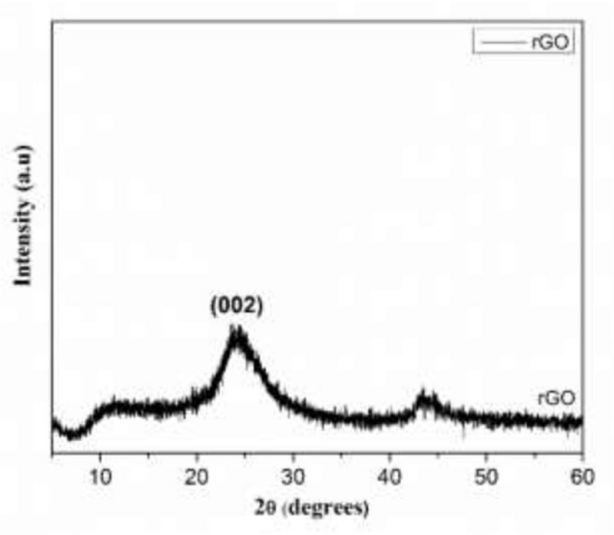

Fig. 2.3*X-Ray Diffraction pattern of as-synthesized thermally reduced graphene oxide (rGO).*

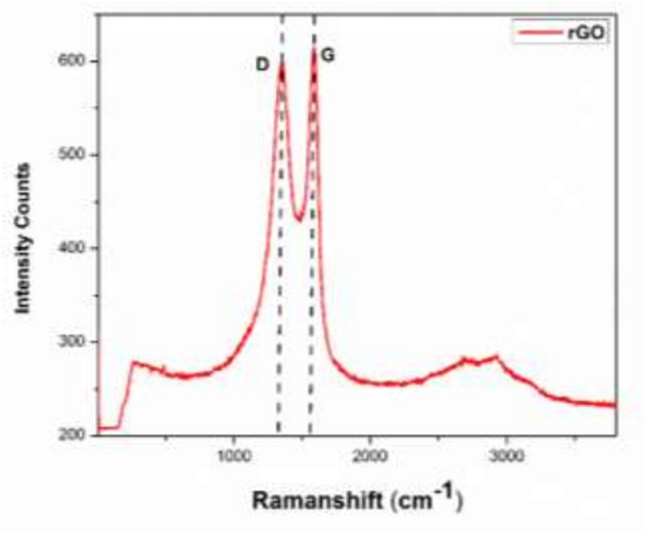

Fig. 2.4 *RAMAN spectrum of as-synthesized thermally reduced graphene oxide (th-rGO).*

RAMAN spectrum of thermally reduced graphene oxide (rGO) is presented in Fig.2.4. Both the D and G bands appear at 1335 cm^{-1} and 1576 cm^{-1} with corresponding I_D/I_G ratio is 0.84

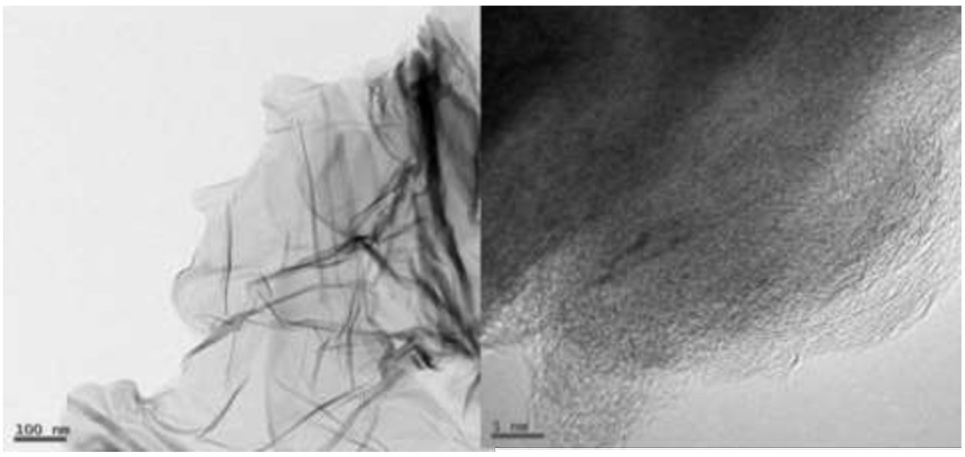

Fig. 2.5 *HRTEM images of as-synthesized thermally reduced graphene oxide (th-rGO).*

Figure 2.5 shows high-resolution TEM of the thermally reduced (rGO), indicating a few layers of rGO are obtained.

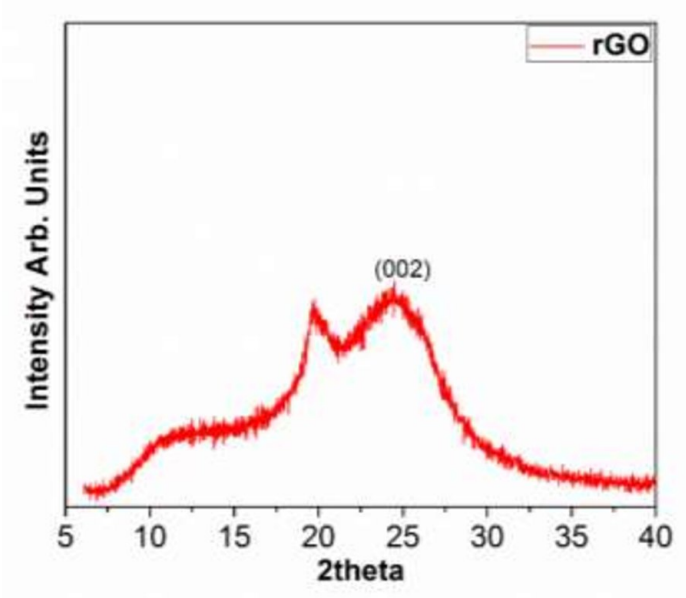

Fig. 2.6 *X-Ray Diffraction spectra of as-synthesized chemically reduced graphene oxide (c-rGO).*

Graphene oxide(GO), which was synthesized by Hummers method was treated with hydrazine hydrate (reducing agent),to obtain the chemically reduced graphene oxide. XRD

pattern of chemically synthesized reduced graphene oxide (c-rGO) is shown in Fig. 2.6. It is seen from Fig. 2.6 that (002) a peak appears at 2θ= 24.4 with d= 0.364, indicating the removal of the oxygen-related functional groups. However, as compared to the thermally reduced-rGO, it is partially oxidized.RAMAN spectrum of the chemically reduced graphene oxide is presented in Fig. 2.7 It is observed that the D-band is slightly broadened and is shifted to around 1342 cm^{-1} and the G band to 1603 cm^{-1}[115]. This is due to the reduction in thickness and removal of functional groups from the graphene oxide.

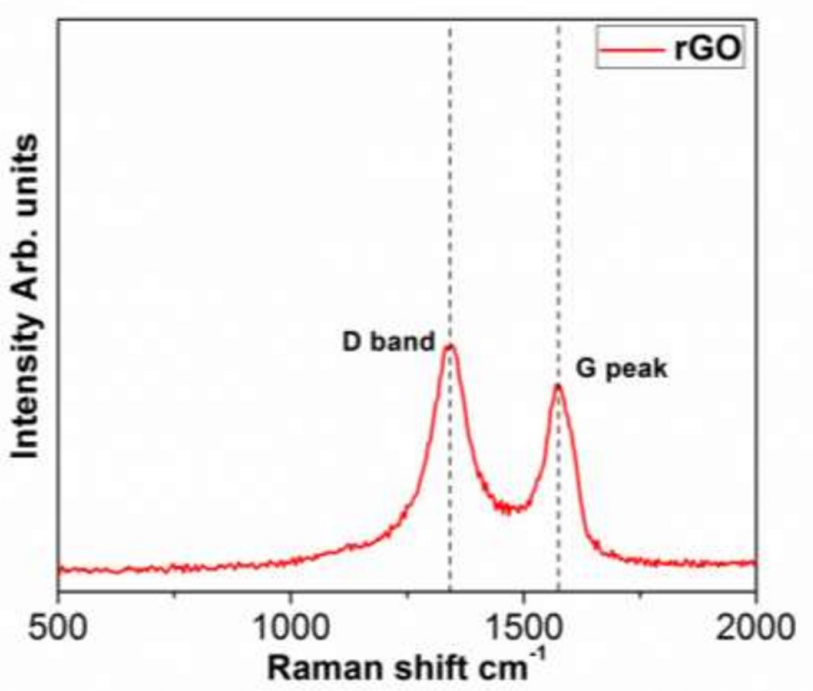

Fig. 2.7 *RAMANspectrumof as-synthesized chemically reduced graphene oxide (c-rGO).*

The high-resolution TEM image of the rGO chemically reduced is shown in Fig. 2.8, indicating few thin and transparent layers of the reduced graphene.

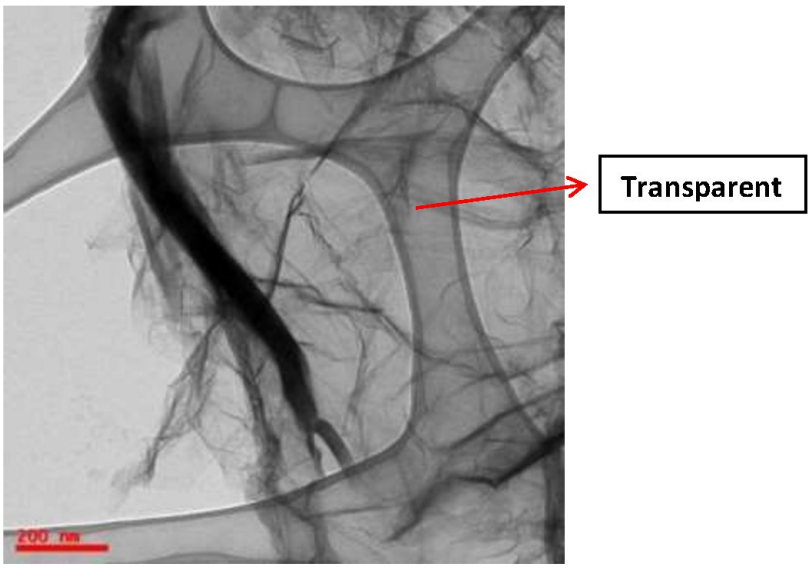

Fig. 2.8 *HRTEM image of as-synthesized chemically reduced graphene oxide (c-rGO).*

2.3 Synthesis and characterization of neat Bismuth telluride thermoelectric nanomaterials

2.3.1. Synthesis of Bismuth telluride nanostructures by rational wet chemical method

Bismuth telluride nanomaterials were synthesized by using a wet chemical method. The flow process of synthesis is graphically illustrated in Fig 2.10. In a typical process 20mL of ethylene glycol (EG), 0.2gm polyvinyl pyrrolidone (PVP MW-40000) 0.6gm of NaOH and 3mmol of TeO_2 powder (99.999%) were added to a three-neck flaskand stirred at 160 ℃ in presence of nitrogen and at this stage 0.8 mL hydrazine hydrate solution was added which acts as reducing agent. After one hour of reaction, bismuth precursor (2mmol of Bismuth (111) nitrate ($Bi(NO_3)_3.5H_2O$) in 5mL ethylene glycol solution) was injected into the three-neck flask.

The nitrogen purging was carried out at regular intervals throughout the reaction. The temperature inside the flask was monitored by a thermometer. A condenser with inlet and out of the water was kept on the top of the three-neck flask with running cold water as shown in the schematic (Fig. 2.9). After an hour of reaction, the mixture solution was collected and washed

several times with methanol followed by DI water. It was filtered to obtain the powder form of the sample. Finally, the obtained product was dried at 50 °C fir 12hr by using a vacuum oven.

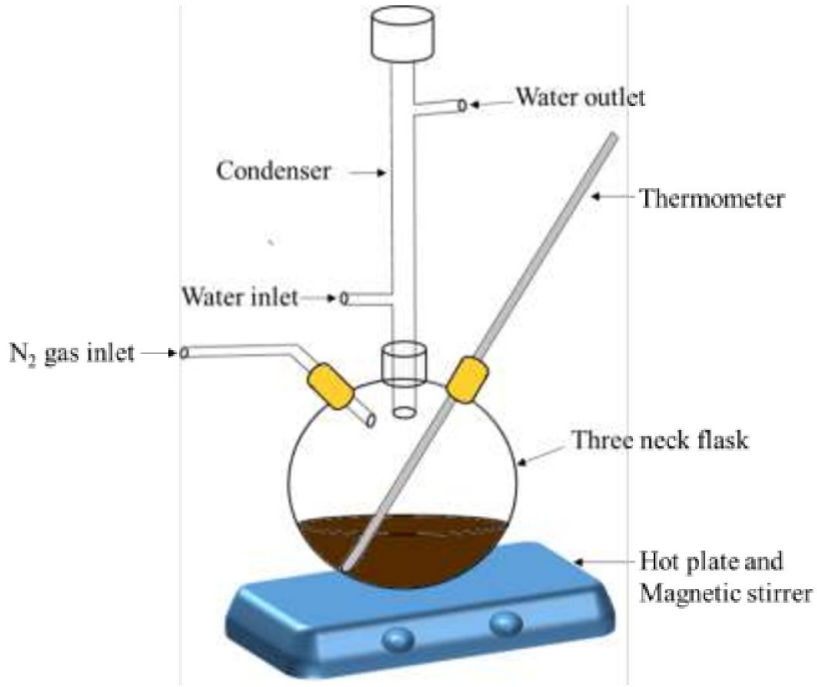

Fig. 2.9 *Experimental setup of Bi_2Te_3 synthesis.*

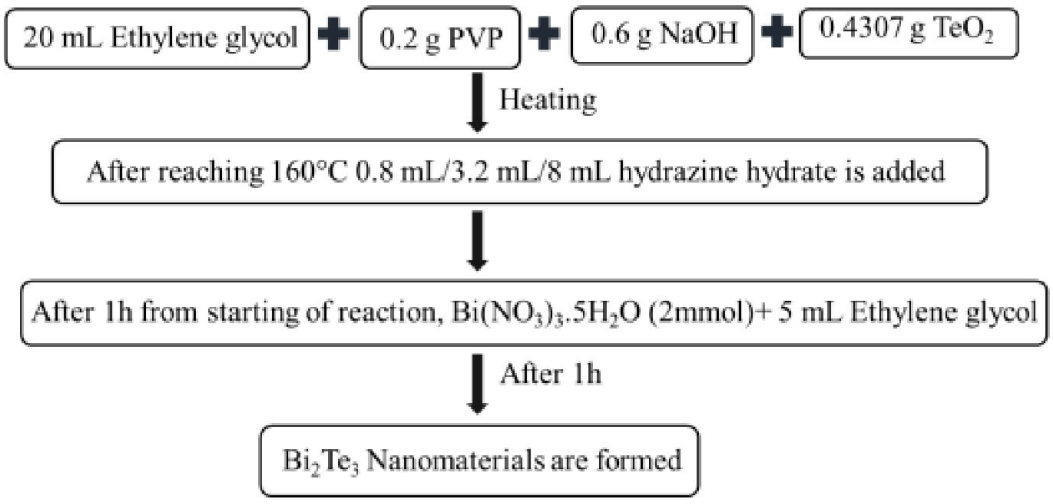

Fig. 2.10 *Flow chart for the synthesis of bismuth telluride nanomaterials by rational synthesis method.*

The nomenclature of all the neat materials synthesized in this chapter is shown inTable 2.1.

Table 2.1 All synthesized GO, rGO and bismuth telluride samples

Sl. No.	Sample ID	Synthesis Method
1	GO	Hummers Method
2	rGO	Thermally/ Chemically
3	0.8-NW(NEAT) Bi_2Te_3	0.8mL H.H. (Hydrazine Hydrate)
4	3.2-NT(NEAT) Bi_2Te_3	3.2mL H.H.
5	8-NT(NEAT) Bi_2Te_3	8mL H.H.

2.3.2. Characterization of different Bismuth telluride nanomaterials

The pristine bismuth telluride nanomaterials were characterized by X-ray diffractometer Bruker D8 advance. Fig. 2.11 represents the corresponding XRD patterns of the as-obtained samples synthesized at 0.8mL, 3.2mL and 8mL amount of reducing agent. The corresponding diffraction planes are (015), (1010), (110), (0015), (205), (0210), (1115), (125) and (1022). As shown in Fig. 2.11 these planes match with the bismuth telluride rhombohedral structure (JCPDS:080021). It is found out that all the crystal planes are in good agreement with the standard diffraction planes of bismuth telluride; however, peak broadening is identified in the bismuth telluride nanotubes synthesized with 3.2mL reducing agent.

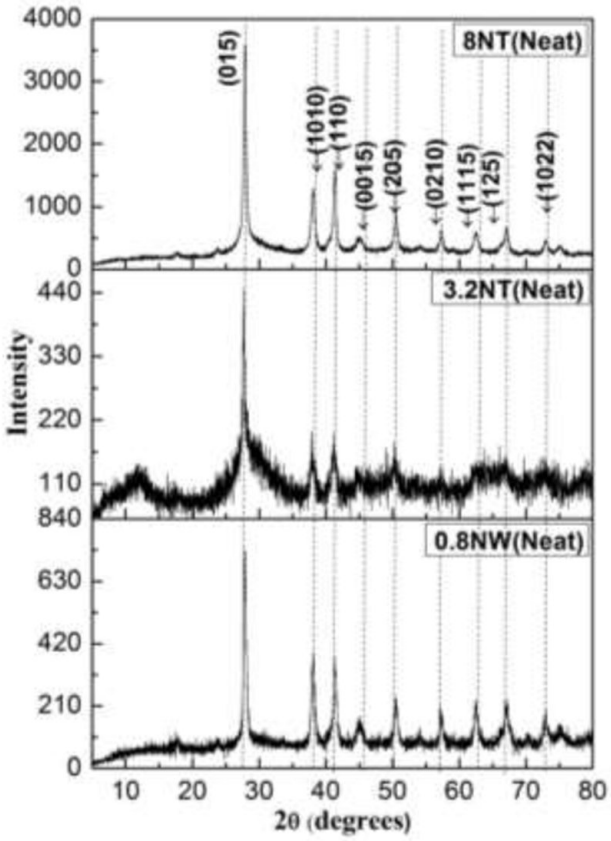

Fig. 2.11*X-Ray Diffraction plots of as-synthesized Bi_2Te_3 nanomaterials with 0.8mL, 3.2mL and 8mL reducing agents.*

Table 2.2Lattice parameters of the bismuth telluride nanomaterials with different morphologies

Sample ID	Lattice parameter a (Å)	Lattice parameter c (Å)
0.8-NW(NEAT) Bi_2Te_3	4.33	29.21
3.2-NT(NEAT) Bi_2Te_3	4.38	30.24
8-NT(NEAT) Bi_2Te_3	4.36	30.02

Lattice parameters of all the three samples have been calculated and tabulated in Table 2.2. The lattice parameters have been calculated for major planes of the bismuth telluride using the standard method[116].

Figures 2.12, 2.13 and 2.14 show the FESEM images of the samples synthesized by using 0.8mL, 3.2mL and 8mL amount of reducing agent. It is seen from Fig. 2.12 that the sample synthesized by using 0.8 mL reducing agent consists of nanorods with an average length of 2.75 μm and diameter nearly about 85nm.

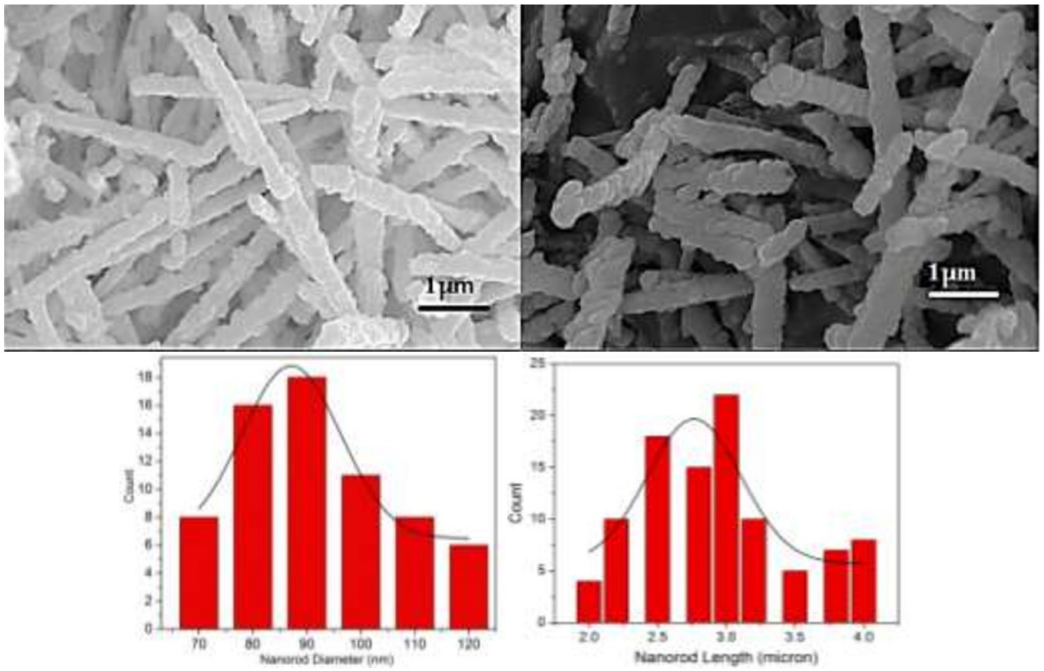

Fig. 2.12 *FESEM images of 0.8-NW-Neat Bi_2Te_3 nanostructures(obtained by using 0.8mL reducing agent).*

It is also seen from Fig. 2.13 that hollow nanotubes of Bi_2Te_3 with an average length of 2.4μm and diameters of 75nm are obtained when 3.2mL reducing agent was used.

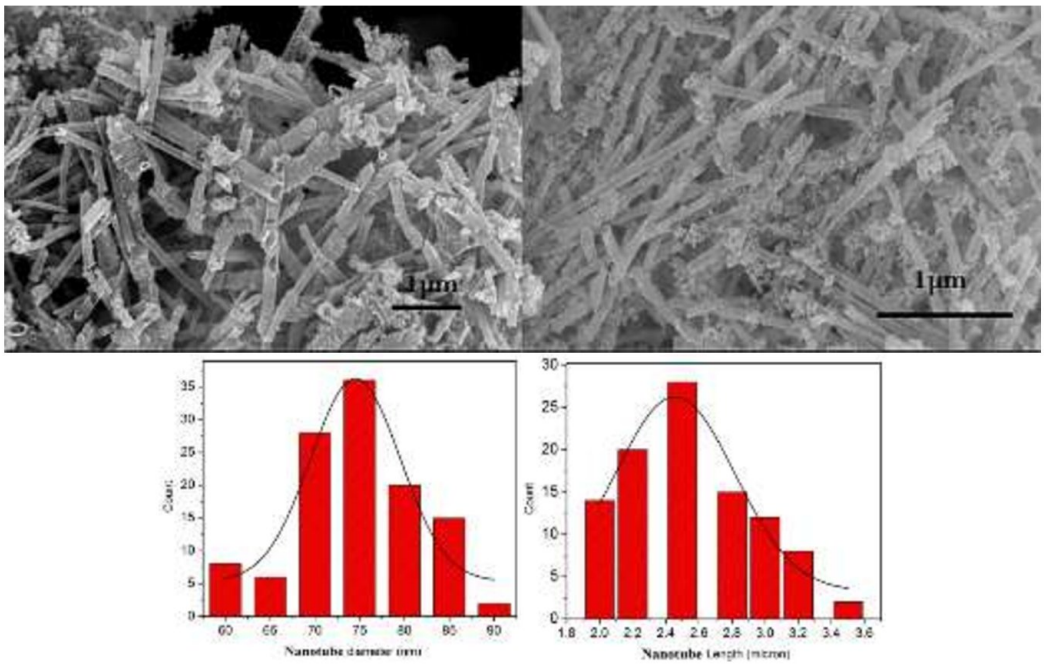

Fig. 2.13 *FESEM images of 3.2-NT-Neat Bi_2Te_3 nanostructures(obtained by using 3.2mL reducing agent).*

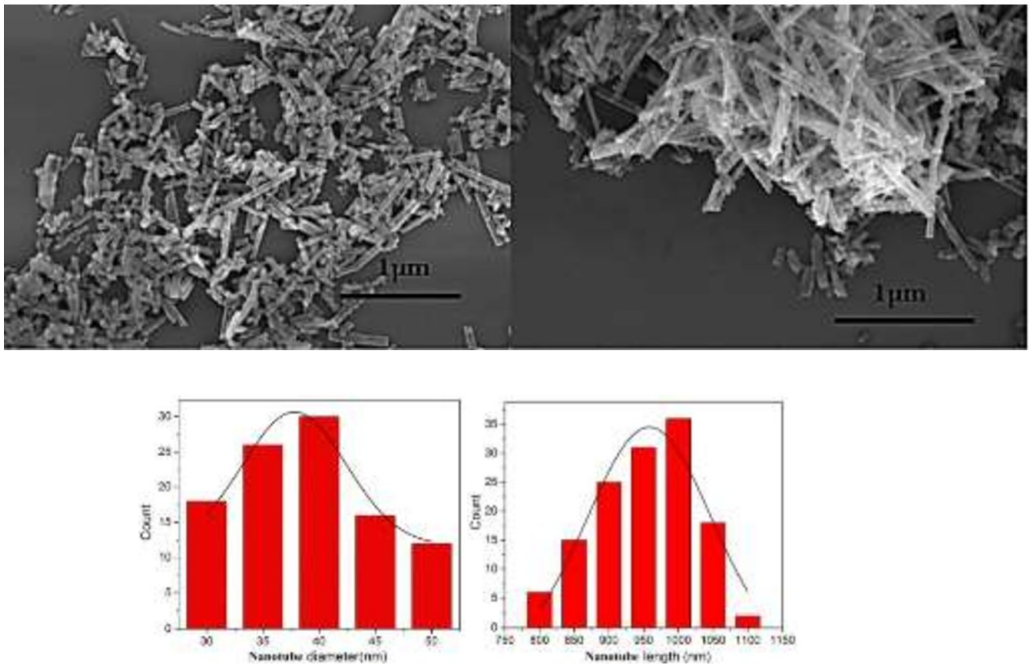

Fig. 2.14 *FESEM images of 8-NT-Neat Bi_2Te_3 nanorods(obtained by using 8mL of reducing agent).*

Hollow nanotubes of Bi_2Te_3 with the smaller diameter of around 20-40 nm are observed as shown in Fig. 2.14 when 8 mL reducing agent was used for synthesis.

Therefore, chain-like nanorods, larger diameter nanotubes and smaller diameter nanotubes are obtained by using 0.8mL, 3.2mL and 8mL amounts of reducing agents respectively.

EDS analysis of all the three obtained bismuth telluridenanomaterials is shown in Table 2.3. A significant change in the percentage composition of Bi to Te ratio is observed

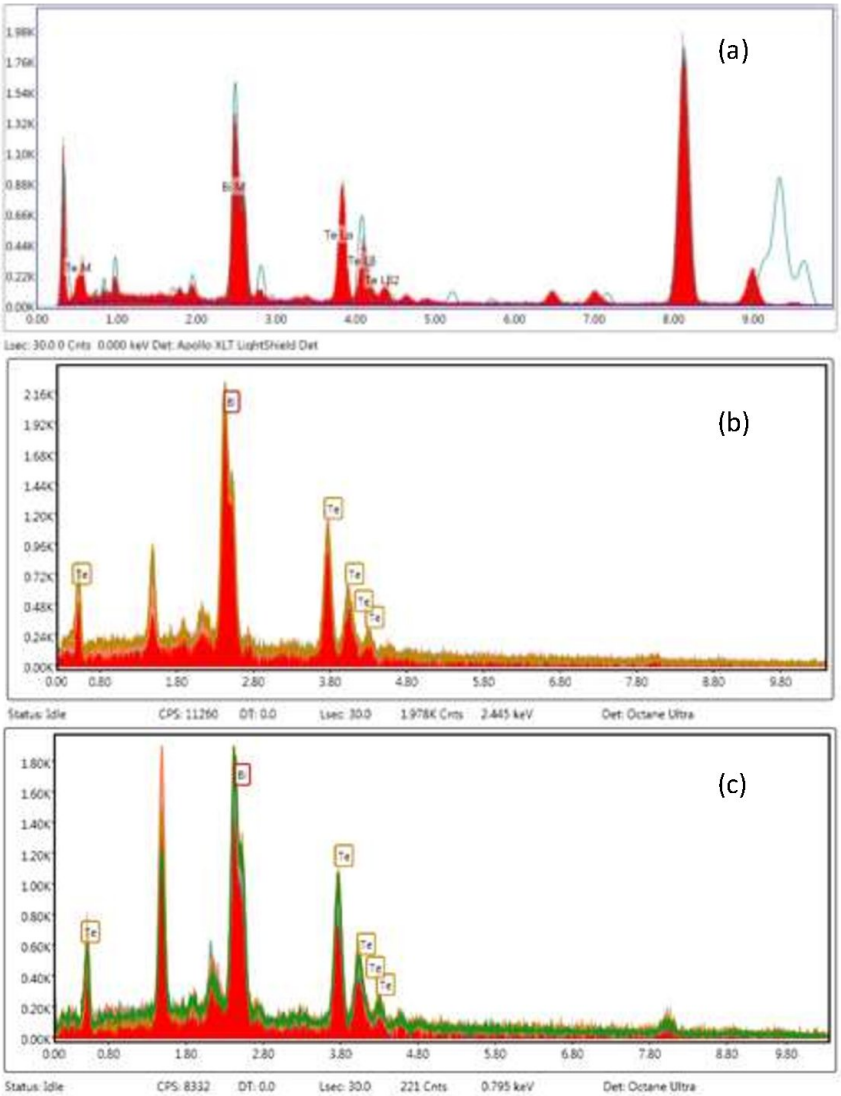

Fig. 2.15 *EDS spectra of (a)0.8NT, (b)3.2NT and (c)8NT- Neat samples*

. It is found that 0.8-NW Bi_2Te_3 nanorods synthesized by using 0.8 mL RA possess Te rich compound. Whereas, 3.2-NT Bi_2Te_3 hollow nanotubes are Bi rich compound. On the other hand, 8-NT Bi_2Te_3 hollow nanotubes with smaller diameter show near stoichiometric composition.

Table. 2.3EDS analysis data of neatsynthesized bismuth telluride nanomaterials.

Sample ID	Bi%	Te%
0.8-NW(NEAT) Bi_2Te_3	34.29	65.71
3.2-NT(NEAT) Bi_2Te_3	47.2	52.8
8-NT(NEAT) Bi_2Te_3	42.65	57.3

FTIR analysis wasperformed on all the as-synthesized different morphologybismuth telluride nanomaterial and the corresponding FTIR spectra are shown in Fig 2.16. Different bands appear at 640 cm^{-1}, 1029cm^{-1}, 1195, 1387cm^{-1}, 1468 cm^{-1}, 1653cm^{-1}, 1752cm^{-1}, 2855cm^{-1}, 2933cm^{-1} and 3550cm^{-1} corresponding to C-O,C-C, CH_3, -CH_3, CH_3(Asymmetric deformation) C=C, C-O, C=O -CH_2- (Symmetric stretch)-CH_2-(Asymmetric stretch) and also the O-H bonds (Fig. 2.16). FTIR results indicate that some hydroxyl (-OH) and carboxyl (-COOH) groups are present in all the synthesized samples. Possible reason for the presence of these groups is that the synthesis process involves a lot of chemicals and also a cleaning process with methanol and distilled water. Therefore these functional groups are present in the synthesized materials.

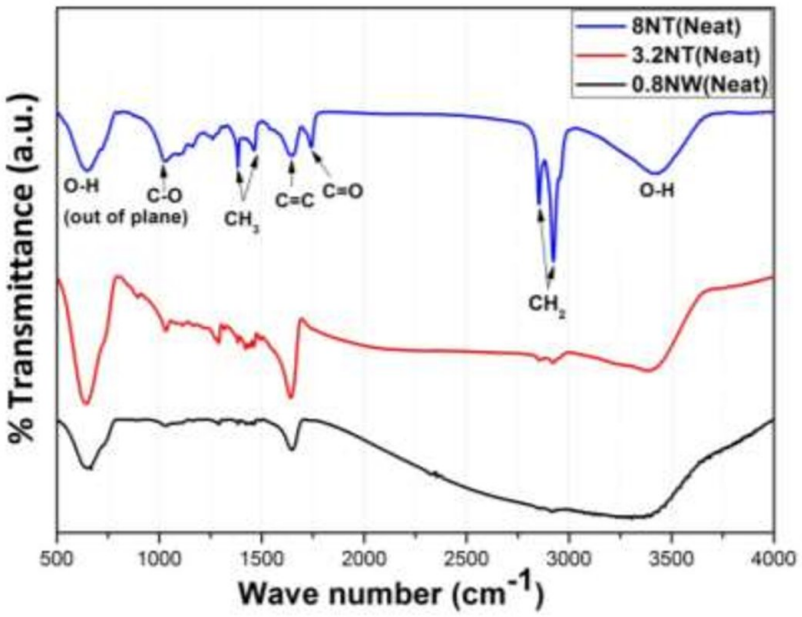

Fig. 2.16 *FTIR spectra of as-synthesized different morphology Bi_2Te_3 nanomaterials.*

Figure2.17 shows the RAMAN spectra of all the synthesized bismuth telluridenanorods and nanotubes samples. As shown in Fig.2.17 different bands appear at 60 cm^{-1}, 100 cm^{-1}, 120 cm^{-1} and 140 cm^{-1} and those correspond to A^1_{1g}, E^2_g and A^2_g. When the laser excites the $Bi_2Te_3$the atoms vibrating in basal planes can be attributed in E^2_gmodes,these atoms vibrating in trigonal direction cab be attributed to the A^1_{1g} modes[112]. It is also observed that the intensity of E^2_gdecreases for the sample 8-NT (NEAT) sample, possibly due to reduction in diameter of the nanotubes. This is significant as reported previously[48].

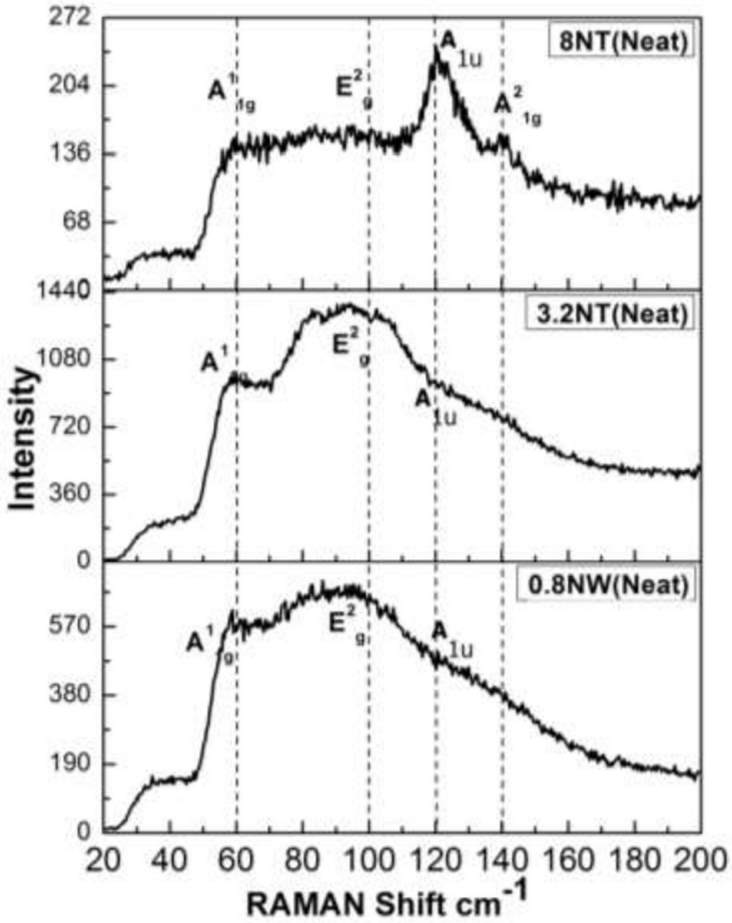

Fig. 2.17 *RAMAN spectra of as-synthesized 0.8mL, 3.2mL and 8mL (RA) Bi_2Te_3 nanomaterials.*

HRTEM studies were carried on the samples and Fig. 2.18, 2.19 and 2.20 represent the TEM and HRTEM images with SAED patterns for the samples synthesized with 0.8mL, 3.2mL and 8mL reducing agents, respectively. It is found the morphology of the sample synthesized at 0.8mL RA is nanorod. The corresponding HRTEM image as shown in Fig 2.18 (b) shows the lattice spacing is near about 0.31nm. Also, it is clearly seen from Fig. 2.18(b) thatdislocations are present in this sample.

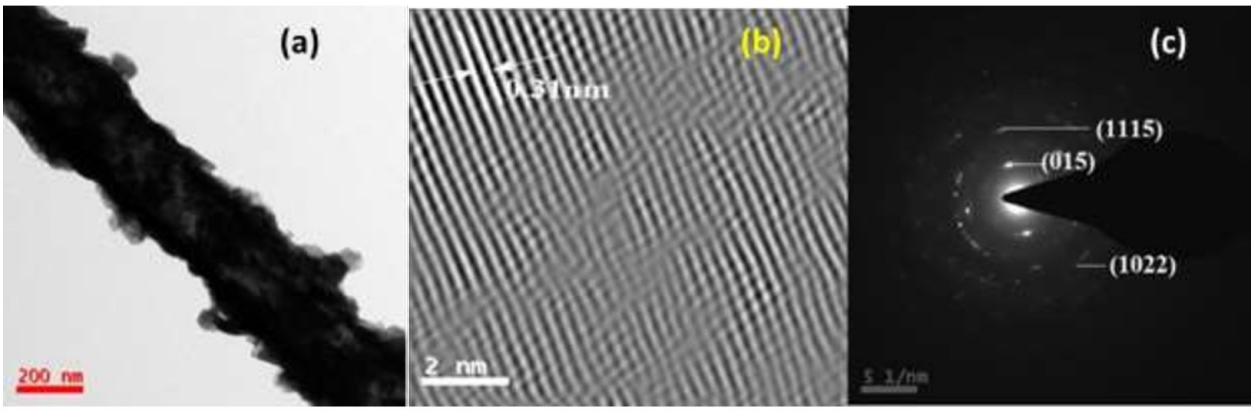

Fig. 2.18 *(a) TEM, (b) HRTEM and (c)SAED pattern of as-synthesized 0.8-NW (Neat) Bi_2Te_3 nanomaterial.*

From the TEM image ofbismuth telluride synthesized by 3.2mL RA as shown in Fig. 2.19(a), the morphology of the sample is found to be hollow in nature. Small particle agglomerates are also observed in the TEM image. Corresponding HRTEM image from Fig. 2.19 (b) shows the lattice spacing of 0.22nm which corresponds to the d spacing of (110) plane of bismuth telluride.

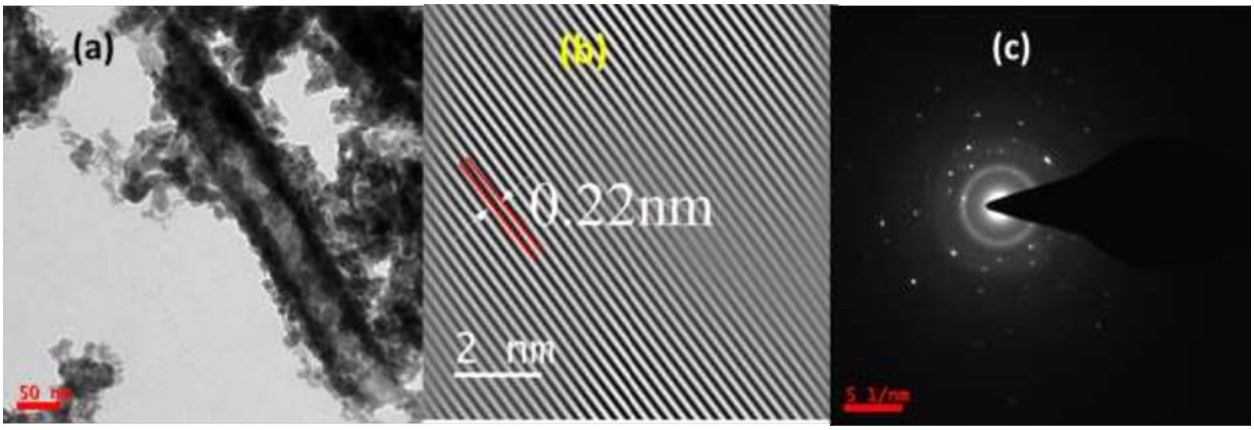

Fig. 2.19 *(a) TEM, (b) HRTEM and (c)SAED pattern of as-synthesized 3.2-NT (Neat) Bi_2Te_3 nanomaterial.*

Fig 2.20 (a) shows the TEM image of bismuth telluride synthesized by 8mL RA, hollow nanotubes morphology is observed. Fig. 2.20 (b) shows the corresponding HRTEM image and it

is found that d spacing is about 0.31nm and 0.22nm corresponding to the planes (015) and (110) respectively.

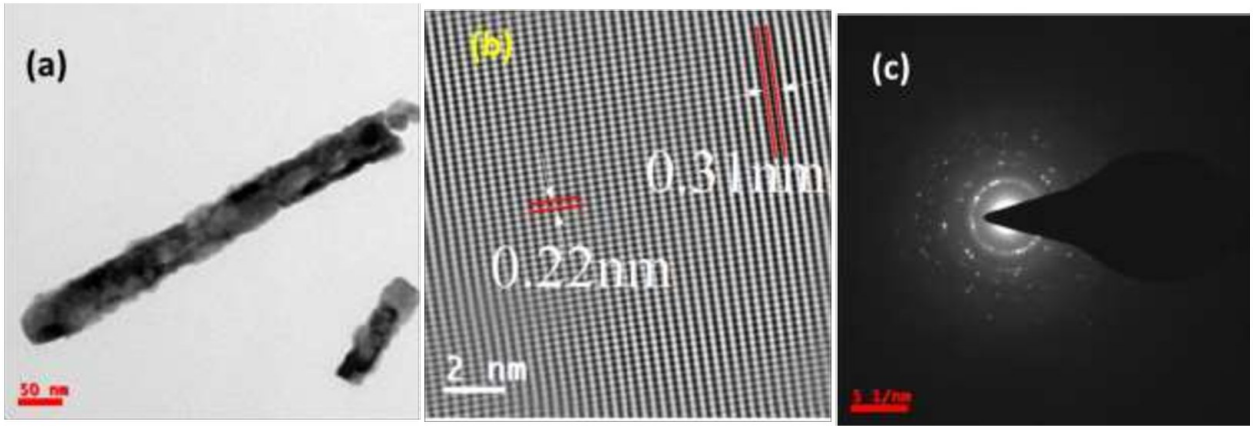

Fig. 2.20 *(a) TEM, (b) HRTEM and (c)SAED pattern of as-synthesized 8-NT (Neat) Bi_2Te_3 nanomaterial.*

Table 2.4 depicts the nomenclature of the different samples synthesised and later these samples have been used to synthesize the graphene-bismuth telluride based nanomaterials by the ball milling process.

Table 2.4. Nomenclature of the different synthesized samples from this chapter.

Nomenclature		
1	0.8-NW(NEAT) Bi_2Te_3	Nanorods
2	3.2-NT(NEAT) Bi_2Te_3	Nanotubes
3	8-NT(NEAT) Bi_2Te_3	Nanotubes (Smaller diameter)
4	Neat GO/ rGO	Chemical reduction
5	Neat GO/rGO	Thermal reduction

2.4 Conclusion

Graphene oxide (GO) and reduced graphene oxide (rGO) were successfully synthesized by using modified Hummers method. Analytical and spectroscopic analysis results revealed that graphite flakes were oxidized to obtain GO with multilayers. Different amounts of reducing agents were used in synthesizing different morphological 1D bismuth telluride nanomaterials such as nanorods, larger diameter nanotubes and smaller diameter nanotubes. These morphologies were evidenced by FESEM and TEM results.

CHAPTER-3

Fabrication and Characterization of GO/rGO-Bi_2Te_3 Thermoelectric Nanocomposites by Mechanical Alloying

CHAPTER-3

Fabrication and Characterization of GO/rGO-Bi_2Te_3 Thermoelectric Nanocomposites by Mechanical Alloying

3.1 Introduction

In the previous chapter, synthesis of neat GO, neat rGO and different neat bismuth telluride nanomaterials with their optimized synthesis parameters have been discussed. This chapter presents the fabrication and characterization of bismuth telluride based nanocomposites by following the ball milling process, using GO and rGO as nanofillers. Different morphologies of bismuth telluride such as nanorods, nanowires, and nanotubes were synthesized by rational chemical approach as discussed in the previous chapter and were used as source materials to study the impacts of morphologies on the structure, morphology and thermophysical properties of the fabricated nanocomposites. Structural, morphological, and compositional characterizations have been carried out by XRD, FESEM, TEM, and EDS for all the synthesized hybrid materials. Thermophysical properties of all ball-milled GO and rGO-bismuth telluride nanocomposites are discussed in **Chapter 5**.

3.2 Synthesis procedure:

The synthesis procedure of neat bismuth telluride with different morphologies such as nanorods, smaller diameter, and larger diameter nanotubes have been discussed in the earlier chapter. These different 1D bismuth telluride nanomaterials were used as a host material to prepare the nanocomposites. Similarly, synthesis procedures of GO and rGO have been discussed in **Chapter 2**, have been prepared by modified Hummers' method and thermal reduction respectively. The obtained GO and rGO were chosen as filler material in the fabrication of nanocomposites.

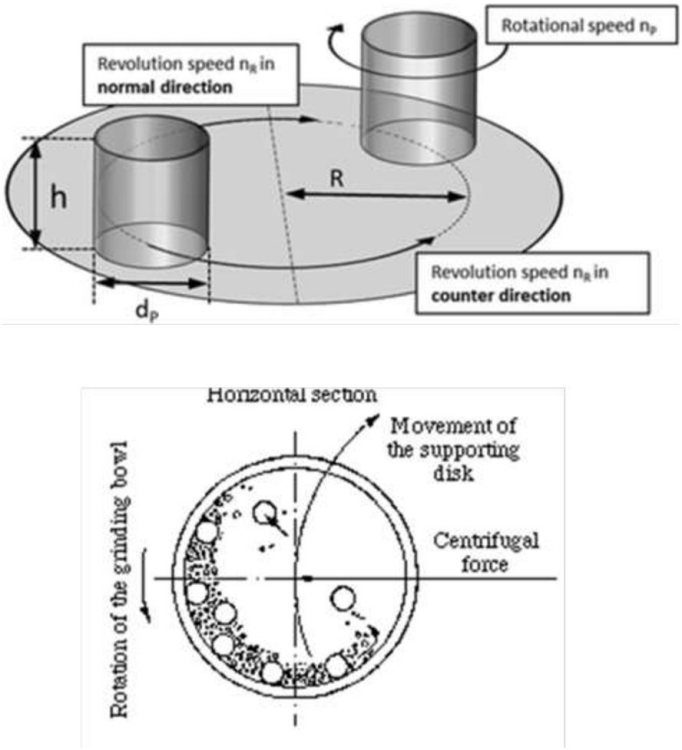

Fig. 3.1 *Schematic of a planetary ball milling to fabricate the nanocomposites.*

GO and rGO-bismuth telluride nanocomposites were synthesized by mechanical alloying with a planetary ball mill (Fritsch Planetary Pulverisette 5/4 Classic line). For this purpose, stainless steel vials, ceramic zirconia balls were chosen. The ball to mill ratio was maintained at 10:1 and 200 rpm milling speed for 90 min. In order to avoid the excess heat evolution during the ball-milling process, a 5 min break was taken after every 15 min of the ball-milling process. It was reported earlier that 3wt% of graphene/ Bi_2Te_3 NW composites have shown higher carrier mobility and carrier concentration[83]. Hence, the amount of the matrix(Bi_2Te_3)was taken as 97% of total weight and the inclusion(GO/rGO) is 3% of total weight. The mechanical alloyed product was collected from the vials and stored in airtight sample containers to carry out further investigations. Table 3.1 shows the nomenclature of different synthesized nanocomposites with three different morphologies of bismuth telluride milled with GO and rGO separately resulting in 6 samples.

Table 3.1 Nomenclature of the samples synthesized bismuth telluride nanostructures and nanocomposites.

S.no	Nomenclature	
	Sample ID	**Sample Contents**
1	0.8NW-GO-BM1	0.8mL RA-Nanorod-Bi_2Te_3 -3%GO
2	0.8NW-rGO-BM2	0.8mL RA-Nanorod-Bi_2Te_3 -3%rGO
3	3.2NT-GO-BM3	3.2mL RA-Nanotube-Bi_2Te_3 -3%GO
4	3.2NT-rGO-BM4	3.2 mL RA-Nanotube-Bi_2Te_3-3%rGO
5	8NT-GO-BM5	8mL RA-Nanotube-Bi_2Te_3 -3%GO
6	8NT-rGO-BM6	8mL RA-Nanotube-Bi_2Te_3-3%rGO

3.3 Structural characterization by X-ray Diffraction

XRD pattern of Bi_2Te_3 and the corresponding GO/rGO-Bi_2Te_3samples is shown in Fig 3.2 (a-c) (*JCPDS card no. 080021*). The peaks appear at 27.6^0, 37.8^0, 41^0, 45.5^0, 50.2^0, 57.49^0, 62.53^0, 67.36^0 and 73.12^0 corresponding to (015), (1010), (110), (0015), (205), (0210), (1115), (125), (1022) planes can be indexed to the rhombohedral structure (*JCPDS card no.080021*).It is also found that the peaks those are corresponding to GO and rGO are not observed in the XRD pattern of the nanocomposites as shown in Fig. 3.2(a-c), possibly due to the overlapping with the (015) peak of the Bi_2Te_3. In order to confirm the coupling of the rGO/GO with Bi_2Te_3, RAMANspectroscopyand FTIR measurement were performed and are discussed in the subsequent sections.

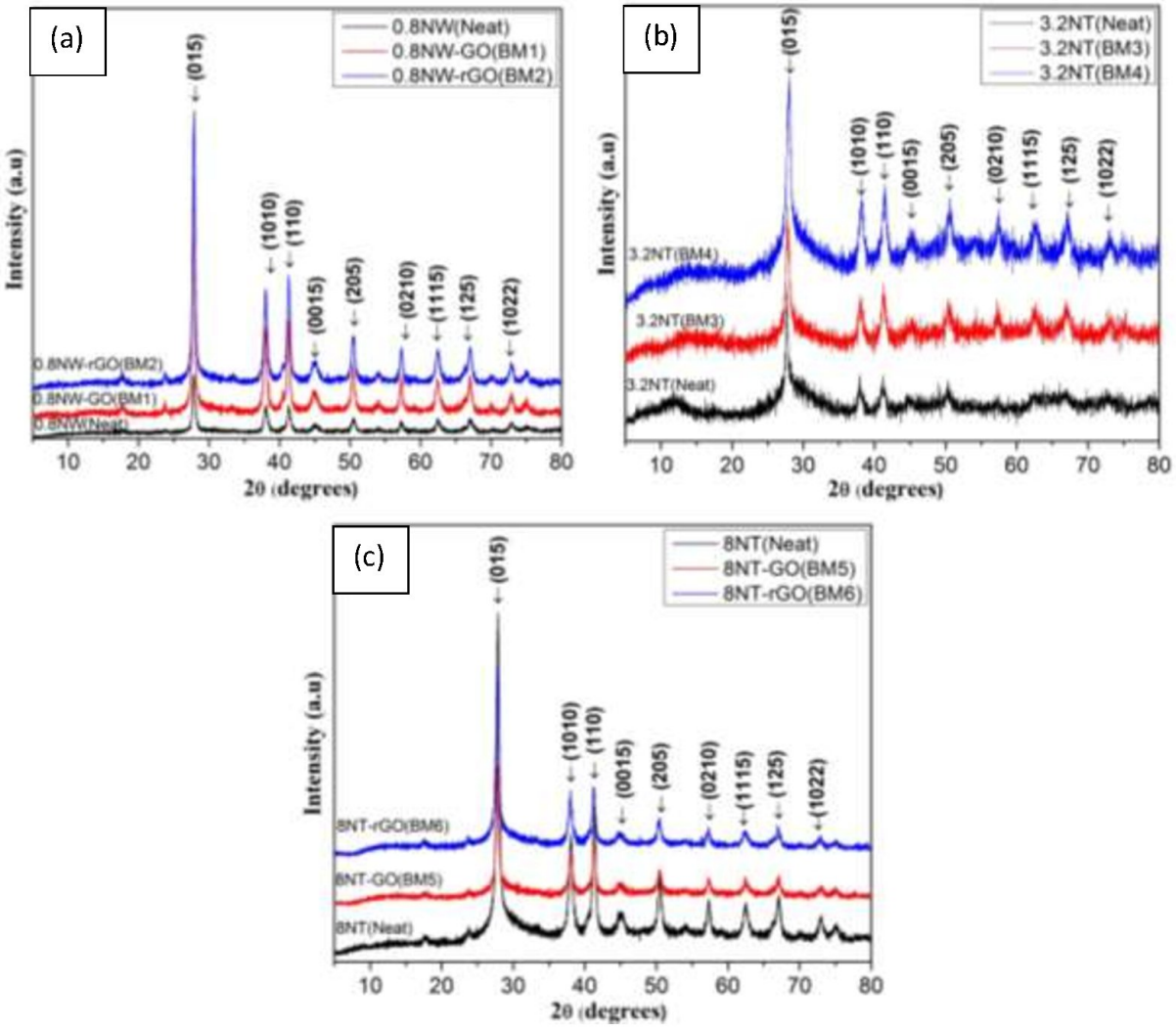

Fig. 3.2*X-ray diffraction patterns of (a) 0.8-NW neat Bi_2Te_3 along with GO- Bi_2Te_3 (BM1) and rGO- Bi_2Te_3(BM2) nanocomposite, (b) 3.2-NT neat sample Bi_2Te_3 along with GO- Bi_2Te_3 (BM3) and rGO- Bi_2Te_3(BM4) nanocomposite and (c) 8-NT neat Bi_2Te_3 along with GO- Bi_2Te_3 (BM5) and rGO- Bi_2Te_3 (BM6) nanocomposite.*

The lattice parameters of all the samples were calculated and by using the standard method [116] shown in Table 3.2.

Table 3.2 Calculated lattice parameters of the obtained samples.

Sample ID	Lattice parameter a (Å)	Lattice parameter c (Å)
0.8-NW-Neat-Bi_2Te_3	4.33	29.21
0.8NW-GO-BM1	4.36	30.15
0.8NW-rGO-BM2	4.36	30.02
3.2-NT-Neat-Bi_2Te_3	4.38	30.24
3.2NT-GO-BM3	4.36	30.15
3.2NT-rGO-BM4	4.36	29.72
8NT-Neat-Bi_2Te_3	4.36	30.02
8NT-GO-BM5	4.36	30.11
8NT-rGO-BM6	4.37	30.21

The lattice parameters (a,c) of the bismuth telluride nanostructures material are about 4.38 Å and 30.4 Å [117]. It is found that lattice parameters do not change so much for all the samples. However, the lattice parameter (c) changes slightly from 29.21 Å and 29.72 Å for the 0.8-NW-neat- Bi_2Te_3 and 3.2NT-rGO-BM4 samples.

3.4 Morphological characterization by FESEM and TEM

Morphological investigations of all the samples were carried out by field emission scanning electron microscope NOVANANO SEM with the electron gun (FEI). For the FESEM and TEM investigations, the samples were prepared by taking a few mg of sample in 50 mL distilled water and sonicated for one hour and were drop-casted on the pre-cleaned silicon substrate and on the copper grid for TEM respectively.

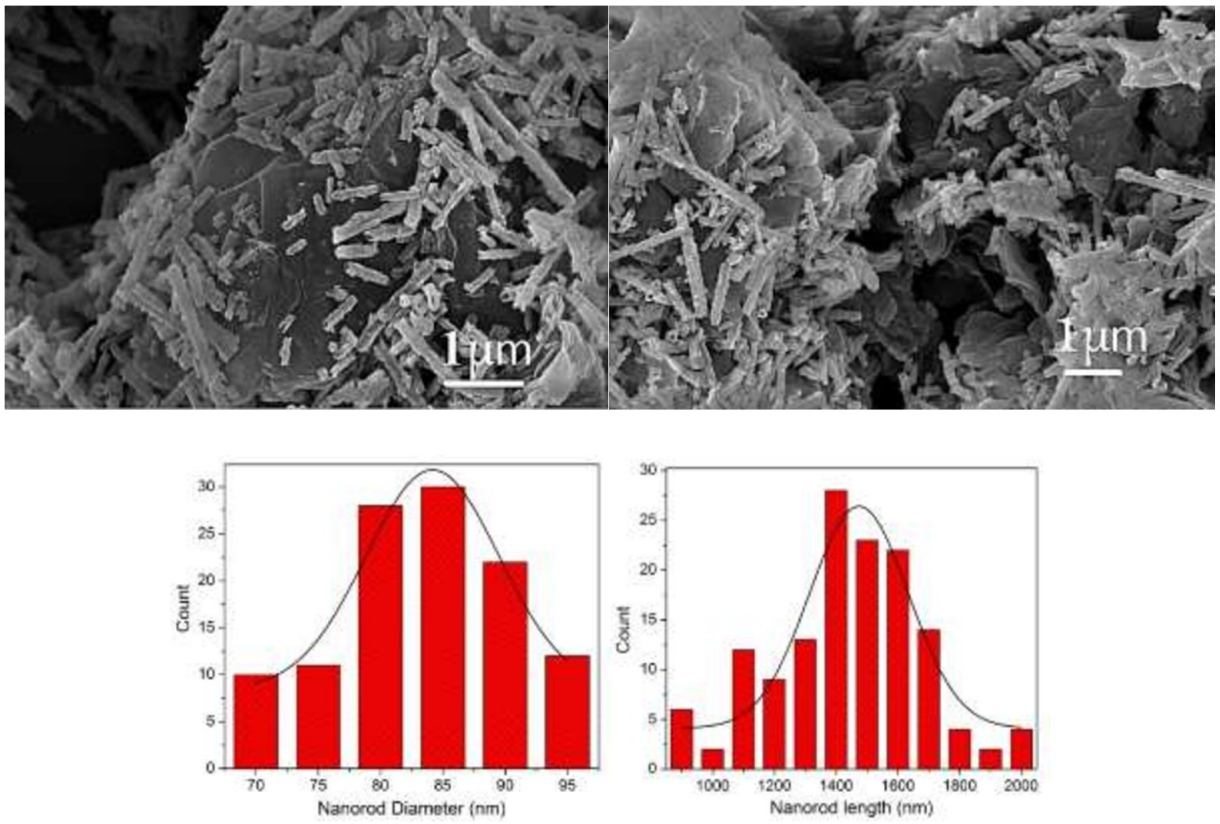

Fig. 3.3 *FESEM images of the 0.8NW-GO-BM1 nanocomposite.*

The mechanically alloyed 0.8NW-GO-BM1 sample was taken in a glass beaker containing DI water and sonicated for one hour. One drop of this solution dried on a silicon substrate for FESEM characterization. Fig. 3.3 shows the FESEM image of this sample. It is seen that bismuth telluride nanorods are cited on the surface of GO sheets, as shown in Fig. 3.3. It is also observed that the high energy ball mill has resulted in the breakage of nanorods in lengthwise.The corresponding length after ball milling is 1.5 microns; however, the as-prepared sample consists of a length ofabout 2.75 microns.

Fig.3.4shows the FESEM image of 0.8NW-rGO-BM2 sample. As shown in Fig.3.4 nanorods of bismuth telluride are broken as compared to the original length before ball-milling. Also, it is found that (Fig.3.4)the smaller size broke nanorods align themselves in between the GO sheets.

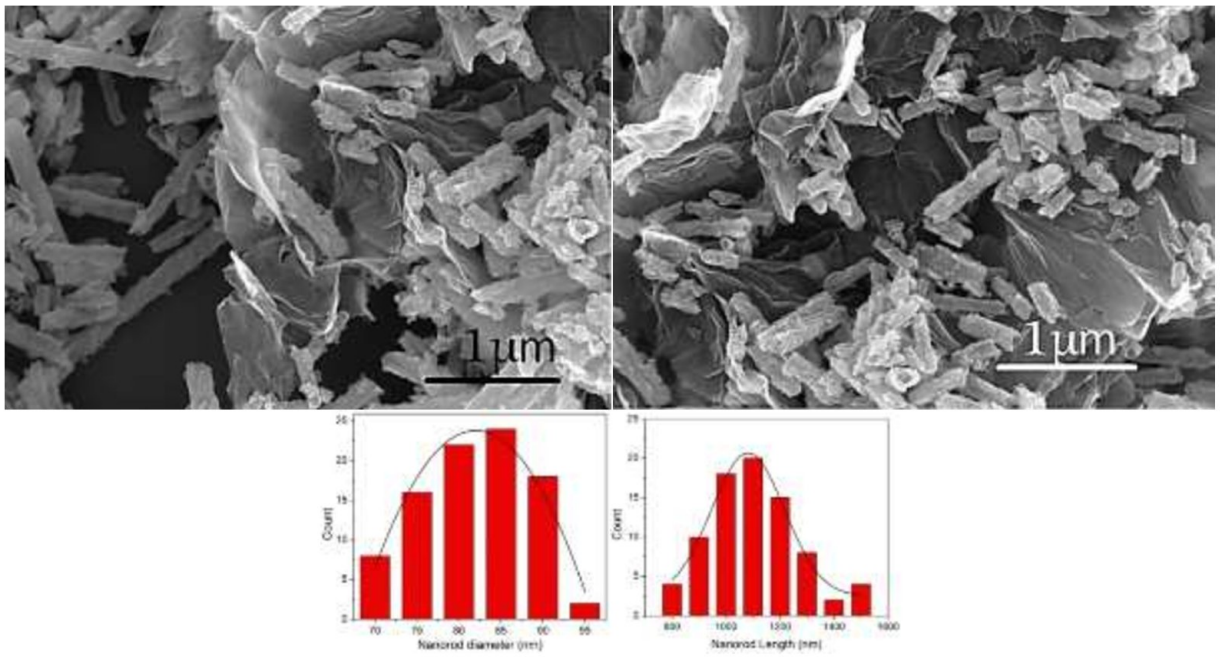

Fig. 3.4 *FESEM images of the 0.8NW-rGO-BM2nanocomposite.*

Fig 3.5 shows the FESEM image of the 3.2-NT-GO-BM3 sample. It is seen from Fig 3.5 that nanotubes are broken and decorated throughout the GO sheets.

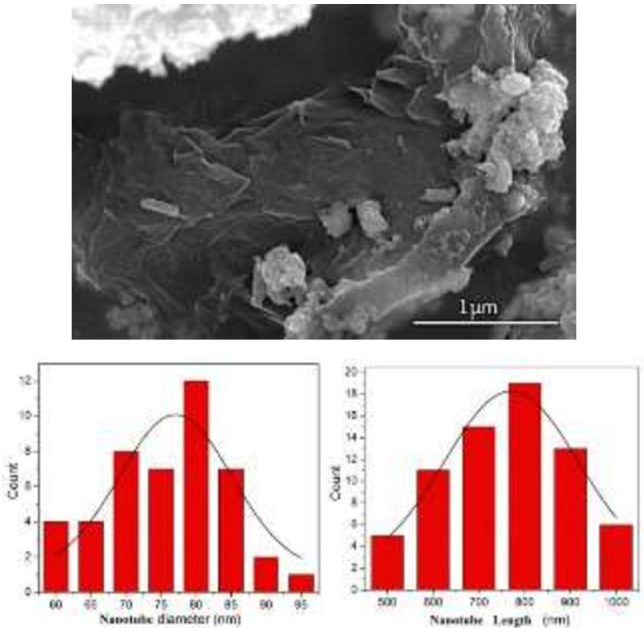

Fig. 3.5 *FESEM image of the 3.2-NT-GO-BM3nanocomposite.*

Fig 3.6 shows the FESEM image of the 3.2-NT-rGO-BM4 sample. It is found that most of the nanotubes are broken and agglomerated on the surface of GO sheets (Fig 3.6).

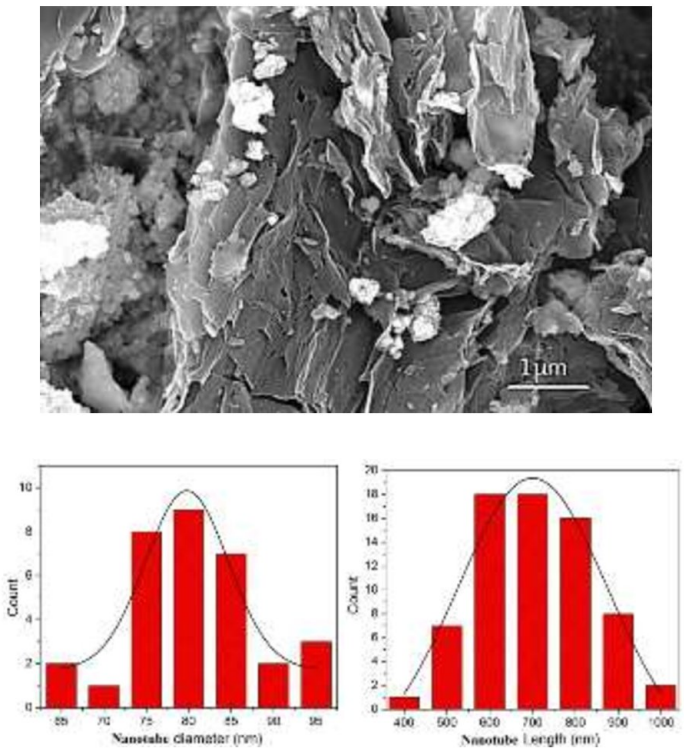

Fig. 3.6 *FESEM images of the 3.2-NT-rGO-BM4nanocomposite.*

Fig.3.7 shows the FESEM image of 8-NT- GO- BM3 sample. As shown in Fig.3.7 low diameter nanotubes of Bi_2Te_3 are spread over the surface of GO sheets.However, it can be seen that the nanotubes are broken and slightly agglomerated. The size of the nanotubes has become 900 nm as compared to the 2.4 microns before ball milling.

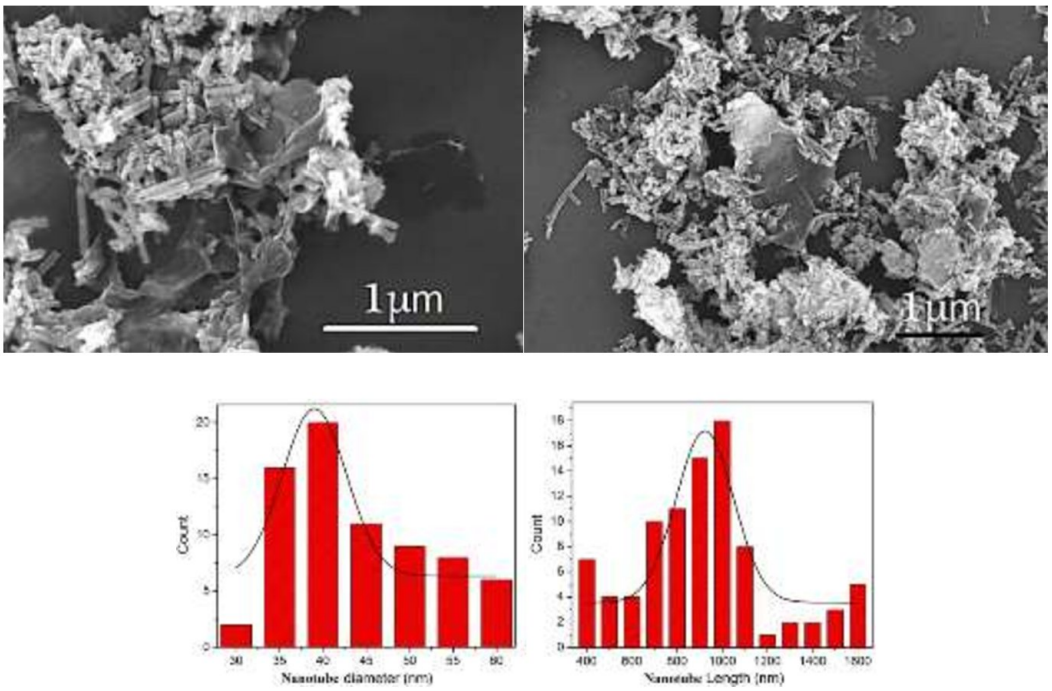

Fig. 3.7 *FESEM images of the 8-NT-GO-BM5nanocomposite.*

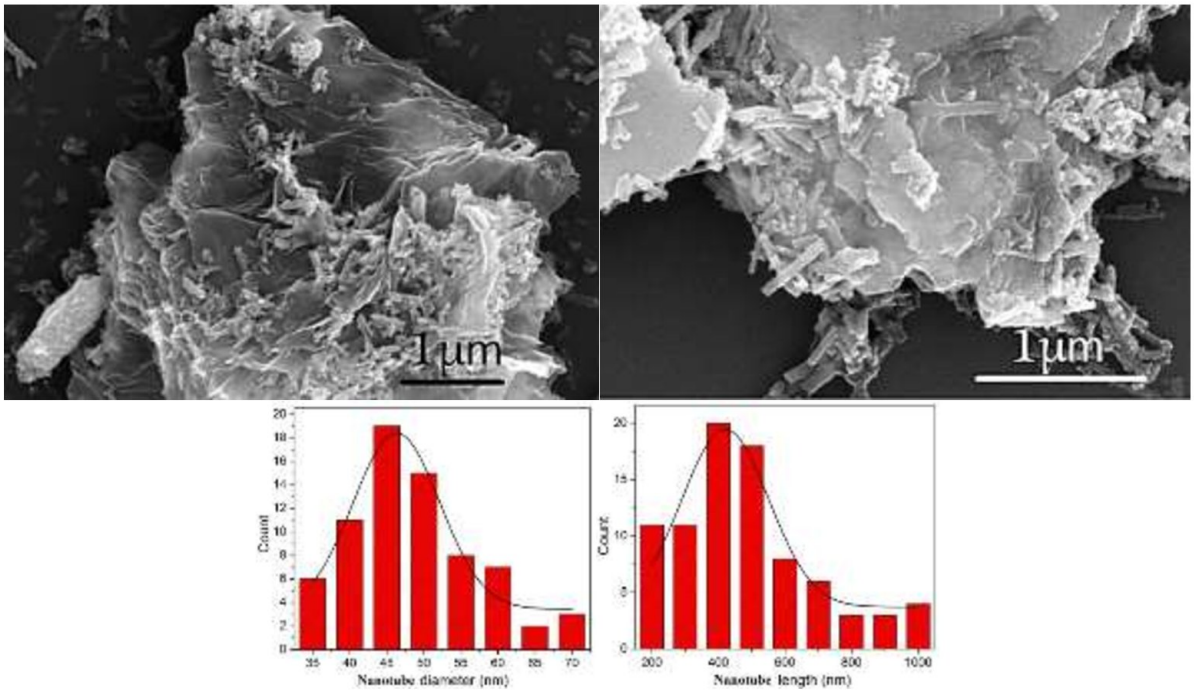

Fig. 3.8 FESEM images of the 8-NT- rGO-BM6nanocomposite.

Fig.3.8 shows the FESEM image of 8-NT-rGO-Bi_2Te_3sample. Low diameter nanotubes of Bi_2Te_3 werespread over the surface of rGO sheets.And here also the low diameter nanotubes appeared to be broken and slightly agglomerated. The length of nanotubes has become nearly 450nm as compared to the 1 micron lengths before ball milling.

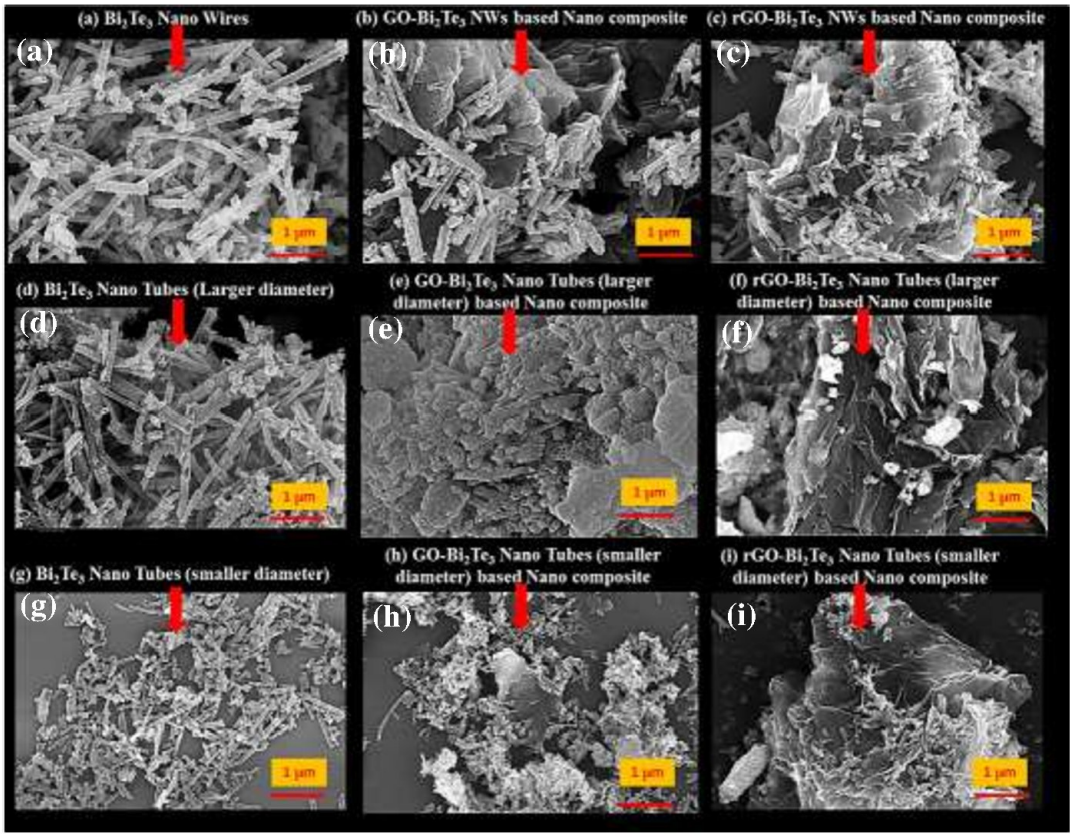

Fig.3.9 *FESEM images of (a-c) 0.8-NW neat Bi_2Te_3 NWs and the corresponding GO/rGO-Bi_2Te_3-nanocomposites, (d-f) 3.2-NT neat Bi_2Te_3 larger diameter nanotubes and the corresponding GO/rGO-Bi_2Te_3- nanocomposites and (g-i) 8-NT neat Bi_2Te_3 smaller diameter nanotubes and the corresponding GO/rGO-Bi_2Te_3-nanocomposites synthesized by the mechanical alloying method.*

The Fig.3.9 shows the comparative FESEM images of all the neat bismuth telluride materials and also the nanocomposites formed by mechanical alloying. For instance, the nanocomposites which were synthesized by employing the nanowire structure retain the nanowires (0.8-NW) morphology after the formation of nanocomposites (Fig. 3.9(b,c)).On the

contrary, the nanocomposites, those were synthesized by applying the larger diameter nanotubes (3.2-NT)do not retain the nanotubular morphology. However, smaller diameter nanotubes (8-NT) based nanocomposites still retain some level of the original structure.

Thus, the FESEM images indicate that the mechanical alloying process breaks the bismuth telluride nanotubular structure after the mechanical alloying process, possibly due to the high energetic process. Furthermore, it indicates that larger diameter nanotubes are damaged more from its original nanotubular structure (Fig.3.9 (e,f)). Hence, the morphology of the original Bi_2Te_3 nanostructures directly impacts the final morphology of the fabricated bismuth telluride nanostructured material. Moreover, it is also observed from the FESEM analysis (as shown in Fig. 3.9 (b) that no perfect contact occurs between the Bi_2Te_3 nanowires with the GO/rGO for the GO/rGO- Bi_2Te_3 nanostructured material when nanowires (0.8-NW) are employed as nanofiller. In contrast, a strong contact between the GO/rGO occurs with the Bi_2Te_3 nanostructures for the GO/rGO- Bi_2Te_3 nanostructured material when nanotubular structures (3.2-NT and 8-NT)are employed as nanofiller (Fig.3.9 (e,f,h,i)). The possible reason for the obtained result is that during the mechanical alloying process, the Bi_2Te_3 nanotubes destroyed its nanotubular structure due to its hollow nature. Thus, easily incorporated with the GO/rGO, whereas Bi_2Te_3 nanowires still retained its physical structure, as shown in Fig. 3.9(b) and (c) after the mechanical alloying process, the GO/rGO were not incorporated into the filler materials instead, they were decorated on the surface of the GO/rGO due to the hydrophobic nature of the graphene sheets.

The morphology of the bismuth telluride samples and their composites was previously shown (Fig. 3.9). However, the additional microscopic analysis was also carried out by TEM to observe the detailed morphology of all the synthesized samples. Fig. 3.10(a,d,g) shows the TEM image of the single bismuth telluride nanostructure synthesized by 0.8 mL, 3.2 mL and 8 mLRA, respectively, indicates that nanowires with the diameter about 200-250 nm are obtained when 0.8 mLRA was used on the other hand nanotubular bismuth telluride with the larger diameter about 90-120 nm and smaller diameter about 50-70 nm are obtained when 3.2 mL and 8 mLRA were utilized in the synthesis process. Thus, TEM images confirm that different one-dimensional

nanostructures such as nanowires, nanotubes with larger and smaller diameter bismuth telluride are successfully obtained by adjusting the amount of the RA, which is consistent with the FESEM results (Fig. 3.9).

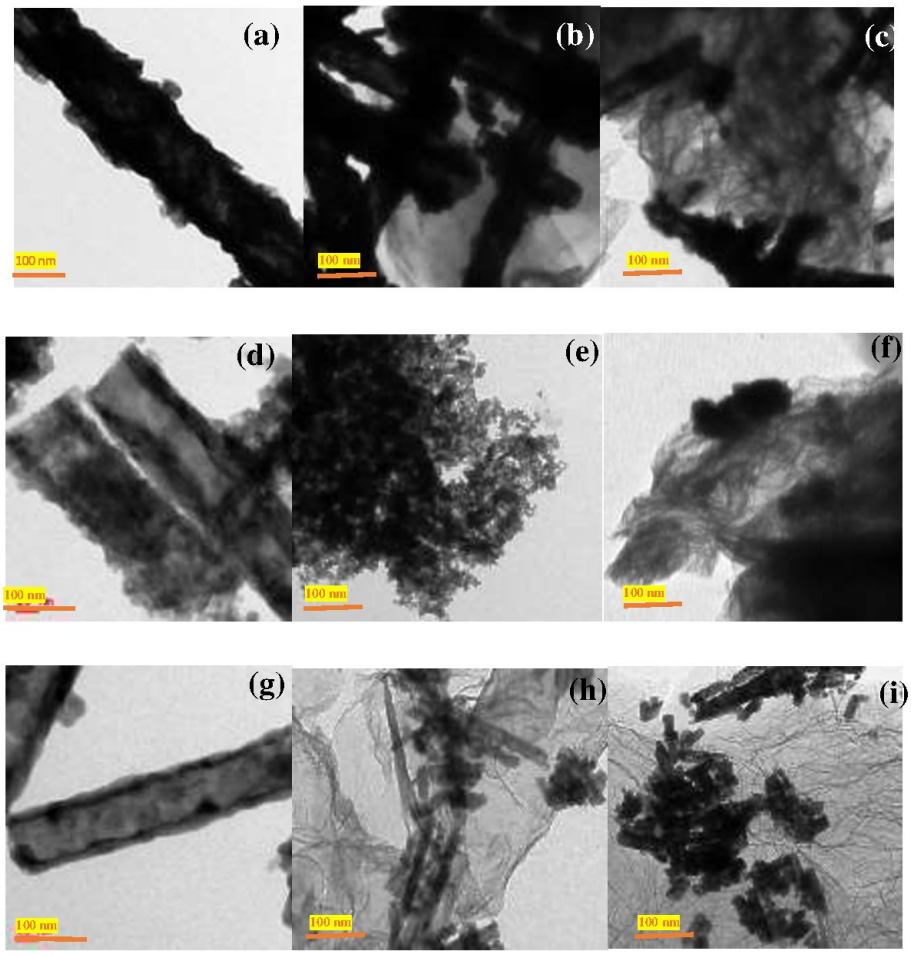

Fig. 3.10.*Comparative TEM images of (a-c) 0.8-NW neat Bi_2Te_3 NWs and the corresponding GO/rGO-Bi_2Te_3-nanostructured material, (d-f) 3.2-NT neat Bi_2Te_3 larger diameter nanotubes and the corresponding GO/rGO-Bi_2Te_3-nanostructured material and (g-i) 8-NT neat Bi_2Te_3 smaller diameter nanotubes and the corresponding GO/rGO-Bi_2Te_3-nanostructured material synthesized by the mechanical alloying method.*

Fig.3.10(b,e,h) shows the TEM images of the GO-bismuth telluride composites by employing the bismuth telluride consisting of nanowires, larger nanotubes and smaller nanotubes as source materials. It is clearly seen that when nanowires or smaller diameter nanotubes ball-

milled for preparation of the composites, nanowires and smaller nanotubes are dispersed on the surface of the GO/rGO sheets in the fabricated composites without breaking the original structure. On the other hand, when larger diameter nanotubes are ball-milled with the GO, the original nanotubular structure got destroyed as shown in Fig. 3.10(e,f) and incorporated with the GO. The same morphology is also observed for the rGO-bismuth telluride composites as shown in Fig. 3.10(c,f,i) indicating that when the nanowires and smaller nanotubes are ball-milled with rGO then their original morphology is not destroyed and dispersed on the surface of the rGO sheets. It is also noticed that nanowires and smaller nanotubes agglomerate in the fabricated composites as shown in Fig. 3.10(i) and 3.10(c). Thus nanowires and smaller nanotubes dispersed on the GO/rGO surface-based composites are obtained when nanowires and smaller nanotubes are used in the ball-milling process. In contrast, no dispersion of the larger bismuth telluride nanotubes on the GO/rGO surface is found (Fig. 3.10(e,f)), instead the larger diameter bismuth telluride are totally embedded in the composites by destroying the one-dimensional tubular nanostructure.

Thus, different morphology-based GO/rGO- bismuth telluride composites are obtained by taking bismuth telluride nanowires, smaller nanotubes, and larger nanotubes. The morphological dependent Seebeck coefficient and room temperature thermal conductivity are discussed by choosing these synthesized samples in chapter 5.

3.5 Compositional analysis by EDS

The elemental analysis was performed by using EDS on all the samples. For the sample preparation purpose, few gm of the obtained sample was dispersed on a conducting tape for the analysis. Further, gold was sputtered on the samples for FESEM-EDS analysis. Fig. 3.11 represents the EDS spectra of all the obtained ball-milled GO and RGO- bismuth telluride samples.

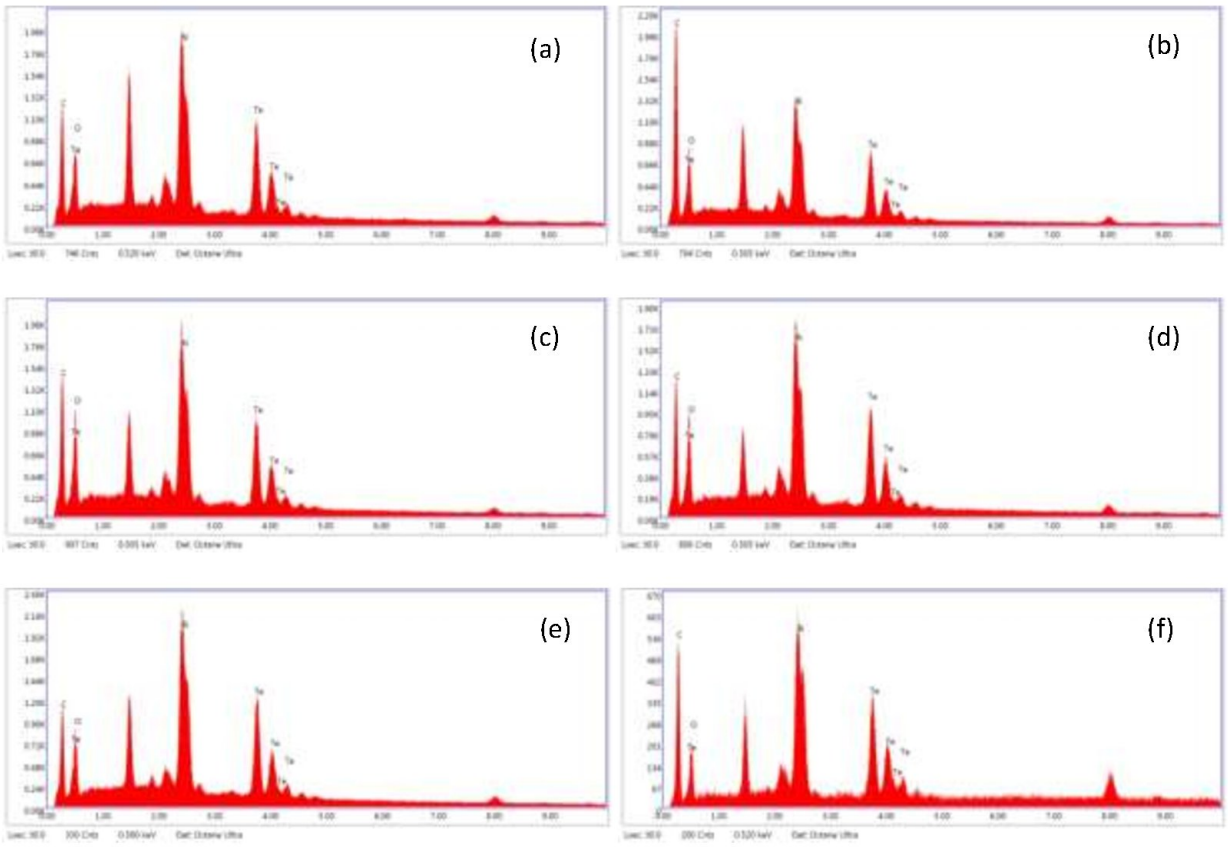

Fig. 3.11*EDS spectra of (a) 0.8NW-GO-BM1, (b)0.8NW-rGO-BM2, (c)3.2NT-GO-BM3, (d) 3.2NT-rGO-BM4, (e) 8NT-GO-BM5 and (f)8NT-rGO-BM6 samples synthesized by mechanical alloying method.*

Elemental analysis of all the nanocomposites synthesized by mechanical alloying indicates that a significant change in the percentage composition as compared to the corresponding neat Bi_2Te_3. However, the GO-Bi_2Te_3 Nanocomposites are well-formed with the large surface of Bi_2Te_3 being predominantly occupied with Graphene Oxide, hence the elemental percentage of GO-Bi_2Te_3 nanocomposites are dominated by Carbon and oxygen which is shown in table 3.2. It is due to the high surface to volume ratio of Graphene oxides and also the high affinity towards bonding with Bi_2Te_3 matrix.

Table. 3.2 EDS elemental analysis of the neat Bi_2Te_3 and the corresponding GO/rGO - Bi_2Te_3 nanocomposites synthesized by the mechanical alloying method (Wt-weight, At-Atomic, Err-Error)

Sample ID	C%		O%		Bi%		Te%	
	Wt	At	Wt	At	Wt	At	Wt	At
0.8NW-Neat Bi_2Te_3	-	-	-	-	48.32	36.34	51.68	63.66
0.8NW-GO-BM1	19.16	63.42	07.27	18.07	36.3	6.91	37.27	11.6
0.8NW-rGO-BM2	32.29	72.67	10.3	17.41	27.26	3.53	30.15	6.39
3.2NT-Neat Bi_2Te_3	-	-	-	-	50.86	38.73	49.14	61.27
3.2NT-GO-BM3	21.13	61.93	10.34	22.76	33.42	5.62	35.11	9.69
3.2NT-rGO-BM4	19.71	61.15	9.43	21.96	33.42	5.96	37.44	10.93
8NT-Neat-Bi_2Te_3	-	-	-	-	48.84	36.82	51.16	63.18
8NT-GO-BM5	16.26	59.21	7.07	19.34	36.2	7.58	40.47	13.87
8NT-rGO-BM6	24.60	69.38	7.51	15.90	31.93	5.18	35.96	9.54

The distribution of graphene and graphene oxide is non-uniform in the composite formation during the mill, which also resulted in high C% depending on the regions with more layers of GO/rGO. The following are the regions of EDS analysis of all the samples.The sample regions at which EDS analysis was performed on all the samples are shown in Fig 3.12.

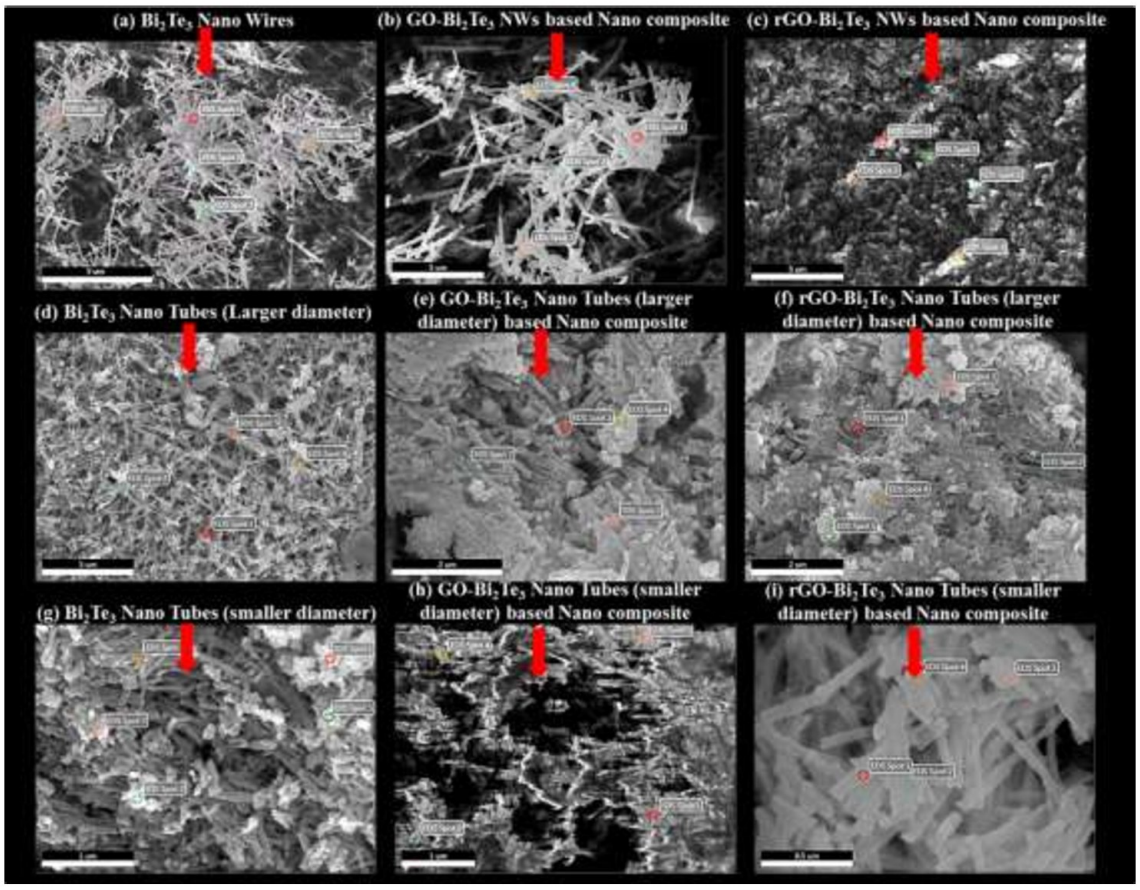

Fig.3.12 *EDS regions of (a-c) the 0.8-NW-Neat Bi_2Te_3 NWs and the corresponding GO/rGO-Bi_2Te_3nanocomposites, (d-f) the 3.2-NT-Neat Bi_2Te_3 larger diameter nanotubes and the corresponding GO/rGO-Bi_2Te_3 nanocomposites and (g-i) the 8-NT-Neat Bi_2Te_3 smaller diameter nanotubes and the corresponding GO/rGO- Bi_2Te_3- nanocomposites synthesized by the mechanical alloying method.*

3.6 RAMAN analysis

Raman spectroscopy was performed and the corresponding spectra for all the samples are shown in Fig. 3.13(a-d). It indicates that the two characteristics peak of the GO and rGO, the D peak appears at 1366cm^{-1} and the G peak at about 1600cm^{-1}[114][113], clearly indicates the formation of the GO/rGO-Bi_2Te_3 nanocomposites. Fig.3.13(d) represents the Raman spectra of all the three neat samples, which were synthesized at 0.8 mL, 3.2 mL and 8 mL reducing agent.

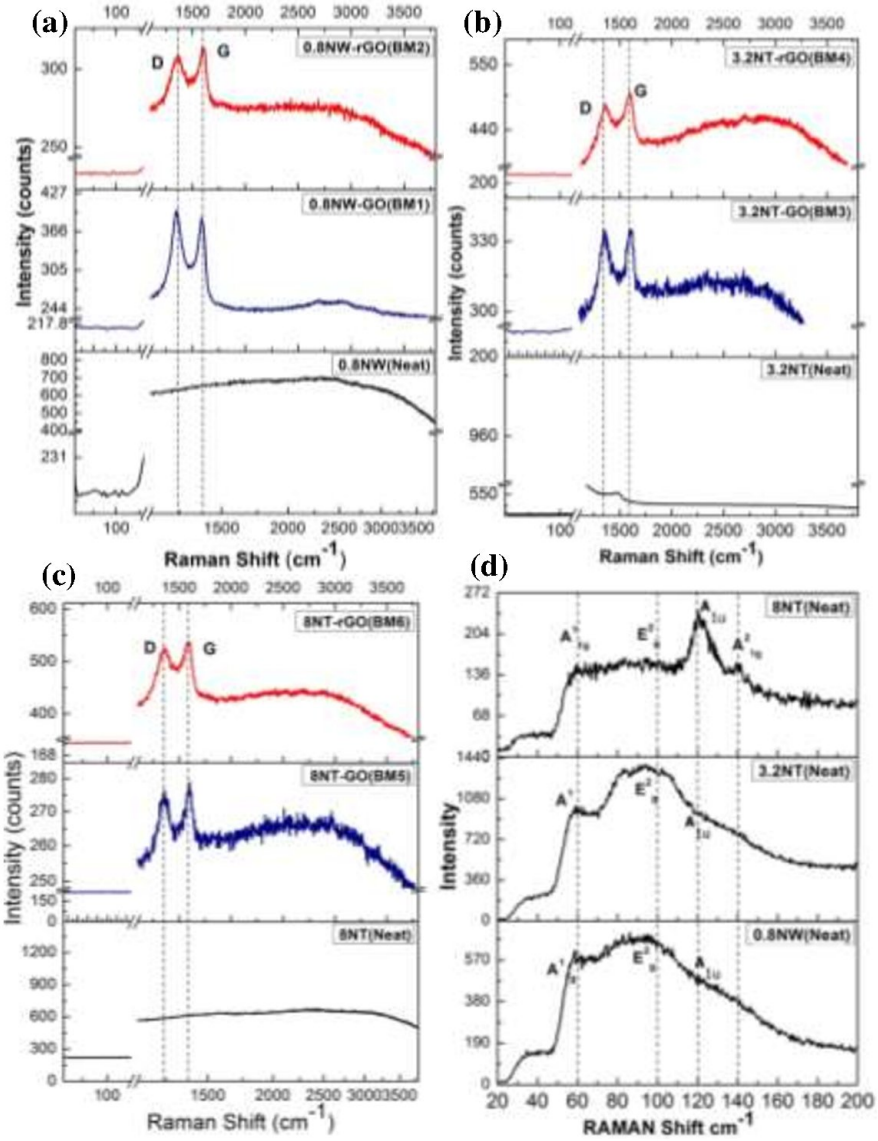

Fig. 3.13*Raman spectrum of synthesized (a) 0.8-NW neat Bi_2Te_3 NWs and the corresponding GO/rGO-Bi_2Te_3-nanocomposites, (b) 3.2-NT neat Bi_2Te_3 larger diameter nanotubes and the corresponding GO/rGO-Bi_2Te_3- nanocomposites and (c) 8-NT neat Bi_2Te_3 smaller diameter nanotubes and the corresponding GO/rGO-Bi_2Te_3-nanocomposites synthesized by the mechanical alloying method.(d) neat Bi_2Te_3 synthesized at 0.8mL, 3.2mL and 8mL RA (20-200cm^{-1} range).*

As shown in Fig. 3.13(d), the peaks appear at 60cm^{-1}, 100 cm^{-1}, 120cm^{-1} and 140cm^{-1} which correspond to A^1_{1g}, E^2_{2g}, A_{1u}, and A^2_{1g} modes, respectively. However, the Raman peaks for the A_{1u} and A^2_{1g} modes are broad for the two samples those were synthesized by using 0.8 mL (0.8-NW-Neat) and 3.2 mL(3.2-NT-Neat) reducing agent as compared to 8 mL(8-NT-Neat) reducing agent synthesized bismuth telluride sample.The possible reason for this is the decrease in the size of the nanotubes which were synthesized by using 8 mL reducing agent (8-NT-Neat).

3.7 FT IR analysis

Furthermore, to understand the molecular structure, FTIR spectra were recorded and Fig. 3.14(a-c) shows the FTIR spectra of all the neat Bi_2Te_3 and the corresponding nanocomposites. The band appears at about 3400cm^{-1} corresponds to the O-H starching vibration, at 1734cm^{-1}which corresponds to the typical stretching vibration of the C=C from the carbonyl and carboxylic groups[114][110].

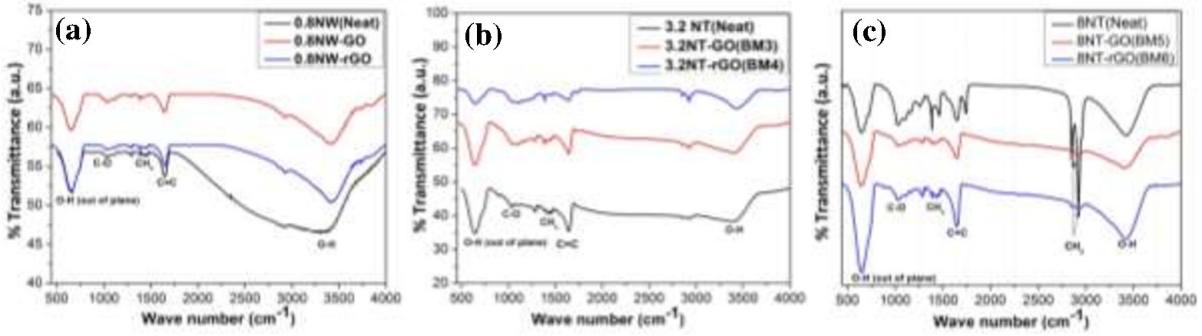

Fig. 3.14 *Typical FT IR spectra of the synthesized (a) 0.8-NW neat Bi_2Te_3 NWs and the corresponding GO/rGO-Bi_2Te_3-nanocomposites, (b) 3.2-NT neat Bi_2Te_3 larger diameter nanotubes and the corresponding GO/rGO-Bi_2Te_3-nanocomposites and (c) 8-NT neat Bi_2Te_3 smaller diameter nanotubes and the corresponding GO/rGO-Bi_2Te_3- nanocomposites synthesized by mechanical alloying method.*

The characteristic peak appears at 1200-1400cm^{-1}could be attributed to epoxy and alkoxy groups[114][110]. At 1384 cm^{-1} and 1464 cm^{-1}, the bands of CH_3 symmetric and asymmetric peaks were present. The band appears at 2900 cm^{-1} corresponds to the asymmetric stretching

mode of the CH_2 group[118]. Thus, FT IR analysis clearly indicates that all the synthesized samples consist of –COOH, C-O, CH_2, and the O-H groups, it may be possible that some of these groups are present due to the chemical synthesis process which includes washing with DI water and methanol. Furthermore, from the FT IR spectra as shown in Fig. 3.14(a-c), all the samples synthesized by employing GO as nanofiller show higher content of –OH functional groups because GO consists of –OH and –COOH group as discussed earlier.

3.8 Conclusion

Bi_2Te_3–GO/rGO nanocomposites were fabricated by using nanowires, large-diameter nanotubes and smaller diameter nanotubes of Bi_2Te_3as source materials which were mechanically alloyed with GO/rGO as nano inclusions. All the as-obtained nanocomposites were characterized by XRD, EDS, FESEM, FT IR and Raman spectroscopy for structural, compositional, morphological and molecular structure analysis.

The experimental results indicated that the high energy ball milling process breaks the larger diameter nanotubular structures during the process. Thus, possibly help to establish a strong contact between the nanofiller and matrix material as compared to the smaller diameter nanotubes. However, the nanowire structures retained its physical structure after the mechanical alloying process and mostly decorated on the surface of the graphene, which leads to no perfect contact between the filler and matrix material. Further studies of its thermoelectric properties of all the obtained nanocomposites are discussed in chapter-5.

Chapter 4

Synthesis and characterization of chemically in-situ doped GO/Bi_2Te_3 and rGO/Bi_2Te_3 nanomaterials

Chapter 4

Synthesis and characterization of chemically in-situ doped GO/Bi_2Te_3 and rGO/Bi_2Te_3 nanomaterials

4.1 Introduction

This chapter deals with the preparation of GO and rGO chemically doped bismuth telluride 1D nanomaterials by using a wet chemical rational approach. The obtained GO and rGO (discussed in **Chapter 2**) were used as dopants for this purpose. In situ chemical doping process was carried out during the synthesis of 1D bismuth telluride by rational approach. All the chemically synthesized in situ GO and rGO doped bismuth telluride nanomaterials were characterized by using XRD, RAMAN, FT IR, FESEM, TEM, and EDS for structural, morphological and compositional analysis are discussed in this chapter. The influence of different amounts of GO and rGO dopants on the structure, morphology, and composition of the obtained GO and rGO doped Bi_2Te_3nanomaterials are investigated and discussed. Thermo-physical properties of all the obtained GO and rGO doped Bi_2Te_3nanomaterials are discussed in **Chapter 5**.

4.2 Experimental procedure

20mL of ethylene glycol (EG), 0.2 gm of polyvinyl pyrrolidone (PVP MW-40000) 0.6gm of NaOH and 3 mmol of TeO_2 powder (99.999%) were taken in a three-neck flask and stirred at 160°C in N_2 atmosphere and 0.8 mL of hydrazine hydrate solution was injected into the mixture solution once the temperature of the solution reached at 160°C. After one hour of reaction, the bismuth precursor 2mmol of Bismuth (111) nitrate ($Bi(NO_3)_3.5H_2O$) and 5mL ethylene glycol solution is injected into the reaction with addition 5mg GO, the reaction was continued for another one hour. The product obtained was collected and washed several times with methanol and then DI water, then dried in a vacuum furnace at 50°C for 12 hr. This synthesis procedure is schematically explained in the flow chart as shown in Fig. 4.1.

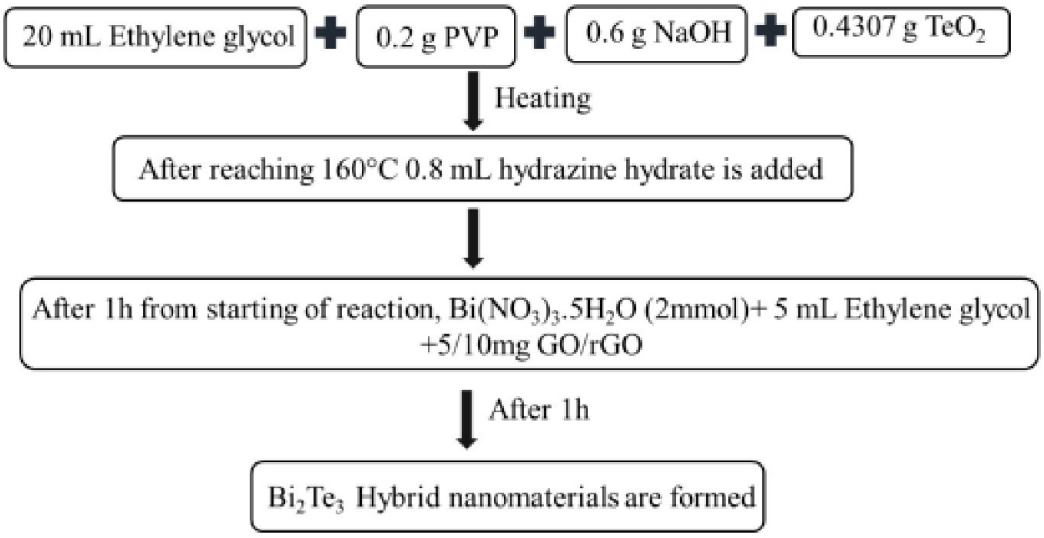

Fig. 4.1 *Flow chart for the synthesis procedure of GO/rGO doped bismuth telluride nanomaterials.*

In the same process, a set of different samples were synthesized by using 10 mg GO, 5 mg rGO and 10 mg rGO as dopants.

Table 4.1 shows the nomenclature of all the synthesized samples.

Table 4.1.Nomenclature of all the synthesized samples by using GO and rGO as a dopant.

Nomenclature of the samples		
1	0.8NW-5mg.GO(CD1)	5mg-GO doped Bi_2Te_3synthesised by using 0.8 mL RA
2	0.8NW-10mg.GO(CD2)	10mg-GO doped Bi_2Te_3synthesised by using 0.8 mL RA
3	0.8NW-5mg.rGO(CD3)	5mg-rGO doped Bi_2Te_3synthesised by using 0.8 mL RA
4	0.8NW-10mg.rGO(CD4)	10mg-rGO doped Bi_2Te_3synthesised by using 0.8 mL RA

4.3 Structural characterization by XRD

Fig.4.2(a,b) shows theXRD pattern of the neat Bi_2Te_3 TE NWs and GO doped Bi_2Te_3 TE and rGO doped Bi_2Te_3 TE samples. As shown in Fig. 4.2(a), no strong GO peaks are present in the XRD pattern of 5mg GO doped Bi_2Te_3 TE sample (CD1). However, a small peak appears near to 24^0 for the 10mg GO doped Bi_2Te_3 TE sample (CD2). A small peak appears at 10^0 for all the samples such as 0.8NW- Bi_2Te_3 (neat), CD2 and CD1 (as shown in Fig. 4.2(a)). Since rGO peak appears at 24^0 as shown in Fig. 4.2(a), it is possible that GO could be reduced to rGO during the synthesis process when 10 mg GO acted as the dopant. When rGO was employed as dopant, the identical XRD pattern is observed as shown in Fig. 4.2(b). A small peak appears at 24^0which corresponds to the rGO peak [113].The identical XRD pattern for the GO-doped Bi_2Te_3 TE and rGO-doped Bi_2Te_3 TE indicates that GO possibly reduces to rGO during the synthesis process. All the XRD peaks corresponding to Bi_2Te_3 NWs as shown in Fig. 4.2(a,b)arein good agreement with the earlier reported result (*JCPDS no. 080021*).

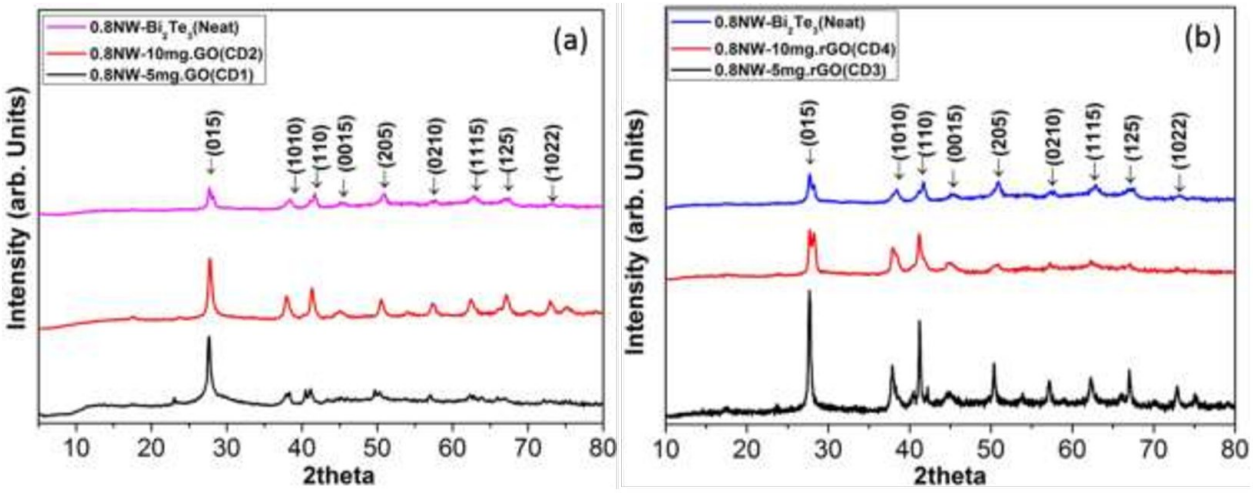

Fig. 4.2 *X-ray diffraction pattern of (a) 0.8NW- Bi_2Te_3(neat), CD1,CD2and (b)0.8NW- Bi_2Te_3(neat), CD3, CD4 samples.*

Table 4.2.The lattice parameter of GO/rGO doped Bi_2Te_3 and neat bismuth telluride samples.

Sample ID	a (Å)	c (Å)
0.8NW-5mg.GO(CD1)	4.38	30.78
0.8NW-10mg.GO(CD2)	4.37	30.09
0.8NW-5mg.rGO(CD3)	4.37	30.38
0.8NW-10mg.rGO(CD4)	4.38	29.84
0.8NW-Neat Bi_2Te_3	4.33	29.30

The lattice parameters of all the samples were calculated by using the standard method [116] and presented in table 4.2. As shown in the table, lattice parameters (mainly a) increases after doping with GO or rGO. These results indicate that the incorporation of GO and rGO as dopant creates lattice strains in the cell and that leads to change in lattice parameters.

4.4 Morphological characterization by FESEM and TEM

4.4.1 FESEM

Morphological characterization was carried by using FESEM NOVANANOSEM for all the GO/rGO doped bismuth telluride nanomaterials.The FESEM image of 0.8NW-5mg.GO (CD1) sample is shown in Fig. 4.3(a,b). As shown in Fig. 4.3(a,b), nanorods are agglomerated and the average size is about 90 nm to 100 nm diameter. It is seen from Fig. 4.3 that this sample shows a nanowire morphology with ~2µm length.

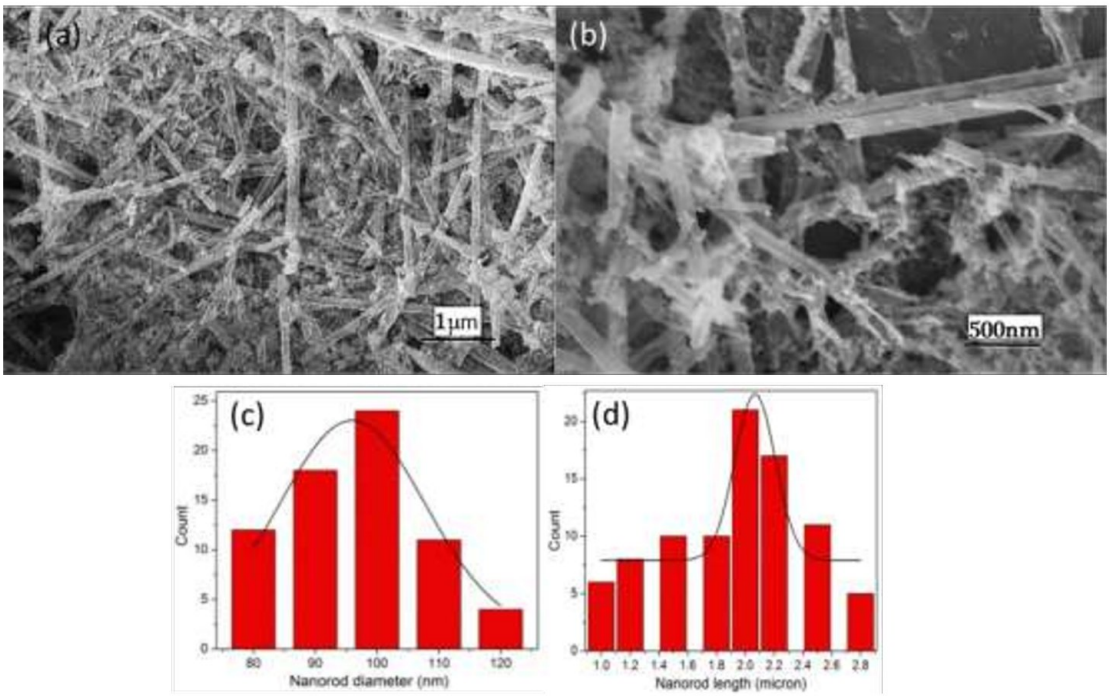

Fig. 4.3 *FESEM images of as-synthesized 0.8NW-5mg.GO(CD1) sample.*

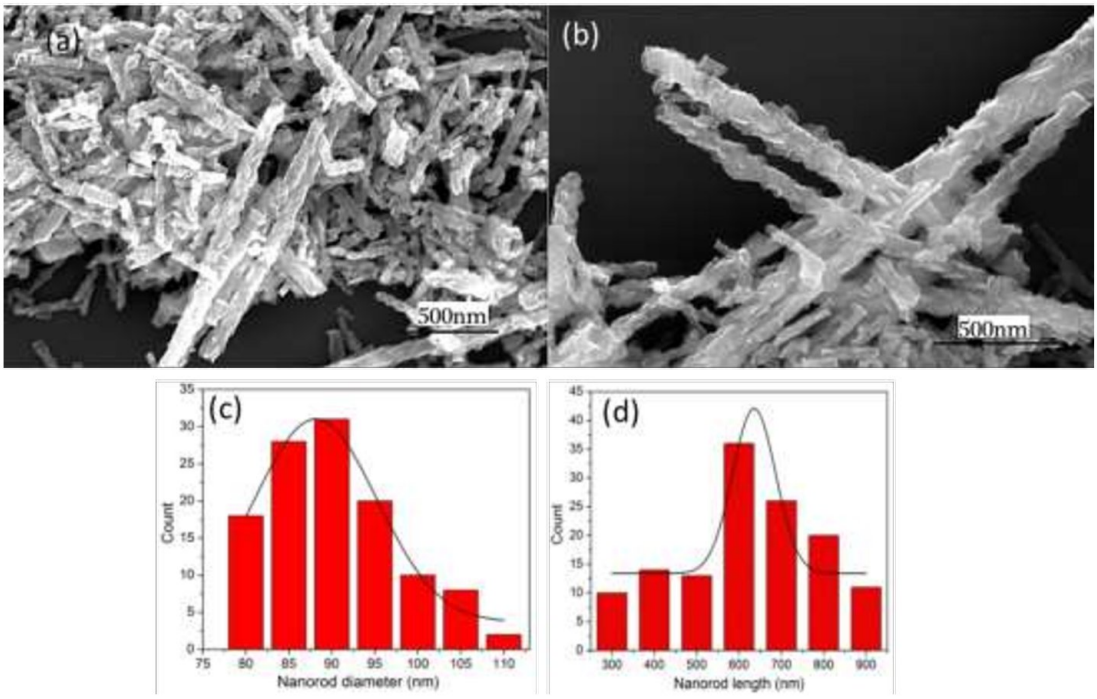

Fig. 4.4 *FESEM images of as-synthesized 0.8NW-10mg.GO(CD2) sample.*

Fig. 4.4 shows the FESEM images of 0.8NW-10mg.GO(CD2) sample. As shown in Fig. 4.4(a,b), the nanowires have rough morphology and the average diameter and average length are about 85 nm and 650 nm, respectively.

The FESEM images of 0.8NW-5mg-rGO(CD3) sample are shown in Fig. 4.5. As shown in the figure, the nanowires look rough surface and not agglomerated. The average length of nanowires is about 2 microns and the average diameter is about 110 nm. From Fig. 4.5, it can be seen that there is a chain-linked platelet formation of nanowires.

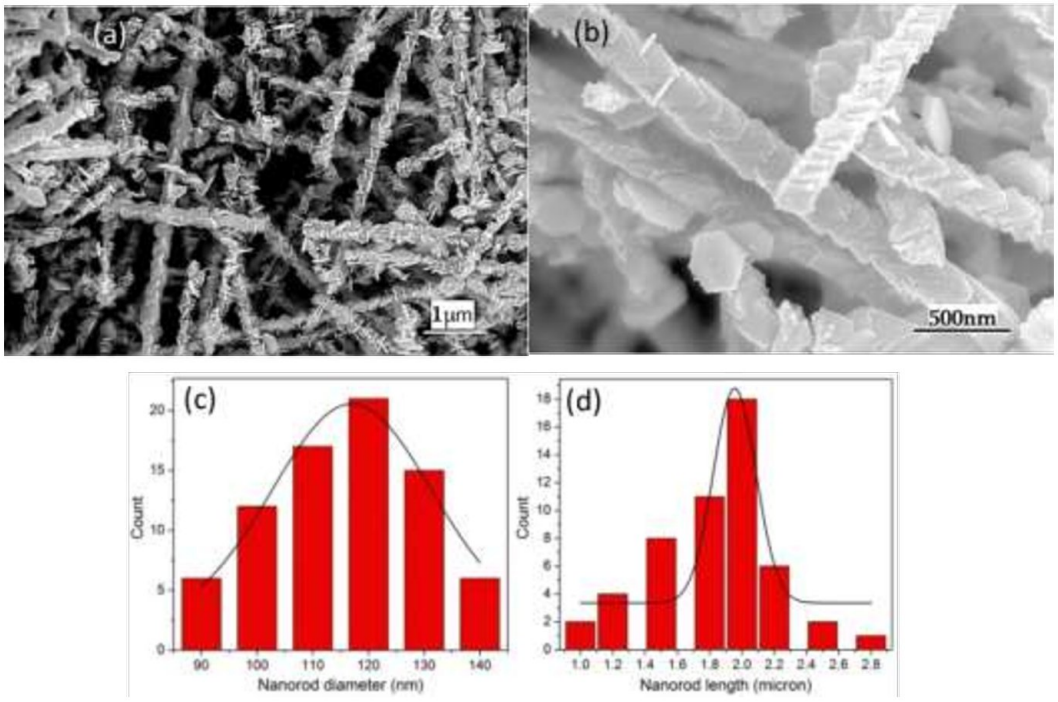

Fig. 4.5 *FESEM images of the as-synthesized 0.8NW-5mg-rGO (CD3) sample.*

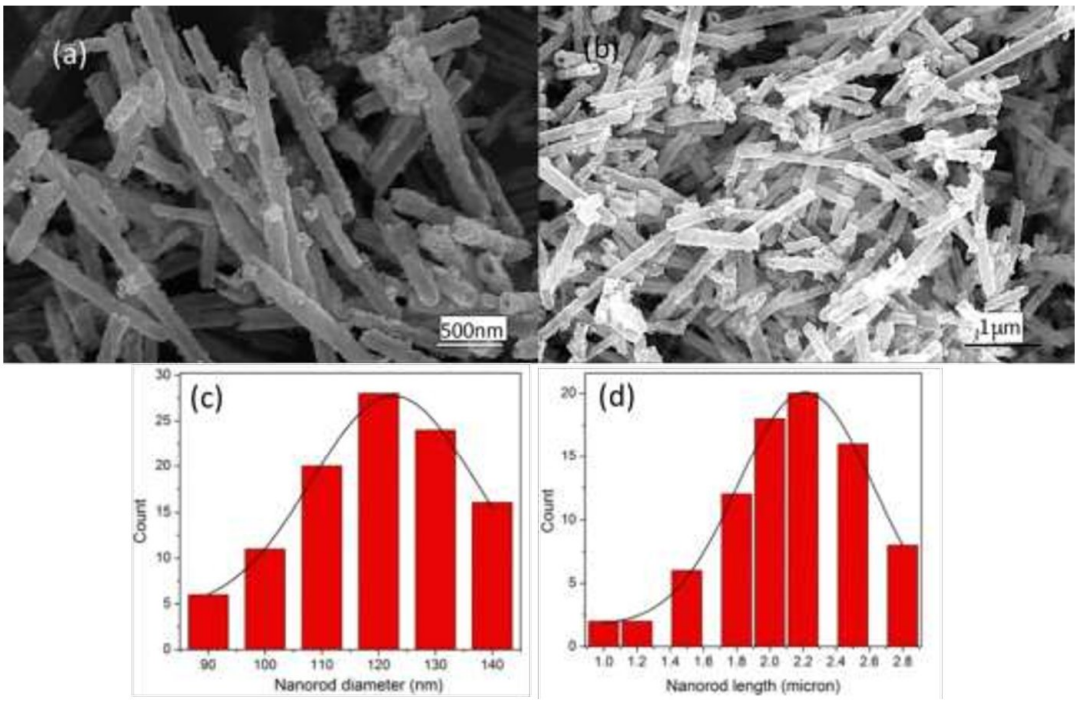

Fig. 4.6 *FESEM images of the as-synthesized 0.8NW-10mg-rGO (CD4) sample.*

FESEM images of 0.8NW-10mg-rGO (CD4) sample are shown in Fig. 4.6. It is observed that the surface of the nanorods is very rough in morphology and appears to be platelets linked in chain form. The average length of nanowires is about 2 microns and the average diameter is about 110 nm.

It is clearly observed from the FESEM images as shown in Fig. 4.7 that the amounts of GO and rGO doped into the bismuth telluride plays a key role in the morphology of each sample. 5mg-GO CD1 seems to be the smoother in the surface as compared to the other two samples as shown in Fig. 4.7.

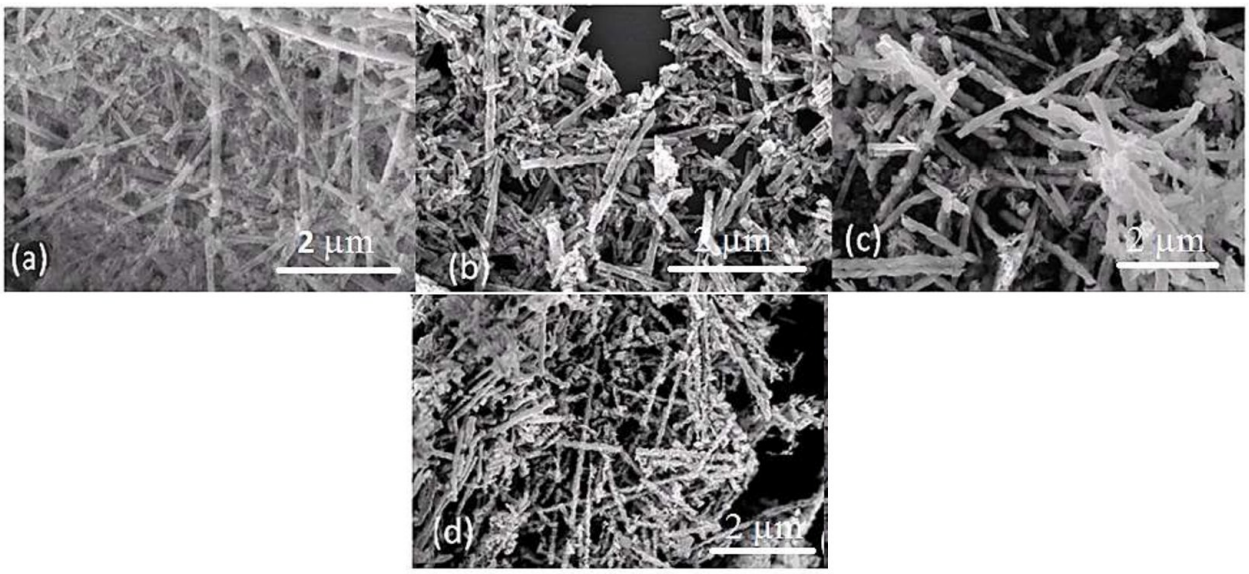

Fig. 4.7 *Field emission scanning electron microscopy images of (a) 5mg-GO CD1 (nanowires),(b) 10mg-GO CD2 (nano-screw), (c) 5mg-rGO CD3 (nanoplates/ nanowires), (d) 10mg-rGO CD4 (nanotubes).*

Thus the experimental results indicate that by increasing the concentration of dopant either GO or rGO, the morphology of the obtained final nanostructure changes and the surface becomes rougher. For instance, when rGO acts as dopant then chain-linked platelet morphology is obtained. As the amount of rGO increases to 10 mg (twice) then different morphology is observed a shown in Fig. 4.7. Therefore, the comparative FESEM images of all the samples reveal that GO and rGO doping into bismuth telluride have a morphological effect on the matrix bismuth telluride TE materials as the remaining synthesis parameters are same for all the four syntheses.

4.4.2 TEM

The morphology of the obtained GO/rGO doped bismuth telluride 1D nanomaterials was further analyzed by TEM, HRTEM and SAED analysis for all the samples.

TEM images, HRTEM images and SAED pattern of 0.8NW-5mg GO (CD1) were shown in Fig. 4.8. From Fig. 4.8 (a,c) nano agglomerates were found around the nanowires which are

also evident from the FESEM investigations. Fig. 4.8 (c & d) shows the HRTEM images, it is found that the interplanar distance corresponding to the major peak of $Bi_2Te_3$is 0.31nm. The SAED pattern clearly shows the (10220) and (205) planes from the Bi_2Te_3;

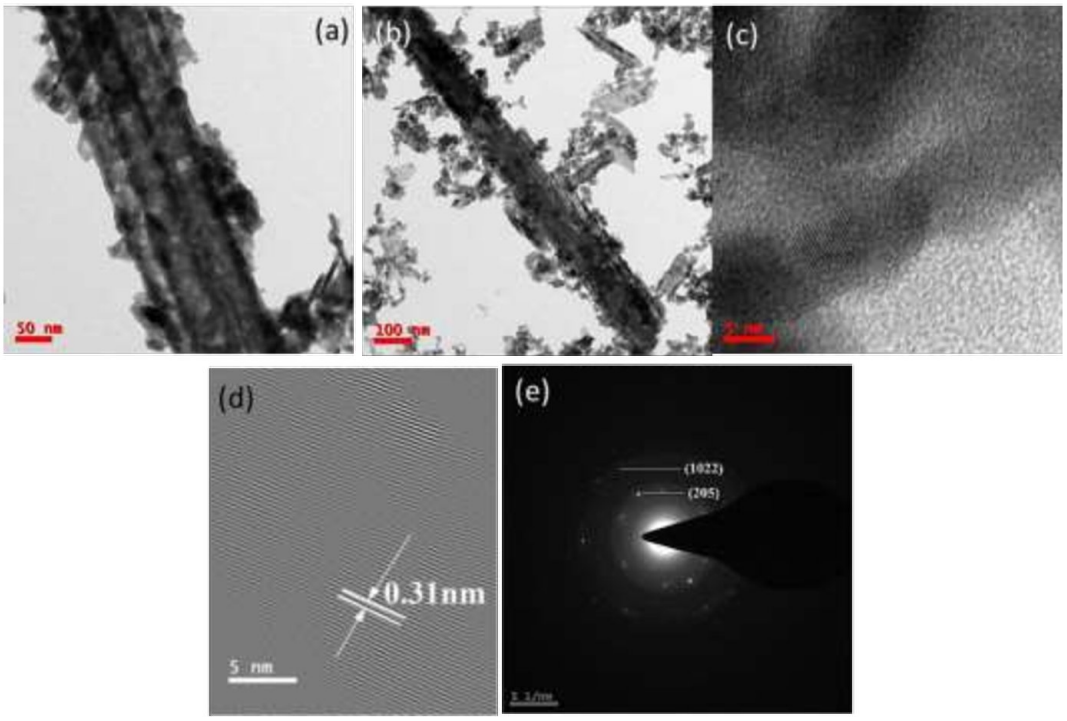

Fig. 4.8*(a & b) TEM, (c & d) HRTEM images and (e) SAED pattern of 0.8NW-5mg.GO (CD1) sample.*

Fig. 4.9 shows the TEM images, HRTEM images and SAED pattern of 0.8NW-10mg GO doped Bi_2Te_3(CD2) sample. The rough morphology along with the chain-linked platelets, is clearly seen in Fig. 4.9 (a,b) and the particles of GO seem to be decorated on the surface of the nanorods. From the HRTEM images (Fig. 4.9 c & d) the interplanar arrangements corresponding to bismuth telluride and GO are found and interplanar distance corresponding to the peak of the $Bi_2Te_3$is 0.32 nm. The interplanar distance of the GO is found to be 0.54 nm. The SAED pattern (Fig 4.9 c) shows (015) and (002) planes of Bi_2Te_3. The d-spacing related to GO are present in the material which indicates the formation of hybrid GO doped nanowires; it also shows the interface between GO and the Bi_2Te_3nanorods due to the embedment of GO in the matrix bismuth telluride.

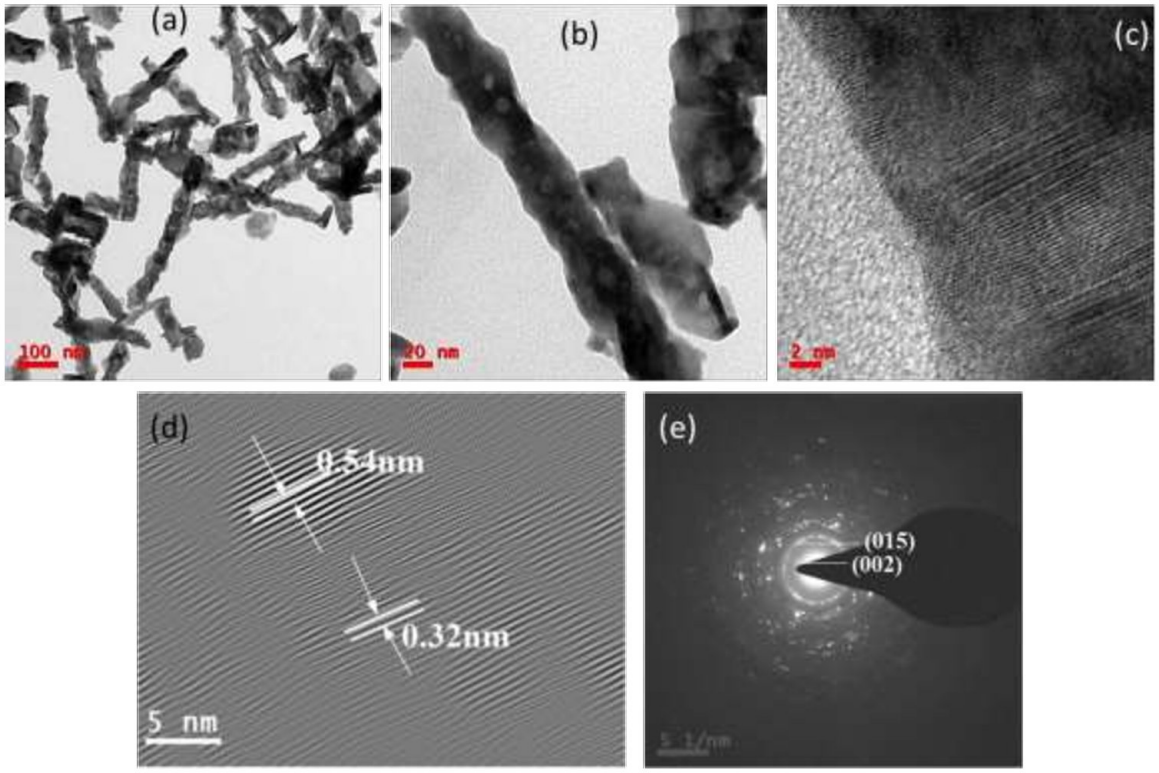

Fig. 4.9*(a & b) TEM, (c & d) HRTEM images and (e) SAED pattern of 0.8NW-10mg-GO (CD2) sample.*

TEM, HRTEM and SAED pattern of 0.8NW-5mg-rGO (CD3) sample were shown in Fig. 4.10. The chain-linked structure formed by the platelets of Bi_2Te_3 nanowires is clearly observedas shown in Fig. 4.10 (a,b) which is also observed in the corresponding FESEM images. It is also seen that there are very fewer agglomerates and rGO is found surrounding the nanowires. From the HRTEM images, interplanar distance is found to be 0.31 nm corresponding to the crystal plane of the Bi_2Te_3. The interplanar distance of the rGO is also found to be 0.35 nm. The SAED pattern (Fig 4.10 e) shows the (015) and (002) planes of Bi_2Te_3. The d-spacings related to rGO are embedded in the matrix Bi_2Te_3material which shows the formation of hybrid rGO doped 1D bismuth telluride.

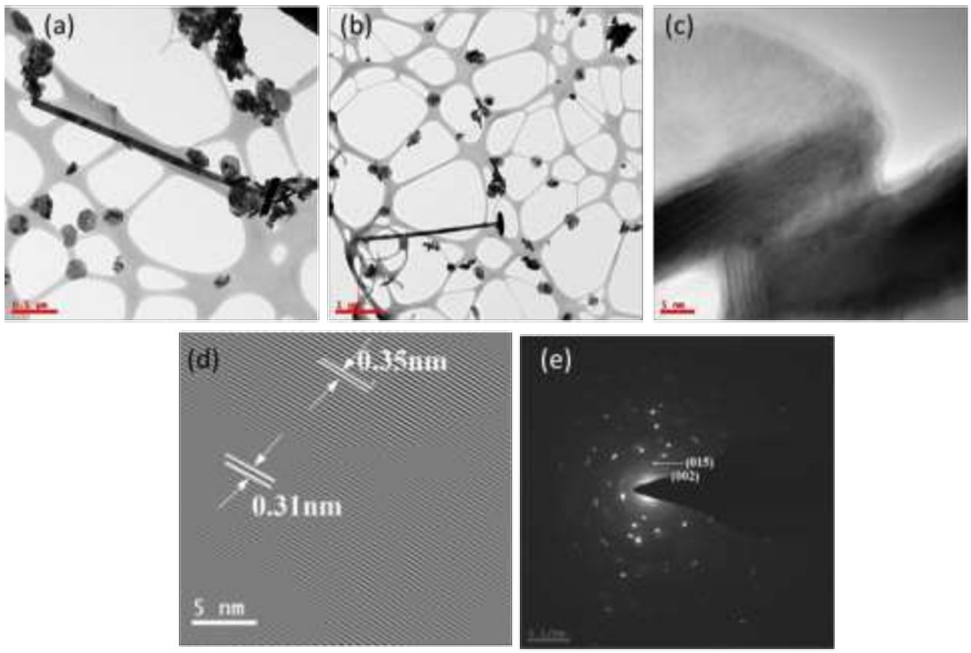

Fig. 4.10*(a & b) TEM, (c & d) HRTEM images and (e) SAED pattern of 0.8NW-5mg-rGO (CD3) sample.*

TEM, HRTEM and SAED patterns of 0.8NW-10mg-rGO (CD4) are shown in Fig. 4.11and it has found the similarity from its corresponding FESEM images. The chain-linked structure formed by the platelets of Bi_2Te_3 into nanorods is also observed as shown in Fig. 4.11 (a,b). It is also seen that there are fewer agglomerates and the rGO is surrounded to the nanorods. From the HRTEM images (Fig. 4.11 c,d) interplanar arrangements of bismuth telluride and the reduced graphene oxide are observed. The interplanar distance corresponding to the crystal plane of the $Bi_2Te_3$is found to be 0.28 nm and the interplanar distance of the rGO is about 0.35 nm. The interface between the bismuth telluride and the reduced graphene oxide is also identified as shown in Fig. 4.11 (d). The SAED pattern clearly shows the (015) (010) and also (002) planes corresponding to Bi_2Te_3. The d-spacings related to rGO are embedded in the matrix Bi_2Te_3material indicates the formation of hybrid rGO doped nanorod.

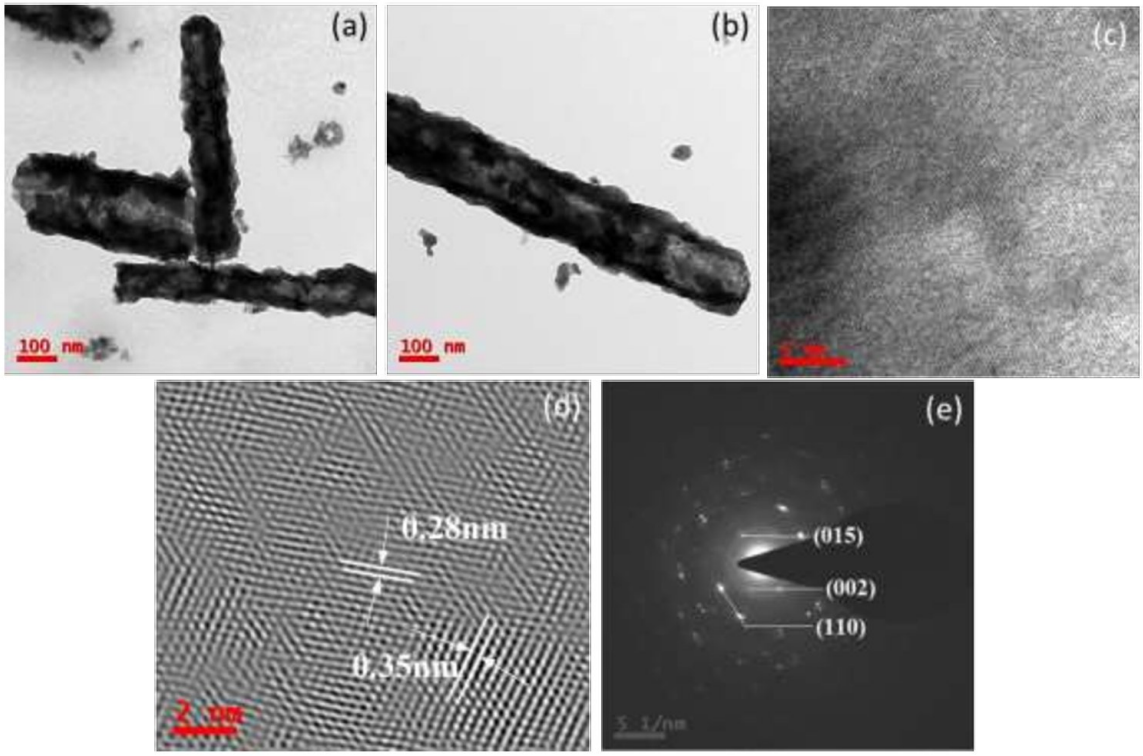

Fig. 4.11 *(a &b) TEM, (c &d) HRTEM images and (e) SAED pattern of 0.8NW-10mg.rGO (CD4) sample.*

4.5 Compositional analysis by EDS

The elemental analysis of all the obtained samples was carried out by using Energy dispersive X-Ray spectroscopy (EDS) and it is shown in table 4.3. The EDS analysis of all the doped samples was compared with the undoped neat bismuth telluride sample and it was found that significant C and O percentage in the GO and rGO doped samples. It is also found that 0.8NW-10mg-rGO (CD4) sample possesses less % of O as compared to other doped samples. It is earlier reported that possibly the Van der Waal bonding between the Te-Te is replaced by GO or rGO dopant,thus there is a significant reduction in Te% in doped samples. Therefore, after doping GO/rGO into the 1D bismuth telluride, nanowires have become bismuth rich; this also shows the formation of GO/rGO-Bi_2Te_3 hybrid 1D TE materials.

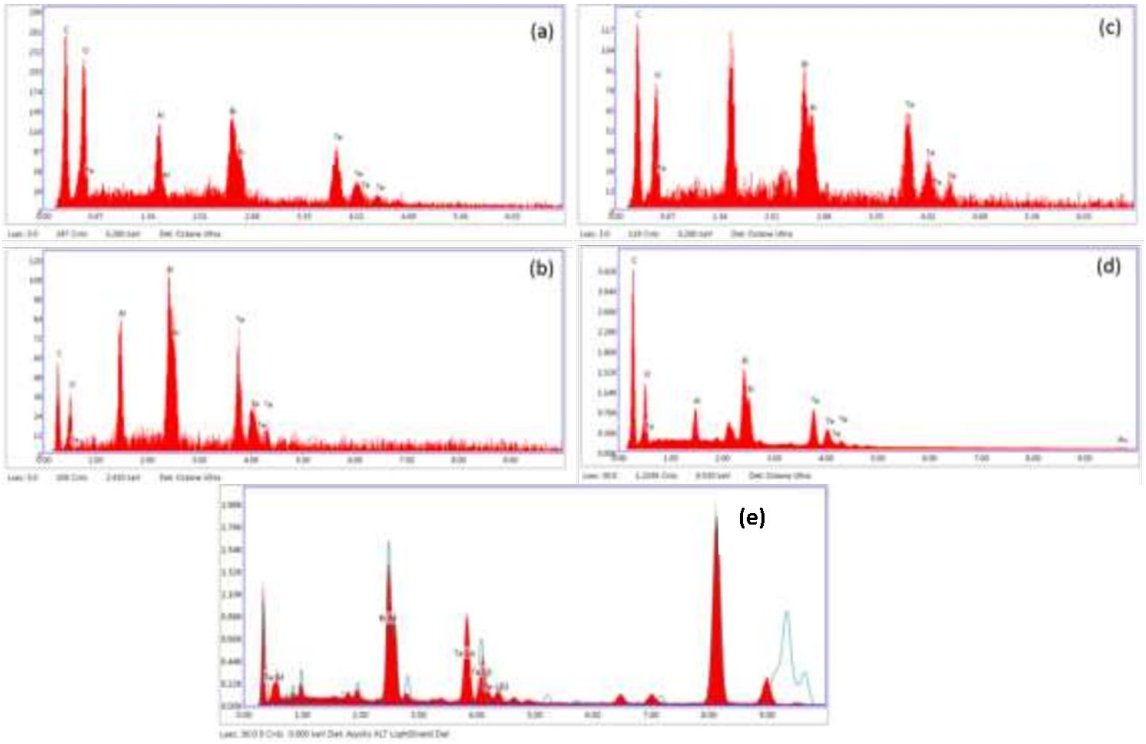

***Fig. 4.12**, EDS spectra of (a)0.8NW-5mg-GO (CD1), (b) 0.8NW-10mg-GO (CD2), (c) 0.8NW-5mg-rGO (CD3), (d) 0.8NW-10mg-rGO (CD4) and (e)0.8 NW neat*

Table 4.3 Compositional analysis of neat Bi_2Te_3 and GO or rGO doped Bi_2Te_3 TE nanomaterials.

Sample ID	C%	O%	Bi%	Te%
0.8NW-5mg.GO(CD1)	13.42	7.63	30.73	48.21
0.8NW-10mg.GO(CD2)	8.65	3.23	42.14	45.97
0.8NW-5mg.rGO(CD3)	9.20	4.17	29.13	57.46
0.8NW-10mg.rGO(CD4)	7.37	0.08	33.07	59.44
0.8NW-Neat Bi_2Te_3	-	-	34.29	65.71

4.6 RAMAN analysis

Fig. 4.13 (a-c) shows the Raman spectra of 0.8 neat Bi_2Te_3NW, GO/rGO, GO/rGO-doped Bi_2Te_3 samples and Fig. 4.13 (d) shows Raman spectra of obtained GO/rGO-doped bismuth telluride samples in the wavenumber range of 1300 cm^{-1} to 1650 cm^{-1}. As shown in Fig. 4.13 (a) the Raman bands appear at 60cm^{-1}, 100cm^{-1}, 120cm^{-1} and 140cm^{-1} correspondings to A^1_g, E^2_g, A^1_u and A^2_{1g} modes of bismuth telluride sample[112].

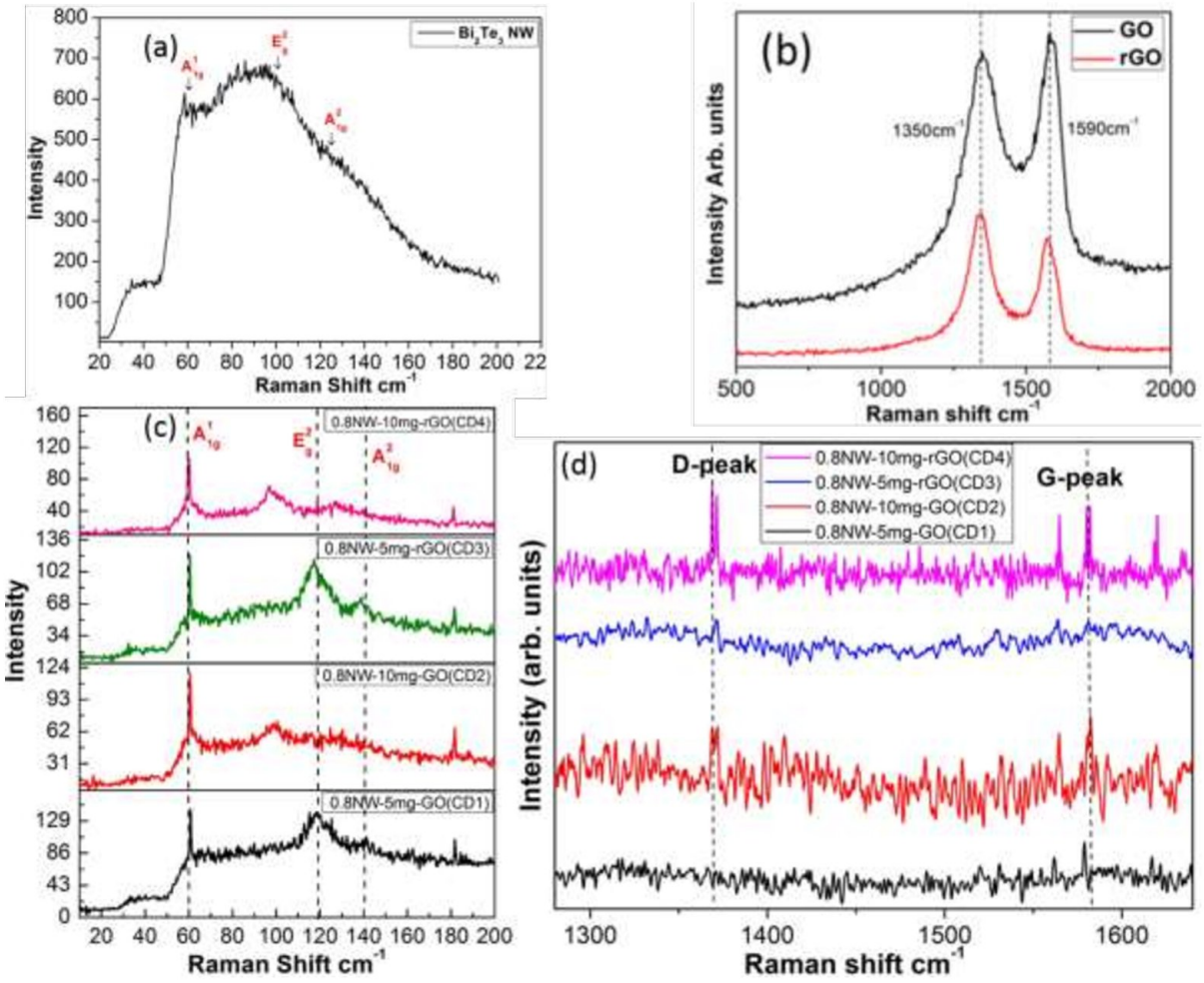

Fig 4.13 *Raman spectra of (a) 0.8-NW Neat Bi_2Te_3 nanorods, (b) GO and rGO and (c) and (d) GO/rGO-Bi_2Te_3 Hybrid materials.*

It is seen from Fig 4.13 (b), that both the G and D peaks appear at 1350cm^{-1} and 1590cm^{-1} for the as-synthesized GO and rGO samples[114]. It is also seen from the Fig 4.13 (d) that all the GO or rGO-doped samples show the D and G-peak, which indicates that GO or rGO is doped with the bismuth telluride by chemical synthesis approach. These results also indicate that some of Raman bands do not appear in the Raman spectra after doping with GO and rGO. It also depends on the concentration of dopant added into the matrix bismuth telluride materials.

4.7 FTIR analysis

Fig. 4.14 shows the FTIR spectra of all the synthesized samples. Fig. 4.14 shows different bands appearing at 1653cm^{-1} , 640 cm^{-1} 2855cm^{-1},3550cm^{-1} as shown in Fig. 4.14 corresponds to C=C, C-O, C=C, C=O and also the O-H. The FTIR spectra of all doped samples are compared with neat GO, neat rGO and neat bismuth telluride FTIR spectra.The presence of hydroxyl (C-OH) and carboxyl (-COOH) bonds in neat bismuth telluride samples is possibly due to the involvement of D.I water and methanol in the cleaning process.It is also found from the Fig 4.14 that bands appear at O-H at 640 cm^{-1}, C-O at 1029 cm^{-1}, C-C at 1195 cm^{-1}, -CH_3(Symmetric deformation) at 1387 cm^{-1}, -CH_3(Asymmetric deformation) at 1468 cm^{-1}, C=C at 1653 cm^{-1}, C=O at 1752 cm^{-1}, -CH_2- (Symmetric stretch) at 2855 cm^{-1}, -CH_2-(Asymmetric stretch) at 2933 cm^{-1}, O-H at 3550 cm^{-1}.The experimental analysis indicates that when the amount of dopant either GO or rGO is higher (i.e., 10mg), then the lesser the –OH groups present in the doped samples. It is due to the possible reduction of GO to rGO during the synthesis process and rGO-doped bismuth telluride nanostructures are obtained.

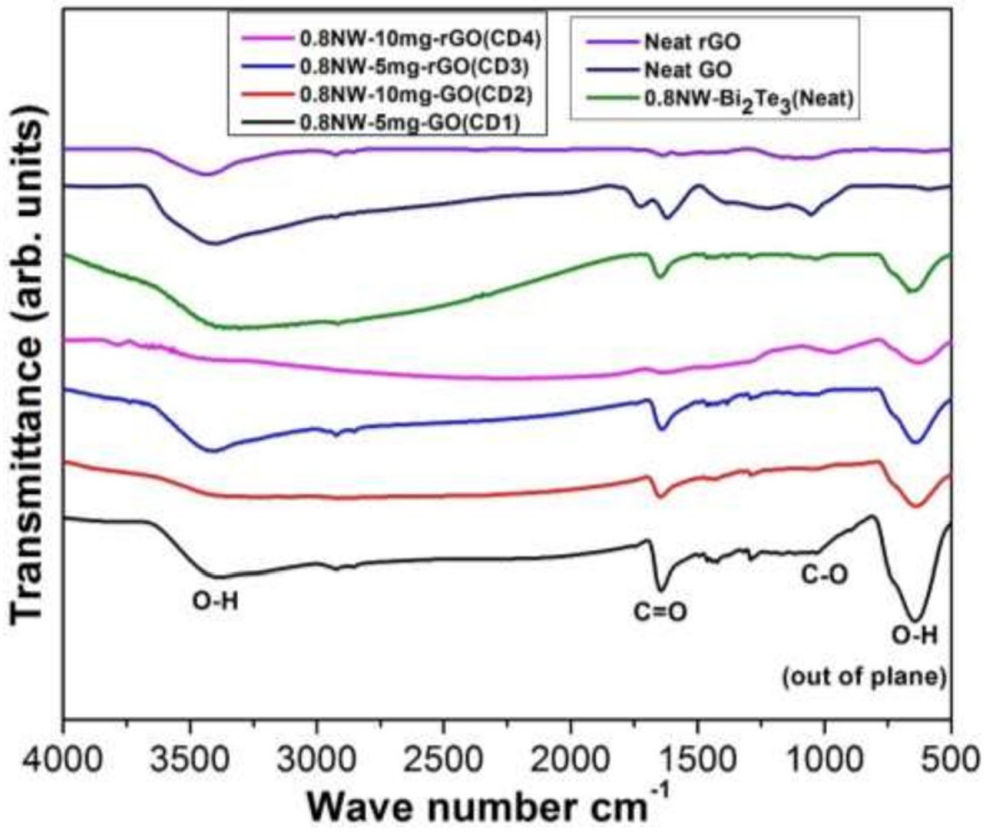

Fig 4.14*Combined FTIR spectra of neat GO, neat rGO, GO-rGO/Bi_2Te_3 nano-composite and 0.8NW-neat Bi_2Te_3 nanorods.*

4.8 Conclusion

In conclusion, GO and rGO doped bismuth telluride nanostructures were synthesized by using the in-situ chemical rational approach. Different amounts of GO and rGO such as 5 mg and 10 mg were used to investigate the impacts of the chemical doping process on the structure, morphology and composition of the GO and rGO doped bismuth telluride nanostructures. Our experimental results revealed that different morphologies of 1D TE nanomaterials such as nano-screws, nanoplates/nanowires, and rough surface thick wall nanotubes could be obtained by controlling the concentration of the dopants(GO/rGO). Compositional analysis indicated that composition could be controlled in a better way when rGO directly acts as dopant instead of

using GO as a dopant. Moreover, a higher percentage of oxygen is incorporated in the sample when GO acts as dopant as compared to rGO. On the other hand, the oxygen percentage is very less when a higher amount of rGO acts as a dopant. Furthermore, XRD and Raman analysis indicate that GOs are mostly reduced to rGO during the in-situ doping synthesis process. The obtained GO and rGO doped bismuth telluride samples were investigated for further thermo-physical properties such as density, Seebeck coefficient, electrical conductivity, thermal conductivity are discussed in the next chapter.

Chapter 5

Thermo-physical properties of all GO and rGO based bismuth telluride cold-pressed nanostructured materials

Chapter 5

Thermo-physical properties of all GO and rGO based bismuth telluride cold-pressed nanostructured materials

5.1 Introduction

In the previous chapters, different ways of fabricating GO/rGO-bismuth telluride nanomaterials have been discussed. In this chapter, thermo-physical properties like the density, electrical conductivity, Seebeck coefficient and the thermal conductivity of all the obtained neat bismuth telluride, GO and rGO base bismuth telluride cold-pressed TE materials are discussed.

Two different dies (6 and 10mm diameters) were used for the preparation of the samples for the density, electrical conductivity, Seebeck coefficient and thermal conductivity measurements. The dies were filled with approximately 50 mg for 6 mm die and 125 mg and then cold-pressed by applying a load of 1.5 and 4Tonne, respectively. Each sample collected from the die was thermally heated for 12 hr at 200°C by using a vacuum furnace. Cold-pressed process was carried out in the present work to retain the nanotubular morphology after the preparation of the pallet samples due to the possibility of damage of the nanotubes embedded in the bulk nanostructured samples. All the cold-pressed samples were then collected from the vacuum furnace and their thermo-physical properties were investigated and comparatively presented in this chapter.

5.2 Measurement of Density

5.2.1 Experimental procedure:

For measurement of density, the weight of each cold-pressed samples was measured by using a digital weighing balance with 0.0001 gm error and thickness of each sample were measured by using a digital micrometer with an error of 0.001 mm. Then densities of all the cold-pressed neat and GO/rGO based bismuth telluride nanostructured samples were calculated

by using the formula Density=Mass/Volume. All thecalculated values of mass, volume and densities are shown in Table 5.1.

5.2.2 Densities of all the samples

Table 5.1 Calculated densities of all the obtained neat bismuth telluride, mechanically ball milled and in situ doped Go/rGO-bismuth telluride cold-pressed samples.

Sample ID	Mass (g)	Volume (cm^3)	Density g/cm^3 (Bulk density of the standard reported sample-7.7 g/cm^3)[119]	Relative density
0.8-NW-Neat	0.120	0.0230	5.21	0.67
3.2-NT-Neat	0.049	0.0115	4.26	0.55
8-NT-Neat	0.046	0.0100	4.64	0.60
0.8NW-GO-BM1	0.043	0.00918	4.68	0.60
0.8NW-rGO-BM2	0.047	0.0098	4.83	0.62
3.2NT-GO-BM3	0.042	0.0121	3.47	0.45
3.2NT-rGO-BM4	0.046	0.0117	3.93	0.51
8NT-GO-BM5	0.050	0.0119	4.20	0.54
8NT-rGO-BM6	0.049	0.0103	4.75	0.61
0.8NW-5mg.GO-CD1	0.119	0.0282	4.21	0.54
0.8NW-10mg.GO-CD2	0.115	0.0266	4.31	0.55
0.8NW-5mg.rGO-CD3	0.115	0.0264	4.35	0.56
0.8NW-10mg.rGO-CD4	0.121	0.0240	5.04	0.65

Although identical parameters and procedure was used to prepare the pellets for all the samples, it is seen from Table 5.1 that density varies for all the samples. It is believed from this result that morphology and the type of filler materials and the amount of filler materials (GO/rGO) have impacts on the density of the finally obtained cold-pressed samples. The influence of morphology of the starting bismuth telluride nanomaterials and the amount of GO and rGO filler on the density of the finally obtained cold-pressed samples are discussed in the subsequent sub-sections.

Calculated densities of all the ball-milled samples with different morphology are represented in the bar graph as shown in Fig. 5.1.

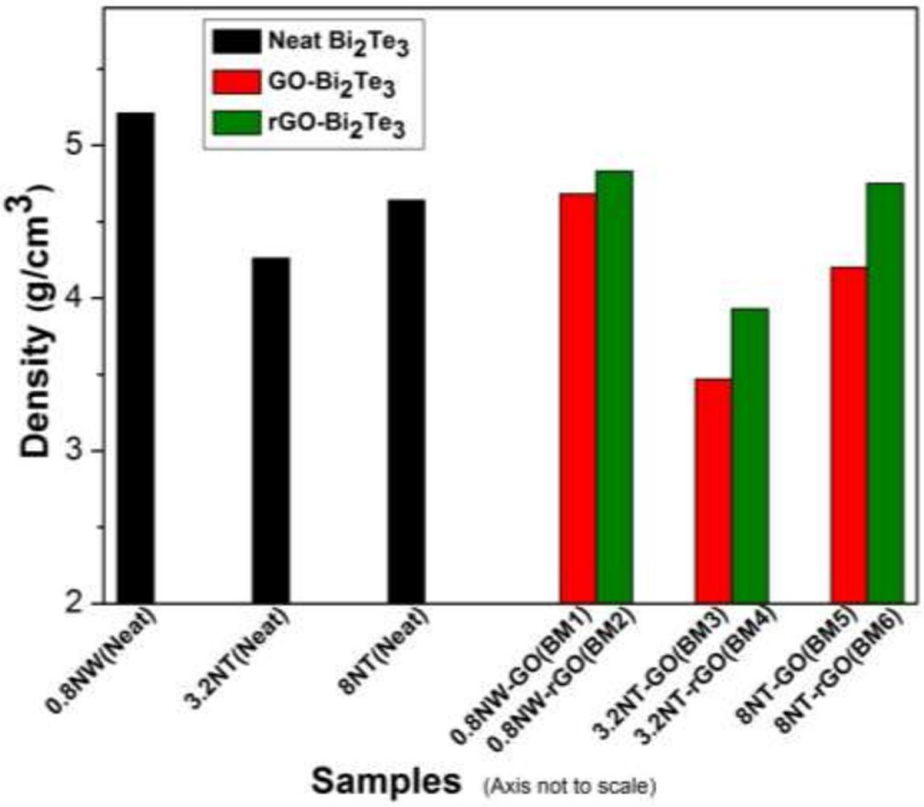

Fig. 5.1 Comparative bar graph for the calculated densities of samples with different morphology of as-synthesized bismuth telluride 1D nanomaterials and ball-milled GO/rGO-bismuth telluride nanomaterials.

The sample consisting of bismuth telluride nanotubes with larger diameter have shown the lowest density as shown in Fig. 5.1. The identical behavior was also seen in all the remainingsamples consisting of nanotubes bismuth telluride either alloyed or doped with GO and rGO samples.It is also found that GO/rGO alloyed with larger diameter bismuth telluride nanotubes sample (3.2NT-GO-BM3 and 3.2NT-GO-BM4) have shown the lowest density. Moreover, it is observed that the TE sample prepared by using nanowire (0.8NW) as filler shows higher density as compared to the identically prepared TE samples. Furthermore, the sample prepared by using larger diameter nanotubes (3.2 NT) as a filler shows a lowes density than the sample which was prepared by using smaller diameter nanotubes (8NT). Thus, the density of the finally cold-pressed TE samplesdepends upon the morphology and size of the starting bismuth telluride 1 D nanomaterials.

Fig. 5.2 represents the bar graph of all the samples consisting of chemically doped GO and rGO-bismuth telluride and the corresponding pallet sample consisting of neat bismuth telluride(nanowires).

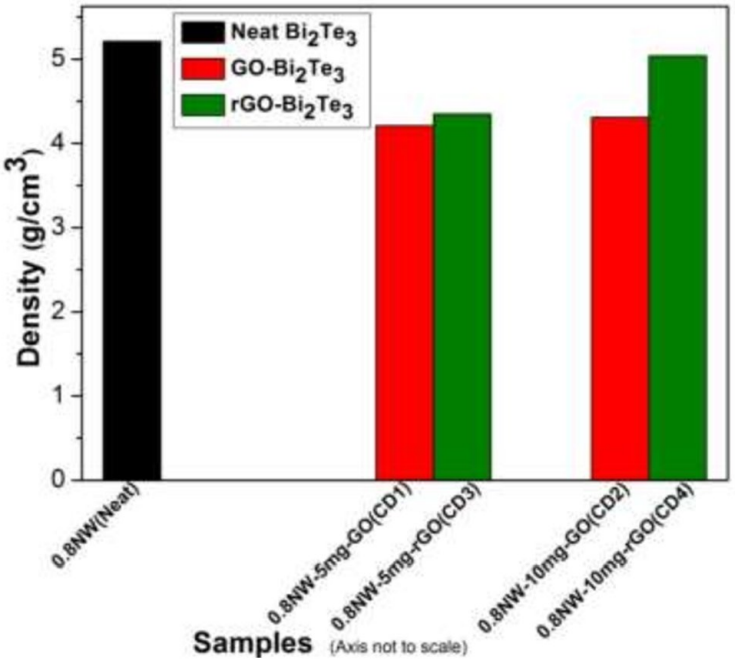

Fig 5.2 Comparative bar-graph for densities of GO/rGO chemically in-situ doped bismuth telluride samples.

As shown in Fig 5.2, calculated density does not vary much as compared to the neat bismuth telluride sample (0.8NW Neat) and there is not much change in the densities with an increase in GO/rGO contents for the in-situ chemically doping process.

5.3 Measurement of Seebeck coefficient

5.3.1 Experimental procedure

The Seebeck coefficient of all the obtained samples is calculated by using the formula,

$$S = \frac{\Delta V}{\Delta T}$$

Where S is the value of Seebeck coefficient, ΔV is the change in potential difference occurred across the sample while the ΔT the temperature difference maintained in the samples. Fig. 5.3 shows the in-home built Seebeck coefficient measurement set up used to measure the Seebeck coefficient of all the samples. The calculated Seebeck coefficient of all the obtained samples is shown in Tables 5.2, 5.3 and 5.4. The voltage drop was measured by using a precision two probes, the temperature probes were placed at the hot end and cold ends of the sample, which

Fig. 5.3 In-home setup built for Seebeck measurement.

was connected to the Agilent 34972A LXI data acquisition system operated by Agilent BenchLink Data logger software.

5.3.2 Seebeck coefficient of all the samples

The calculated Seebeck coefficients of all the obtained samples are shown in tables 5.2, 5.3 and 5.4.The temperature gradient of 5-15^{0}C was employed for calculating Seebeck coefficients of the samples as reported in the earlier work[119]. Three times the sample was measured in a temperature interval of ~ 5-15^{0}C to evaluate the Seebeck coefficientfor all the samples more accurately.

Table 5.2 Measured Seebeck coefficients of bismuth telluride(0.8NW-neat, 3.2NT-Neat and 8NT-Neat) cold pressedpallet samples.

0.8NW-Neat							
Sl No.	**T_1**	**T_2**	**dT (K)**	**V_1 (mV)**	**V_2 (mV)**	**dV (mV)**	**S(µV/K)**
1	55	60	5	-1.55	-1.81	-0.26	-52.0
2	61	70	9	-1.86	-1.36	-0.50	-55.50
3	62	77	15	-1.64	-2.5	-0.86	-57.33
3.2NT-Neat							
Sl No.	**T_1**	**T_2**	**dT (K)**	**V_1 (mV)**	**V_2 (mV)**	**dV (mV)**	**S(µV/K)**
1	37	42	5	-2.54	-2.73	-0.19	-38
2	43	53	10	-1.95	-2.2	-0.25	-25
3	38	54	16	-2.48	-2.99	-0.51	-31.8
8NT-Neat							
Sl No.	**T_1**	**T_2**	**dT (K)**	**V_1 (mV)**	**V_2 (mV)**	**dV (mV)**	**S(µV/K)**
1	43	48	5	-1.6	-1.38	-0.22	-44
2	42	54	12	-2	-1.6	-0.4	-33.3
3	43.65	54	10.35	-2.01	-1.6	-0.41	-39.6

As shown in Table 5.2, 0.8NT-neat sample shows a higher Seebeck coefficientas compared to the 3.2NT-neat and 8NT-neat samples. The 0.8NT-neat sample is highly dense

Table 5.3 Measured Seebeck coefficients of all the mechanically alloyed cold-pressed pallet samples.

0.8NW-GO-BM1							
Sl No.	**T_1**	**T_2**	**dT (K)**	**V_1 (mV)**	**V_2 (mV)**	**dV (mV)**	**S(μV/K)**
1	43	48	5	-1.39	-1.62	-0.23	-46
2	43	53	10	-1.39	-1.83	-0.44	-44
3	52	67	15	-1.80	-2.30	-0.50	-33.3
0.8NW-rGO-BM2							
Sl No.	**T_1**	**T_2**	**dT (K)**	**V_1 (mV)**	**V_2 (mV)**	**dV (mV)**	**S(μV/K)**
1	41	46	5	-0.68	-0.79	-0.11	-22
2	51	60	9	-0.69	-0.88	-0.19	-21.1
3	45	60	15	-0.58	-0.88	-0.30	-20
3.2NT-GO-BM3							
Sl No.	**T_1**	**T_2**	**dT (K)**	**V_1 (mV)**	**V_2 (mV)**	**dV (mV)**	**S(μV/K)**
1	44	54	10	-1.34	-1.81	-0.47	-47
2	41	50	9	-1.67	-2.04	-0.37	-41.1
3	41	50	9	-1.38	-1.8	-0.42	-46.6
3.2NT -rGO-BM4							
Sl No.	**T_1**	**T_2**	**dT (K)**	**V_1 (mV)**	**V_2 (mV)**	**dV (mV)**	**S(μV/K)**
1	41	47	6	-1.5	-1.88	-0.38	-63.3
2	37	47	10	-1.2	-1.87	-0.67	-67
3	36	46	10	-1.15	-1.81	-0.66	-66
8NT-GO-BM5							
Sl No.	**T_1**	**T_2**	**dT (K)**	**V_1 (mV)**	**V_2 (mV)**	**dV (mV)**	**S(μV/K)**
1	38	43	5	-1.78	-1.96	-0.18	-36.0
2	43	56	13	-1.38	-1.70	-0.32	-24.6
3	40	55	15	-1.96	-1.43	-0.53	-35.3
8NT-rGO-BM6							
Sl No.	**T_1**	**T_2**	**dT (K)**	**V_1 (mV)**	**V_2 (mV)**	**dV (mV)**	**S(μV/K)**
1	51	56	5	-1.34	-1.51	-0.17	-34.0
2	56	62	6	-1.51	-1.70	-0.19	-31.6
3	54	73	19	-1.59	-2.29	-0.70	-36.8

compared to the other two samples which result in higher Seebeck coefficient. The possible reason for this may be the denser materials possess higher mean free path and the mobility is higher as compared to the less dense materials.

From table 5.3 it is found that 3.2NT-rGO-BM4 sample shows a higher Seebeck coefficient which was prepared by mechanically alloyed with rGO with the matrix material is large diameter nanotubes of bismuth telluride. It is seen from Table 5.3 that alloying of GO/rGO with different morphologies bismuth telluride nanostructures impacts the Seebeck coefficients. All the samples that are alloyed with GO have shown a lower Seebeck coefficient because GO consists of different hydroxyl and carbonyl functional groups. These functional groups affect the overall charge carriersin the prepared nanostructured materials.

In the case of the samples, those consist of 0.8NW-neat and 8NT neat(smaller diameter) as matrix and rGO as filler, there is no significant improvement in the Seebeck coefficient but in contrast, when 3.2 NT-neat(large diameter nanotubes) were alloyed, it is found that there is a considerable improvement in the Seebeck coefficient. The effect of large tubular hollow morphology and moderate doping of rGO together results in higher Seebeck coefficients. The large diameter nanotubular structure when cold-pressed, it possibly includesimperfections in the material. In addition to this rGO also acts as the phonon-blocking medium. Therefore, when there is a temperature gradient in such material, the phonon-electron interaction may be increased and helping to push electrons to the other end and, in-turn resulting in higher Seebeck coefficients[120].

Table 5.4 shows the Seebeck coefficients of all the GO/rGO in-situ doped bismuth telluride nanostructures based cold-pressed samples. The doping of different amounts of GO/rGO influences the morphology of the final obtained 1D bismuth telluride as discussed in chapter 4.It is found that 0.8NW-10mg-rGO-CD4 pallet sample has shown a higher higher Seebeck coefficient as compared to other samples as shown in Table 5.4. The higher Seebeck coefficient may be due to the cold pressing of the rGO doped chain-linked nanostructures with higher mobilities.

Table 5.4 Measured Seebeck coefficients of all the in-situ doped pallet samples.

0.8NW-5mg-GO-CD1							
Sl No.	**T_1**	**T_2**	**dT (K)**	**V_1 (mV)**	**V_2 (mV)**	**dV (mV)**	**S(μV/K)**
1	51	56	5	-2.72	-2.6	-0.12	-24
2	57	67	10	-2.70	-2.54	-0.16	-16
3	53	68	15	-2.90	-2.54	-0.36	-24
0.8NW-10mg-GO-CD2							
Sl No.	**T_1**	**T_2**	**dT (K)**	**V_1 (mV)**	**V_2 (mV)**	**dV (mV)**	**S(μV/K)**
1	65	70	5	-1.2	-1.3	-0.1	-20
2	60	70	10	-2.62	-2.41	-0.2	-21
3	62	73	11	-2.74	-2.5	-0.24	-21.8
0.8NW-5mg-rGO-CD3							
Sl No.	**T_1**	**T_2**	**dT (K)**	**V_1 (mV)**	**V_2 (mV)**	**dV (mV)**	**S(μV/K)**
1	58	63	5	-1.68	-1.87	-0.19	-38
2	67	73	6	-1.7	-1.5	-0.2	-33.3
3	59	64	5	-1.2	-1.4	-0.2	-40
0.8NW-10mg-rGO-CD4							
Sl No.	**T_1**	**T_2**	**dT (K)**	**V_1 (mV)**	**V_2 (mV)**	**dV (mV)**	**S(μV/K)**
1	61	66	5	-2.6	-2.9	-0.28	-56
2	60	71	11	-2.17	-2.77	-0.60	-54.5
3	60	80	20	-2.17	-3.54	-1.37	-68.5

Table 5.5 shows the average value of Seebeck coefficient with standard deviation for all the cold-pressed samples. It is seen from the table 5.5 all the samples show negative Seebeck

coefficient which means that all the samples are n-type. The majority of charge carriers in all the obtained samples are electrons.

Table 5.5 Calculated Seebeck coefficients of all the obtained samples

Sample ID	Seebeck Coefficient (μV/K)	Standard deviation(μV/K)
0.8NW-Neat Bi_2Te_3	-54.94	2.211
3.2-NT-Neat	-31.6	5.309
8-NT-Neat	-38.9	4.391
0.8NW-GO-BM1	-41.1	5.575
0.8NW-rGO-BM2	-21.03	0.817
3.2NT-GO-BM3	-44.9	2.691
3.2NT-rGO-BM4	**-65.4**	**1.562**
8NT-GO-BM5	-31.96	5.216
8NT-rGO-BM6	-34.13	2.124
0.8NW-5mg-GO-CD1	-21.3	3.771
0.8NW-10mg-GO-CD2	-20.9	0.736
0.8NW-5mg-rGO-CD3	-37.1	2.808
0.8NW-10mg-rGO-CD4	-59.66	6.276

5.3.3 Effect of morphology on the Seebeck coefficient of the cold-pressed samples

The mechanically alloyed 3.2 mL RA bismuth telluride nanotubes with larger diameter alloyed with 3 wt% rGO have shown the highest Seebeck coefficient value. In this nanostructured material, the rGO layers are stacked in between the bismuth telluride nanotubes. The larger contact area of the larger diameter nanotubes with rGO layers has resulted in the high Seebeck coefficient, whereas all the GO based samples have shown lower values due to the presence of more functional groups which decreases the carrier concentrations and also the conductivities of the samples. In chemically doped samples, it is seen that from Fig.5.5 that 10mg rGO doped sample shows a higher Seebeck coefficient due to the chain morphology of the sample. The higher concentration of the rGO sample is higher dense though all the samples were prepared in the identical procedure, possibly it possesses higher carrier mobility due to its higher density.

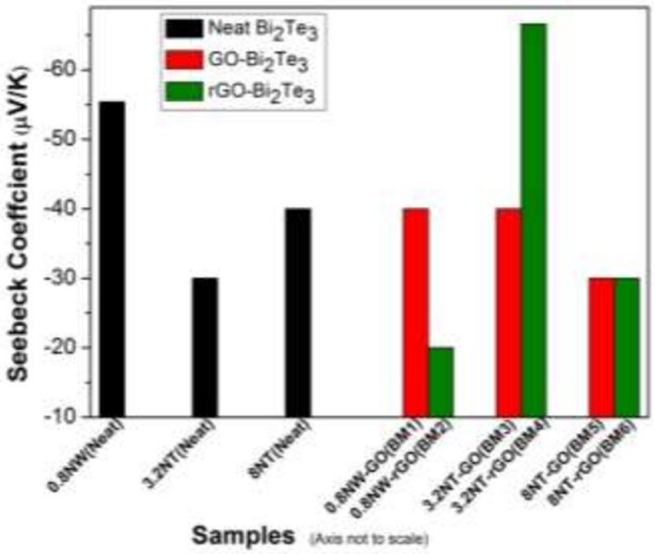

Fig. 5.4Comparative graphical representation of Seebeck coefficients of GO/rGO alloyed bismuth telluride nanomaterials cold-pressed samples with different morphologies

The Seebeck coefficients of all samples with different morphology are depicted in Fig. 5.4. It is seen from Fig. 5.4 that the morphology of the starting bismuth telluride nanomaterials has an impact on the Seebeck coefficient of the obtained samples. For instance, the sample

consisting of neat bismuth telluride nanowires shows higher Seebeck coefficient than the samples that were prepared by using nanotubes(three black bars in Fig. 5.4). Also it has been seen from Fig. 5.4 that for the sample consisting of the larger diameter nanotubes shows lower value of Seebeck coefficient (middle two black bars in Fig. 5.4). However, the trend drastically changes when these samples alloyed with GO or rGO. It is found that there is an increase in the Seebeck coefficient in the 3.2 mL RA bismuth telluride(larger diametre) alloyed with rGO.The improvement in the Seebeck coefficient is possibly due to the increased contact area between the large diameter nanotubes and the rGO sheets and that leads to increase mobility. Whereas alloying of GO sheets with the same larger diameter nanotubes shows a lower Seebeck coefficient due to the presence of functional groups. Thus the carrier mobility reduces and this sample shows a lower Seebeck coefficient.

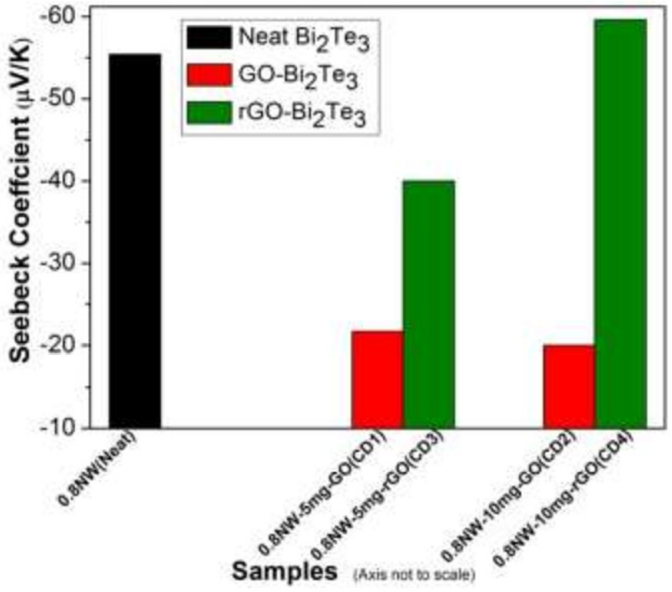

Fig. 5.5 Comparative graphical representation of Seebeck coefficients of GO/rGO in-situ chemically doped bismuth telluride cold-pressed samples.

The effect of the amount of GO and rGO on the Seebeck coefficients of the samples is shown in Fig. 5.5. In this case, only 0.8 mL RA based synthesis procedure was carried out since the corresponding sample has shown higher Seebeck coefficient (as shown in Fig. 5.4). 3.2 mL and 8 mL RA based synthesis procedures were not carried out because of the lower value of

Seebeck coefficients (as shown in Fig. 5.4). It has been seen that GO doped samples do not show any improvement as shown Fig. 5.5. In contrast, rGO doped samples show improvement and increasing the rGO content,there is a significant increase in the thermopower known as Seebeck coefficient. It is also seen that 10 mg rGO doped bismuth telluride based cold-pressed sample has shown the highest Seebeck coefficient among all the samples.

5.4 Measurement of Thermal conductivity

5.4.1 Experimental procedure

The thermal conductivity can be measured in various methods depending upon the heat flow in the samples. When the heat flow is steady and one-dimensional flow then guarded hot plate, the unguarded hotplate isapplicable. In radial heat flow sample, the cylindrical method, spherical method and ellipsoidal methods have been used. When the heat flow is in a non-steady state then hot wire method, transient hot strip method and the transient plane source(TPS) methods are mainly used. In this present work, a transient plane source method has been used by Hot disk TPS 2200 instrument to measure the thermal conductivity, thermal diffusivity and volumetric specific heats of all the obtained cold-pressed samples.

Fig 5.6 Hot Disk TPS 2200 thermal constant analyser[121]

A 10 micron sensor made of nickel double spiral insulated with Teflon/ mica/kapton was used as a heat source and as the time-dependent resistance thermometer. Thermal constants were calculated by measuring the increase in resistance as function of time as given in the following equation

$$R(t)=R_o\{1+\alpha[\Delta T_i+\Delta T_{ave}(\tau)]$$

Where R_o is the resistance of disk at T=0, α is the temperature coefficient of resistivity, ΔT_i is constant temperature difference developed in the insulators. $\Delta T_{ave}(\tau)$ is the increase in temperature of the sample surface measured on the other side of the insulating layers on the nickel sensor.

$$\Delta T_{ave}(\tau)=P_o\, D(\tau)/a.K.\prod^{3/2}$$

Where "a" is the radius of the disk, K is the thermal conductivity and P_o is the total output power coming from the sensor.

5.4.2 Thermal Conductivities of all the samples

The thermal conductivities of all the samples were directly measured from the Hot disk TPS 2200 instrument. Table 5.6 shows the thermal conductivity of all the obtained cold-pressed samples. It is found from Table 5.6 that all the GO/rGO alloyed and GO/rGO dopped cold-pressed samples possess very low thermal conductivity value in the range 0.25-0.32 W/mK.

Table 5.6Thermal conductivity and specific heat (directly measured from Hot disk TPS 2200 instrument) of all the obtained cold-pressed samples.

Sample	Sp. Heat (MJ/m^3K)	Thermal conductivity (W/mK)	Std. deviation
0.8NW-Neat	2.33	0.32	8.63×10^{-5}
3.2NT-Neat	4.38	0.26	5.01×10^{-5}
8NT-Neat	0.66	0.25	6.05×10^{-5}
0.8NW-GO-BM1	3.28	0.30	4.41×10^{-4}
0.8NW-rGO-BM2	3.01	0.29	2.89×10^{-4}
3.2NT-GO-BM3	2.59	0.25	1.43×10^{-4}
3.2NT-rGO-BM4	4.78	0.26	6.35×10^{-5}
8NT-GO-BM5	3.88	0.29	2.97×10^{-4}
8NT-rGO-BM6	3.86	0.30	1.45×10^{-4}
0.8NW-5mg.GO-CD1	1.52	0.32	2.02×10^{-4}
0.8NW-10mg.GO-CD2	1.41	0.25	1.91×10^{-4}
0.8NW-5mg.rGO-CD3	1.14	0.28	5.42×10^{-4}
0.8NW-10mg.rGO-CD4	2.4	0.25	5.21×10^{-5}

5.4.3 Effect of morphology on thermal conductivity of the cold-pressed samples

The thermal conductivity of all the mechanically alloyed samples is depicted in Fig. 5.7 to investigate the morphological(nanowires and nanotubes) effect on the thermal conductivities of the cold-pressed samples.It is found that larger diameter nanotubes based neat(3.2NT-Neat) and mechanically alloyed with GO or rGO samples(3.2NT-GO-BM3 and 3.2NT-rGO-BM4) have shown lower thermal conductivity as compared to nanowires based neat (0.8NW-Neat) and mechanically alloyed with GO and rGO samples(0.8NW-GO-BM1 and 0.8NW-rGO-BM2). It is believed that nanotubes consist of additional scattering surfaces due to hollow in nature as compared to nanowires thus phonon blocking[122] is more effective in nanotubes based samples as a result these samples possess lower thermal conductivity as compared to nanowires based samples.

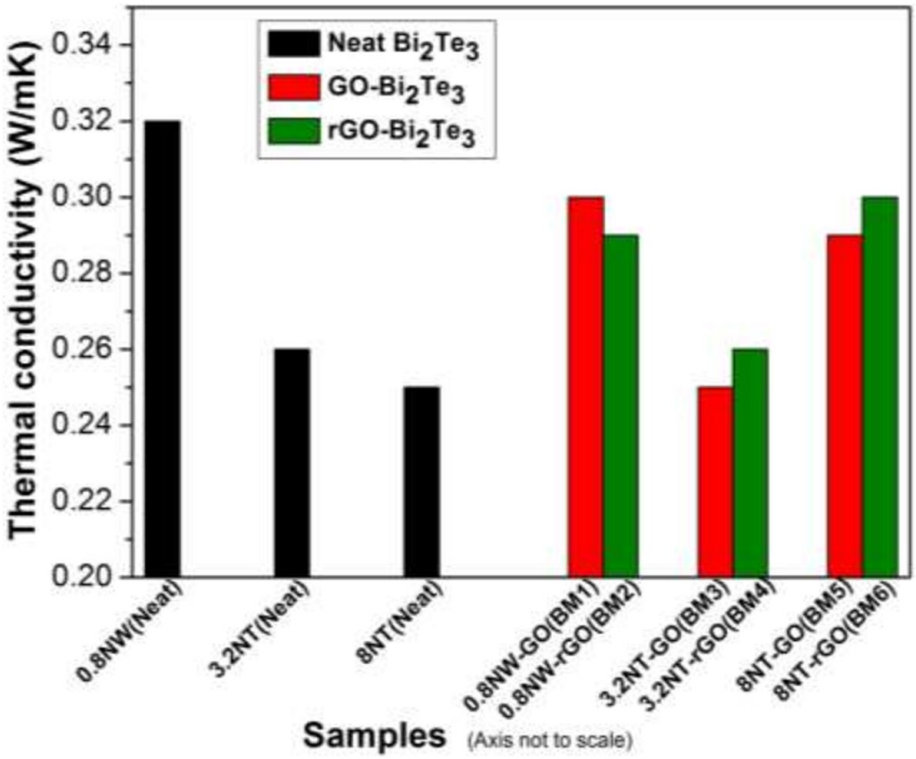

Fig.5.7Graphical representation of thermal conductivity of samples with different morphology of neat bismuth telluride, GO/rGO alloyed bismuth telluride nanomaterials

Moreover, it has also been noticed from Table 5.6 and Fig. 5.7 that addition of GO or rGO does not significantly lower the thermal conductivity more, however little reduction has noticed for the

sample such as 0.8NW-rGO-BM2. This reduction possibly due to the addition of rGO which acts as phonon barriers which reduce the phonon mean free path[122]. However, it has also been found that GO and rGO alloyed with smaller size nanotubes based samples(8NT-GO-BM5 and 8NT-rGO-BM6) show lower thermal conductivity as compared to neat nanotubes based sample(8NT-Neat). This result is possibly obtained due to the increase in the electrical conductivity of the sample.

Therefore, the effect of morphology of the matrix bismuth telluride nanomaterials has shown less impact on the thermal conductivity but alloying with GO/rGO has showna not much significant effect on the TC exceptthe nanowires based samples. GO/rGO act as phonon blocking media resulted in the blocking of the flow of heat flow in the form of phonons. Thus the presence of phonon blocking barriers (GO/rGO) in the samples resulted in the lowering of thermal conductivity. The hollow nanotubes of bismuth telluride with larger diameter alloyed with GO/rGO have shown lower thermal conductivity. However, for a few samples, thermal conductivity increases by adding GO and rGO (8NT-GO-BM5 and 8NT-rGO-BM6), possibly due to an increase in electrical conductivity by addition of GO/rGO. Thus the electronic contribution to thermal conductivity increases and hence thermal conductivity also increases.

5.4.4 Effect of GO/rGO content on the thermal conductivity of the samples

The thermal conductivity of the in-situ chemically 5 mg and 10 mg GO/rGO doped bismuth telluride nanomaterials based cold-pressed samples is shown in Fig. 5.8. Only nanowire-based cold-pressed samples were prepared for investigation since these samples have shown a higher value of the Seebeck coefficient as discussed previous section.It is observed that the thermal conductivity decreases further with increasing the amount of dopping i.e. GO/rGO in thecold-pressed samples(0.8NW-10mg.GO-CD2 and 0.8NW-10mg.rGO-CD4). The doping of rGO in the bismuth telluride nanowires has shown an overall decrease in the thermal conductivity of the samples as shown in Fig. 5.8.

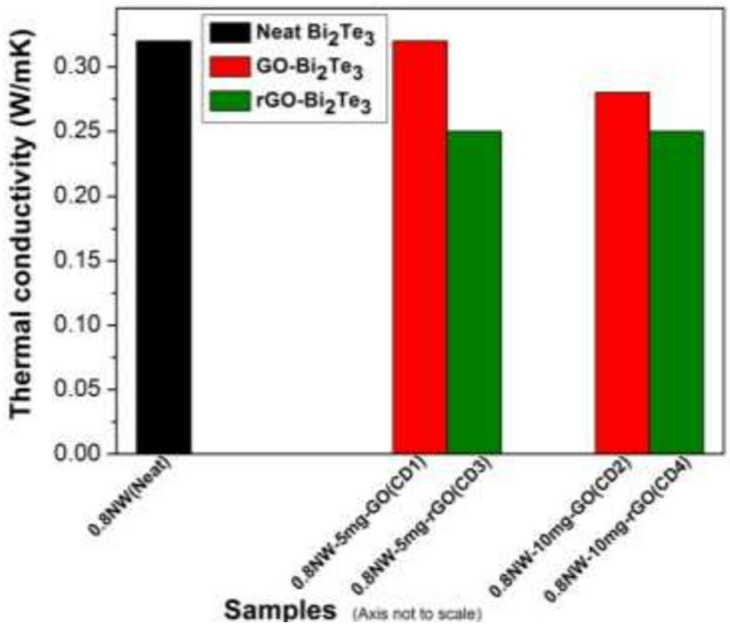

Fig. 5.8 Graphical representation Thermal conductivities of GO/rGO in-situ doped bismuth telluride samples.

The decrease in thermal conductivity in rGO dopped bismuth telluride based cold-pressed sample(0.8NW-10mg.rGO-CD4)is possibly due to the doping of the rGO into individual nanowires. As a result, this process blocks the phonon travel paths from one nanowire to the other as rGO acts as a phonon transfer barrier hence the 10 mg GO/rGO doped bismuth telluride nanostructured materials have shown lowest thermal conductivity.

5.4.5 Measurement of Thermal diffusivity

In practical applications, the temperature gradients or the temperature difference between the hot and cold ends is not constant,in such conditions the thermal diffusivity provides a more accurate analysis of the thermal conduction in all the samples. It gives the rate of heat transfer from the hot side to the cold side in the materials. Thus it provides how fast the material responds to change in temperature. The thermal diffusivity of all the samples was measured by using the same Hot disk TPS 2200 which was used for measuring the thermal conductivity of all the samples and shown in Table. 5.7.

Table 5.7 Thermal diffusivity of all the obtained cold-pressed samples.

Sample	Thermal diffusivity (m^2/S)	Std. deviation
0.8NW-Neat	0.436	1.16×10^{-4}
3.2NT-Neat	0.373	7.08×10^{-5}
8NT-Neat	0.414	9.93×10^{-5}
0.8NW-GO-BM1	0.523	7.59×10^{-4}
0.8NW-rGO-BM2	0.505	7.26×10^{-4}
3.2NT-GO-BM3	0.487	2.73×10^{-4}
3.2NT-rGO-BM4	0.382	9.15×10^{-5}
8NT-GO-BM5	0.464	4.73×10^{-4}
8NT-rGO-BM6	0.744	3.57×10^{-4}
0.8NW-5mg.GO-CD1	0.555	3.55×10^{-4}
0.8NW-10mg.GO-CD2	0.385	3.01×10^{-4}
0.8NW-5mg.rGO-CD3	0.395	7.46×10^{-4}
0.8NW-10mg.rGO-CD4	0.517	1.08×10^{-4}

The thermal diffusivity depends on the density and heat capacity of the samples. It is seen from Table 5.7 that thermal diffusivity varies from the range 0.373-0.744 m^2/S. The samples 8NT-rGO-BM6 and 3.2NT-Neat have shown the highest and lowest thermal diffusivity, respectively.

5.4.6 Effect of Morphology on the thermal diffusivity of the samples

The thermal diffusivity of all the mechanically alloyed with GO/rGO and neat bismuth telluride nanomaterials based cold-pressed samples is depicted in Fig. 5.9. It is seen in Fig. 5.9 that nanowires based sample(0.8NW-Neat) posseses higher thermal diffusivity as compared to nanotubes based samples(3.2NT-Neat and 8NT-Neat). The reason is due to the higher thermal conductivity of 0.8NW-Neat sample (as shown in Table. 5.6), since diffusivity is directly proportional to the thermal conductivity of the materials. However, it is also seen that thermal diffusivity significantly increases when alloyed with rGO in all the samples, which indicating that the addition of rGO helps to improve the heat transfer rate in the samples. Also, these results suggest that when rGO

alloyed with smaller diameter nanotubes based bismuth telluride, it further increases. Therefore by proper size and prope nanofiller, it is possible to tune the heat transfer rate in the TE materials.

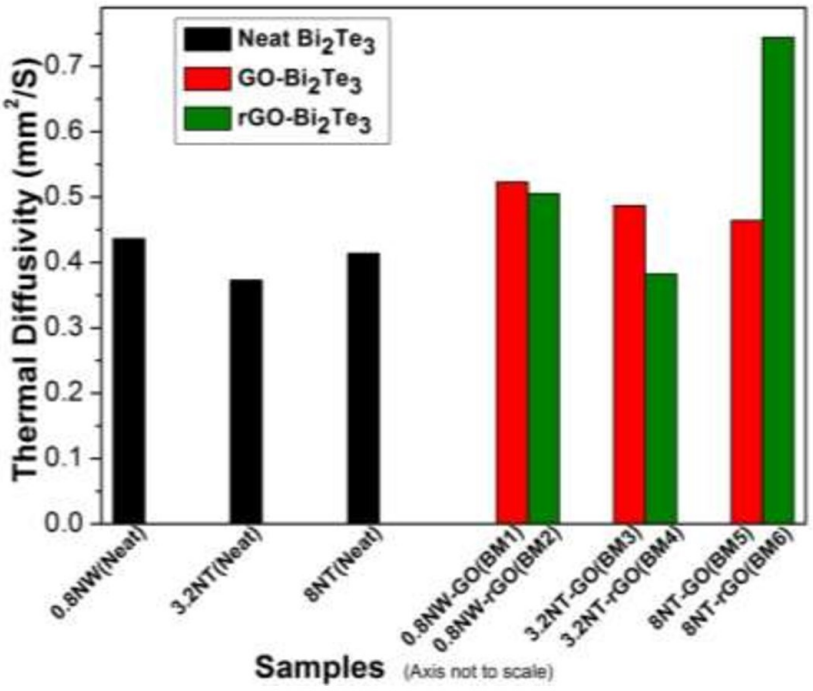

Fig. 5.9 Graphical representation of Thermal diffusivity of all the cold-pressed samples with different morphology (NW, NtTs)of neat bismuth telluride and GO/rGO alloyed bismuth telluride nanomaterials

5.4.7 Effect of GO/rGO content on the thermal diffusivity of the samples

The thermal diffusivity of all the GO/rGO in-situ chemically doped bismuth telluride based cold-pressed samples is shown in Fig. 5.10.

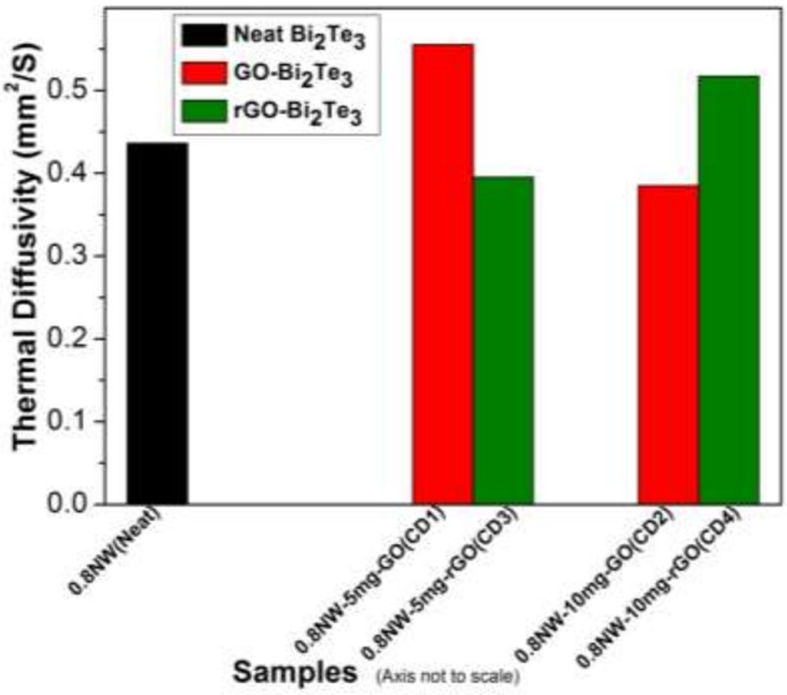

Fig. 5.10Graphical representation of thermal diffusivities of GO/rGO in-situ chemically doped bismuth telluride samples.

From Fig. 5.10 it is observed that the samples such as 0.8NW 5mg-GO and the 0.8NW-10mg-rGO have shown the higher thermal diffusivity. It is clearly seen that 0.8NW 5mg-GO sample shows higher thermal conductivity(as shown in Table. 5.6) as compared to 0.8NW-10mg-rGO, hence it shows the higher thermal diffusivity. In contrast, the sample 0.8NW-10mg-rGO possesses lower thermal conductivity(as shown in Table 5.6) and higher density (as shown in Table 5.1), still it shows higher diffusivity. This obtained result is very interesting since thermal diffusivity is proportional to thermal conductivity and inversely proportional to density. This obtained result is still unknown to us and more research effort is still required to fully understand the heat transfer phenomena in this type of material.

5.5 Measurement of Electrical conductivity

All the obtained cold-pressed GO/RGO- bismuth telluride based mechanically alloyed and in-situ doped TE materials pellet form(6 mm and 10 mm) samples were taken to the probe station for measuring electrical conductivity by varying the applied voltage from -5VD to 5VDC. All the electrical measurements were carried out at room temperature.

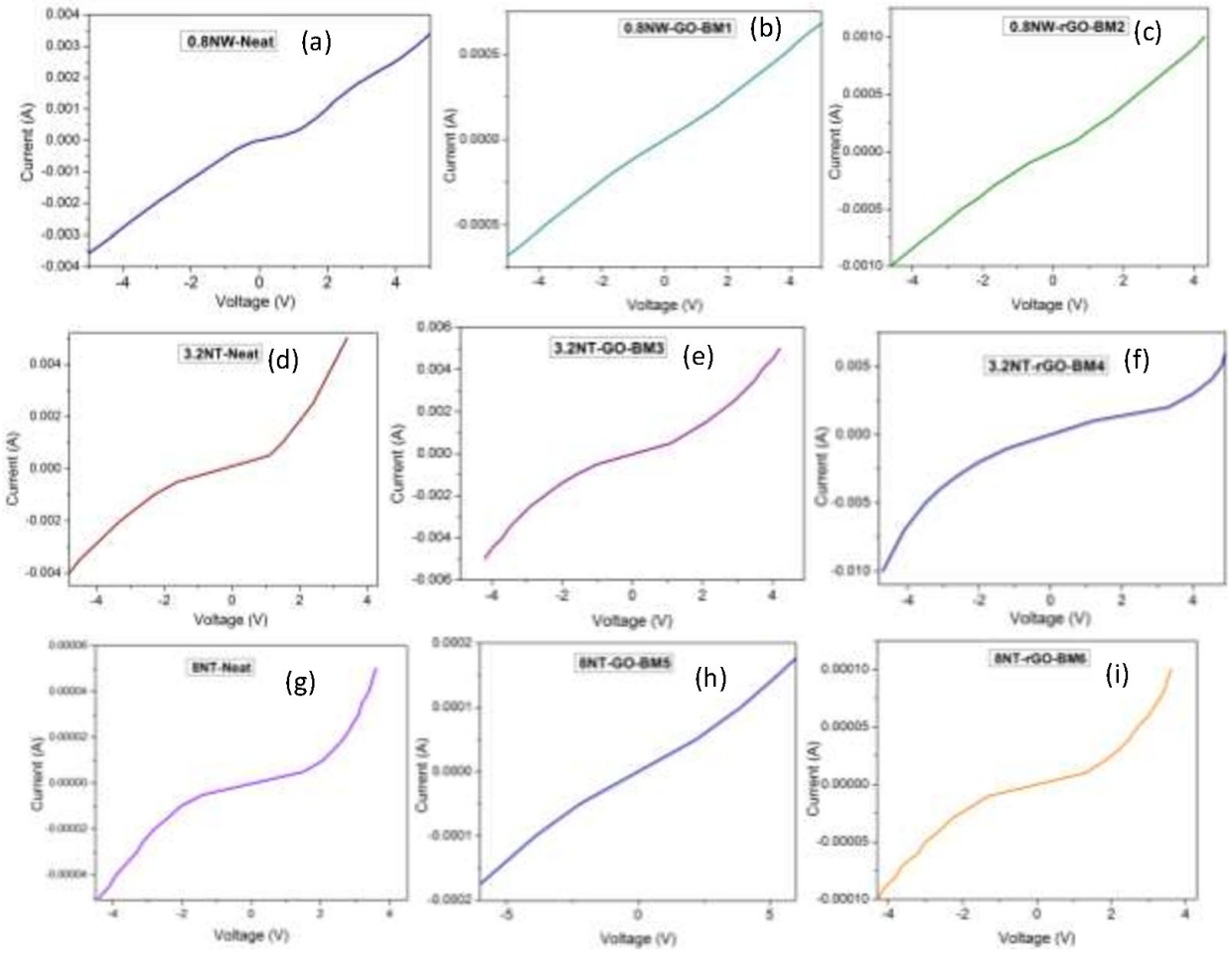

Fig. 5.11 I-V curves of cold-pressed (a-c) 0.8-NW neat Bi_2Te_3 NWs and the corresponding GO/rGO-Bi_2Te_3-nanocomposites, (d-f) 3.2-NT neat Bi_2Te_3 larger diameter nanotubes and the corresponding GO/rGO-Bi_2Te_3- nanocomposites and (g-i) 8-NT neat Bi_2Te_3 smaller diameter nanotubes and the corresponding GO/rGO-Bi_2Te_3-nanocomposites synthesized by the mechanical alloying method.

Fig.5.11(a- i) shows the I-V curves for all cold pressed samples consisting of mechanically alloyed GO or RGO with bismuth telluride and also cold-pressed neat-Bi_2Te_3 nanowires and nanotubes based samples. It is observed from Fig 5.11(a-i) that all the I-V characteristic curves of the samples were not completely rectifying or linear. However, all the I-V curves of the samples are intersecting at zero. These are the most usually observed shape of the curves for semiconducting nanowire materials[123]. As shown inFig 5.11 (b,e,h), I-V curves of samples consisting of GO are little toward linear compared to the rGO alloyed samples (Fig 5.11 (b,e,h)) and the neat GO/rGO unalloyed samples(Fig. 5.11 (a,d,g)).This result indicates that GO-bismuth telluride based cold-pressed sample electrical properties are slightly different than neat-NW/nanotubes or rGO-bismuth telluride based cold-pressed samples, possibly due to the presence of functional groups in such samples. Thus these samples show slightly different electrical phenomena as compared to the neat-NW or nanotubes based and rGO-bismuth telluride based samples.

The electrical conductivity of the samples is calculated from the following formula

$$\rho = 4.53(\frac{v}{i})d$$

Where ρ is the electrical resistivity, V/I is the resistance of the sample and d is the thickness of the pellet. The inverse of electrical resistivity is the electrical conductivity of the sample.This formula is only valid when the sample thickness is very less than the distance between the probes[124];the distance between the probes for all samples was taken at 2 mm gap whereas the sample thickness is always (6 mm/10mm) which is greater than 2 mm.

The slopes of the IV curves (Fig. 5.11(a-i) and Fig. 5.12(a-e)) were calculated for the resistance values and the same were used to calculate the electrical resistivity of the samples as shown in Table 5.8.

Figure 5.12 (a-e) shows the I-V characteristic plots of all the in-situ chemically doped GO/rGO-bismuth telluride(NW) and the 0.8NW-Neat sample. It is seen from Fig. 5.12 (a,b,d,e) the I-V curves represent the behavior of semiconducting nanowires as reported earlier [123]. Therefore the I-V characteristic curves of Fig 5.12 (a,b,d,e) are non-ohmic in behavior. However, 0.8NW-5mg.rGO sample showsa linearity plot (as shown in Fig.5.12(c) with very high resistance; hence it possesses very poor electrical conductivity as shown in table 5.8. The behaviour of this sample can be attributed to their different morphologies due to doping different amount of GO/rGO during the rational synthesis of bismuth telluride.

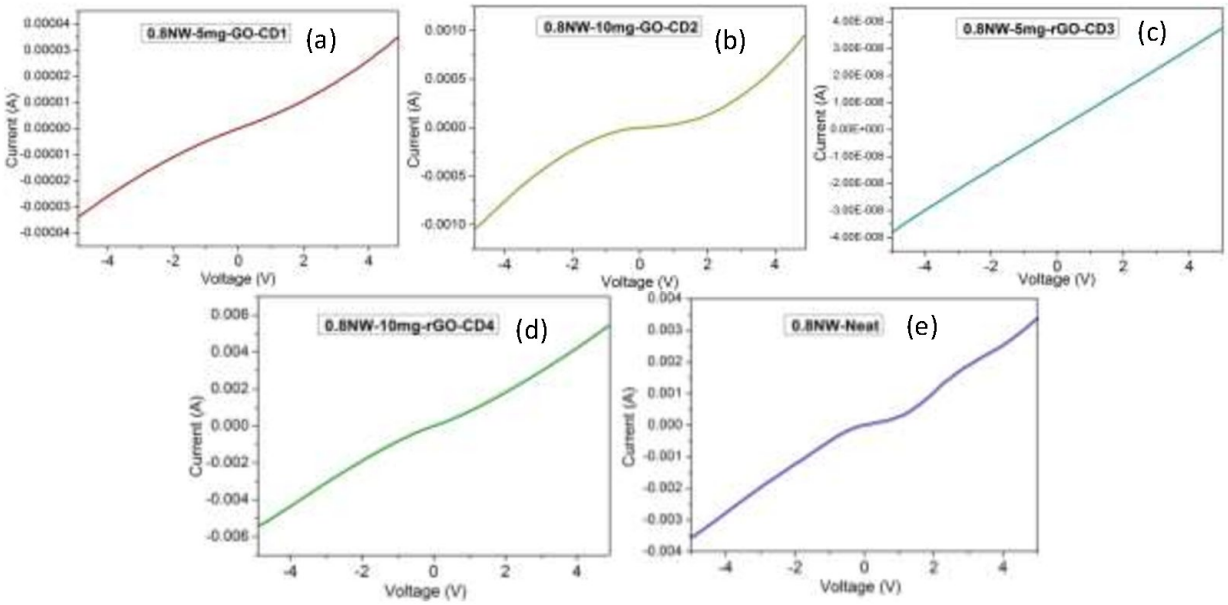

Fig. 5.12 I-V curves of the cold-pressedGO/rGO chemically doped bismuth telluride sample (a)0.8NW-5mg-GO (CD1), (b) 0.8NW-10mg-GO (CD2), (c) 0.8NW-5mg-rGO (CD3), (d) 0.8NW-10mg-rGO (CD4) and (e)0.8 NW neat

Table 5.5 shows the calculated values for the electrical conductivity of all the neat bismuth telluride, mechanically alloyed and chemically dopped cold-pressed samples.

Table. 5.8 Electrical conductivities of pristine GO/rGO, pristine Bi_2Te_3 and Bi_2Te_3-GO/rGO nanocomposites synthesized by Mechanical alloying method

Sample ID	**Electrical Conductivity (S/m) $\times 10^{-3}$**
0.8NW-Neat Bi_2Te_3	403.9
3.2-NT-Neat	204.0
8-NT-Neat	2.14
0.8NW-GO-BM1	78.0
0.8NW-rGO-BM2	96.4
3.2NT-GO-BM3	230.0
3.2NT-rGO-BM4	960.0
8NT-GO-BM5	12.0
8NT-rGO-BM6	4.04
0.8NW-5mg-GO-CD1	2.55
0.8NW-10mg-GO-CD2	48.8
0.8NW-5mg-rGO-CD3	0.0029
0.8NW-10mg-rGO-CD4	775.6

It is found from Table 5.8 that the electrical conductivity of all the samples is in the order of ~ 10^{-3} S/m. The reason for the very low electrical conductivity is due to the cold-pressed sample preparation procedure which has been used in this present work to retain the 1D nanostructure in the of the pallet sample after preparation of the pallet samples. Also due to the very low density of all samples as discussed earlier. The hot-pressed process was not used in the present work because it has been reported that due to hot sintering process, it damages the 1D nanostructure morphology in the bulk hot-pressed sample. Therefore, the objective was to

investigate the thermo-physical properties of the cold-pressed sample such that the main contribution from the 1D nanostructure can be retained after the preparation of the pallet samples.

However, comparing all the samples, it has been seen that addition or dopping of rGO or different morphological starting bismuth telluride based samples show different electrical conductivity. It has been found that rGO-ball milled sample(3.2NT-rGO-BM4) possesses high electrical conductivity. The morphology of the starting bismuth telluride on the electrical conductivity is discussed in the following section.

5.5.2 Effect of morphology on the electrical conductivity of the samples

The graphical representation of neat-bismuth telluride (NW and nanotubes) based cold-pressed samples, GO and rGO mechanically alloyed with NW and nanotubes morphologies bismuth telluride based cold samples is shown in Fig 5.13. It is seen from Fig.5.13 that the morphology of the starting bismuth telluride nanomaterial impacts the electrical conductivity. For instance,neat nanotubular bismuth telluride based sample(3.2-NT-Neat) shows lower electrical conductivity as compared to the nanowires based sample(0.8NW-Neat Bi_2Te_3). Also, it has been seen that the smaller diameter nanotubular based sample(8-NT-Neat) possesses very low electrical conductivity as compared to the larger diameter nanotubes(3.2-NT-Neat) or nanowires(0.8NW-Neat) based sample as shown in Fig. 5.13.

In comparing the effects of the incorporation of GO and rGO by using a mechanically alloyed process, it is found from Fig. 5.13 that the addition of GO does not improve the electrical conductivity but degrades it further. In contrast, the addition of rGO improves the electrical conductivity only for the larger dimeter nanotubes based sample(3.2NT-rGO(BM4)). This is possibly due to the increase in the carrier mobility in the sample because the rGO sheets align in between the larger size nanotubes. However, due to smaller size nanotubes, the sample prepared by using smaller size nanotubes, possibly rGO sheets do not align between the

nanotubes. Whereas, alloying of GO with both nanowires or nanotubes, the electrical conductivity degrades due to the presence of functional groups which affects the carrier mobility.

The experimental results suggest that the morphology of the starting nanomaterials hasa key role in the electrical conductivity of the mechanically alloyed samples. It is also possible to improve further the electrical conductivity by optimizing the sintering process parameters or by applying a different sample preparation approach, which is the future scope of the present work.

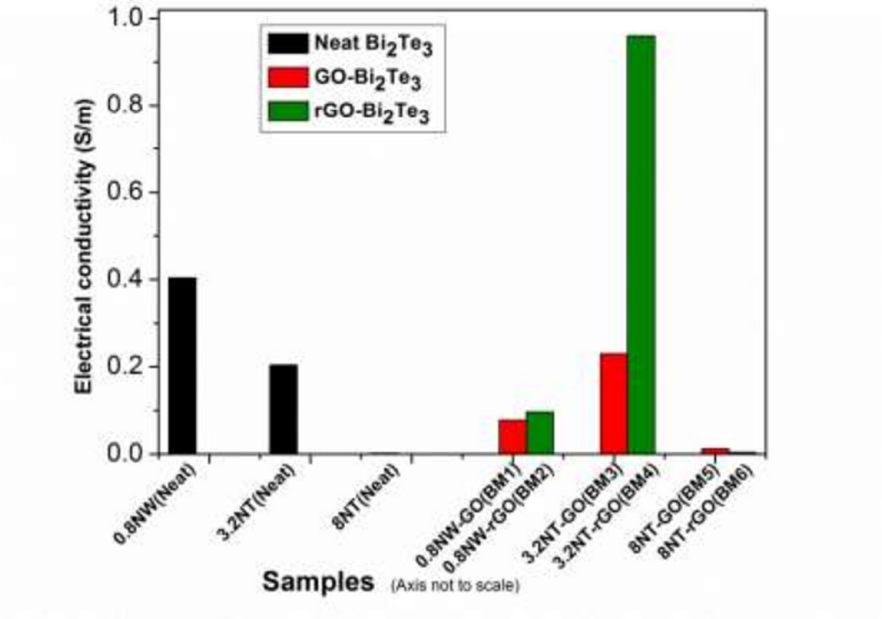

Fig. 5.13Graphical representation of the electrical conductivity of the cold-pressed samples with different morphology of neat bismuth telluride, GO/rGO alloyed with bismuth telluride(NW and nanotubes) cold-pressed samples.

5.5.3 Effect of GO/rGO content on the electrical conductivity

All the chemically doped with GO and rGO based cold-pressed samples are graphically shown in Fig.5.14. It is shown from Fig. 514 that 10 mg rGO doped bismuth telluride nanowire

sample(0.8NW-10mg-rGO-CD4) shows higher electrical conductivity, possibly due to the chain morphology of the sample as shown in Fig. 4.7. Also, ahigher concentration(10 mg) of rGO sample has shown higher density as compared to other chemically doped samples which possiblypossesses higher carrier mobility.

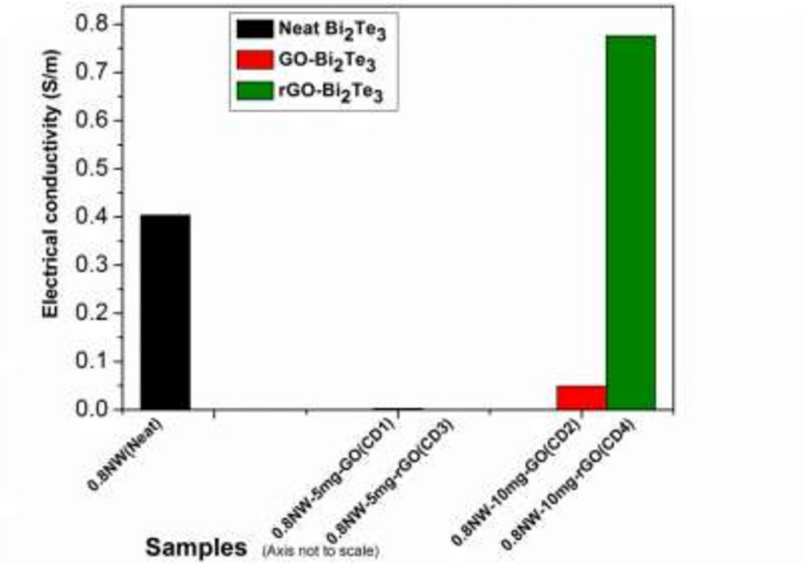

Fig. 5.14Graphical representation of the electrical conductivity of the cold-pressed samples with different amounts of GO and rGO in-situ chemically doped.

Thus, the morphology of the source nanomaterial and addition of rGO are the keys influencing parameters for improving the thermophysical parameters of the samples. Also, the preparation of the process of the bulk nanostructured materials plays a crucial role in attaining higher electrical conductivities and Seebeck coefficient as well as high ZT.

5.6 Results and discussion

The figure of merit(ZT) which is an important parameter(energy conversion efficiency) for the thermoelectric materials and strongly depends on the materials parameters such as the Seebeck coefficient(S), electrical conductivity(σ) and the thermal conductivity(k), is calculated for all the samples by using the following formula[125]

$$ZT = \frac{S^2 \sigma T}{k}$$

Where S is the Seebeck coefficient, σ is the electrical conductivity, k is the thermal conductivity and T is the operational temperature (room temperature 298K). Thecalculated thermo-electric figure of merit(ZT) of all the samples is shown in Table 5.9.

Table 5.9 Calculated figure of merit(ZT) of all the cold-pressed nanostructured neat bismuth telluride sample and GO/rGO mechanically alloyed and chemically-in-situ doped based bismuth telluride samples (at room temperature)

Sample ID (Cold pressed pellets)	**Seebeck Coefficient (μV/K)**	**Electrical Conductivity (S/m) × 10^{-3}**	**Thermal Conductivity (W/m-K)**	**Figure of merit(×10^{-6})**
0.8NW-Neat Bi_2Te_3	-54.94	403.9	0.32	1.13
3.2-NT-Neat	-31.6	204.0	0.26	0.23
8-NT-Neat	-38.9	2.14	0.25	0.003
0.8NW-GO-BM1	-41.1	78.0	0.30	0.13
0.8NW-rGO-BM2	-21.03	96.4	0.29	0.04
3.2NT-GO-BM3	-44.9	230.0	0.25	0.5
3.2NT-rGO-BM4	**-65.4**	**960.0**	**0.26**	**4.70**
8NT-GO-BM5	-31.96	12.0	0.29	0.01
8NT-rGO-BM6	-34.13	4.04	0.30	0.004
0.8NW-5mg-GO-CD1	-21.3	2.55	0.32	0.001
0.8NW-10mg-GO-CD2	-20.9	48.8	0.25	0.02
0.8NW-5mg-rGO-CD3	-37.1	0.0029	0.28	0.000004
0.8NW-10mg-rGO-CD4	**-59.66**	**775.6**	**0.25**	**3.29**

As shown in Table 5.9, it is found that the 3.2NT-rGO-BM4 has shown the highest figure of merit with a higher value of Seebeck coefficient, lower value of thermal conductivity and higher value of electrical conductivity among all the other obtained samples. These results indicate that rGO layers act as phonon blocking barriers due to the interface between the rGO and bismuth telluride nanotubes(larger diameter) without harming the electrical conductivities as compared to other samples. 10mg.rGO-CD4 sample has also shown a higher figure of merit value. However, all the cold-pressed nanostructured thermo-electric materials have shown a very low figure of merit(ZT) as compared to the required ZT value (~2-3) for utilizingin the commercial applications. The main reason is that all thesamples have shown poor electrical conductivity. However, compared to the other obtained sample, 3.2NT-rGO-BM4 shows higher electrical conductivity. These findings suggest that the ball milling process is the optimum process in the present work and incorporation of rGO as a filler material improves the figure of merit. Moreover, these findings also suggest that all the obtained samples show lower thermal conductivity due to the inclusion of GO or rGO, possibly due to the strong phonon scattering at the interface and also due to the holey nanostructure with porosity as evidenced from the FESEM images of the broken pallet samples (as shown in Fig. 5.15 and 5.16).

It has been already known that the porosity, crystallinity, density, grain size of the fabricated nanostructured material directly influence its material properties[89]. Therefore to investigate the morphology of the incorporated bismuth telluride nanomaterials(nanowires/nanotubes) in the cold-pressed samples (3.2NT-rGO-BM4 and 0.8NW-10mg-rGO-CD4), both the sampleswere broken and FESEM images were captured. The cross-section and top view FESEM images of the broken pellet samples are shown in Fig. 5.15(a-d) and Fig. 5.16(a-d) for the 3.2NT-rGO-BM4 and 0.8NW-10mg-rGO-CD4 samples, respectively.

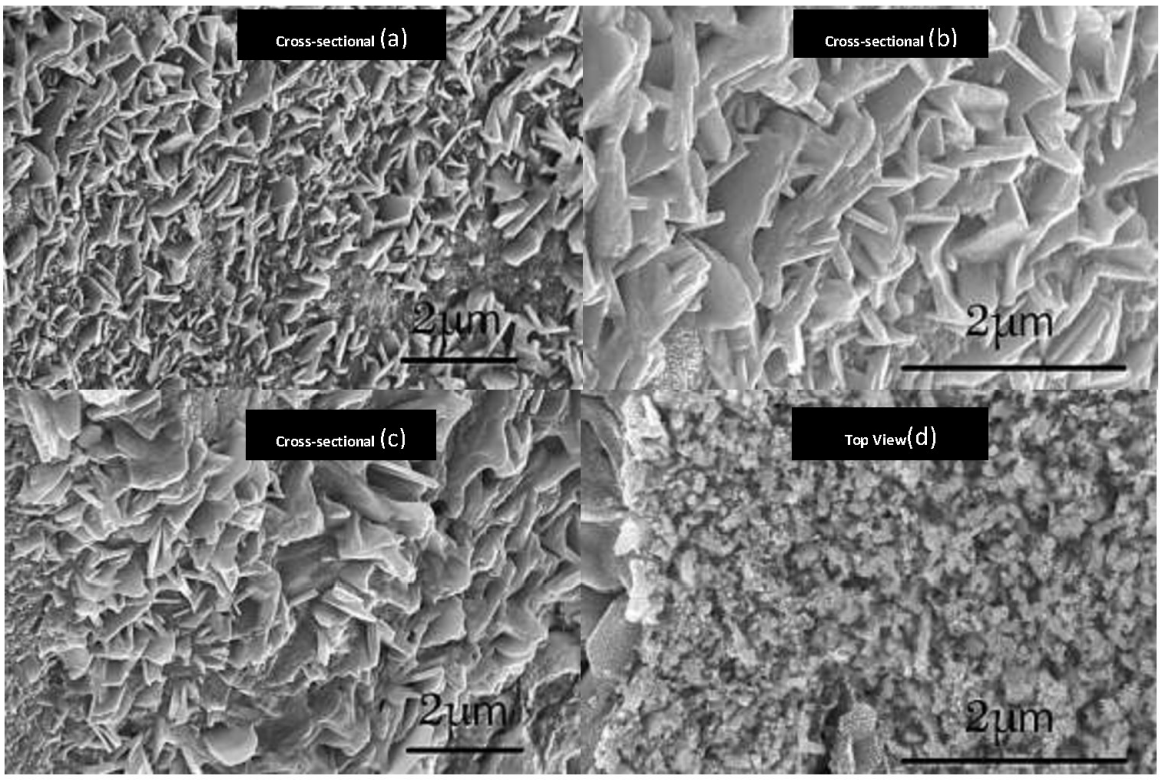

Fig.5.15(a-c) Cross-sectionaland (d) top view FESEM images of the broken 3.2NT-rGO-BM4 cold-pressed pellet sample

As shown in Fig. 5.15(a-c), most of the bismuth telluride larger size nanotubes retain the morphology (nanotubes) after the cold-pressed process. However, it shows porosity in the sample. Thus FESEM images evidence that the nanotubes are closely packed layer by layer in the sample, butit possesses high porosity. As a result, it shows the lower thermal conductivity but due to porous in nature, the electrical conductivity does not improve.

FESEM images (cross-sectional and top view) of the broken pallet sample of *0.8NW-10mg.rGO CD4*are shown in Fig. 5.16(a-d). This result indicates that most of the nanowires retained their morphology after the cold-pressed process, as shown in Fig. 5.16(a-c).

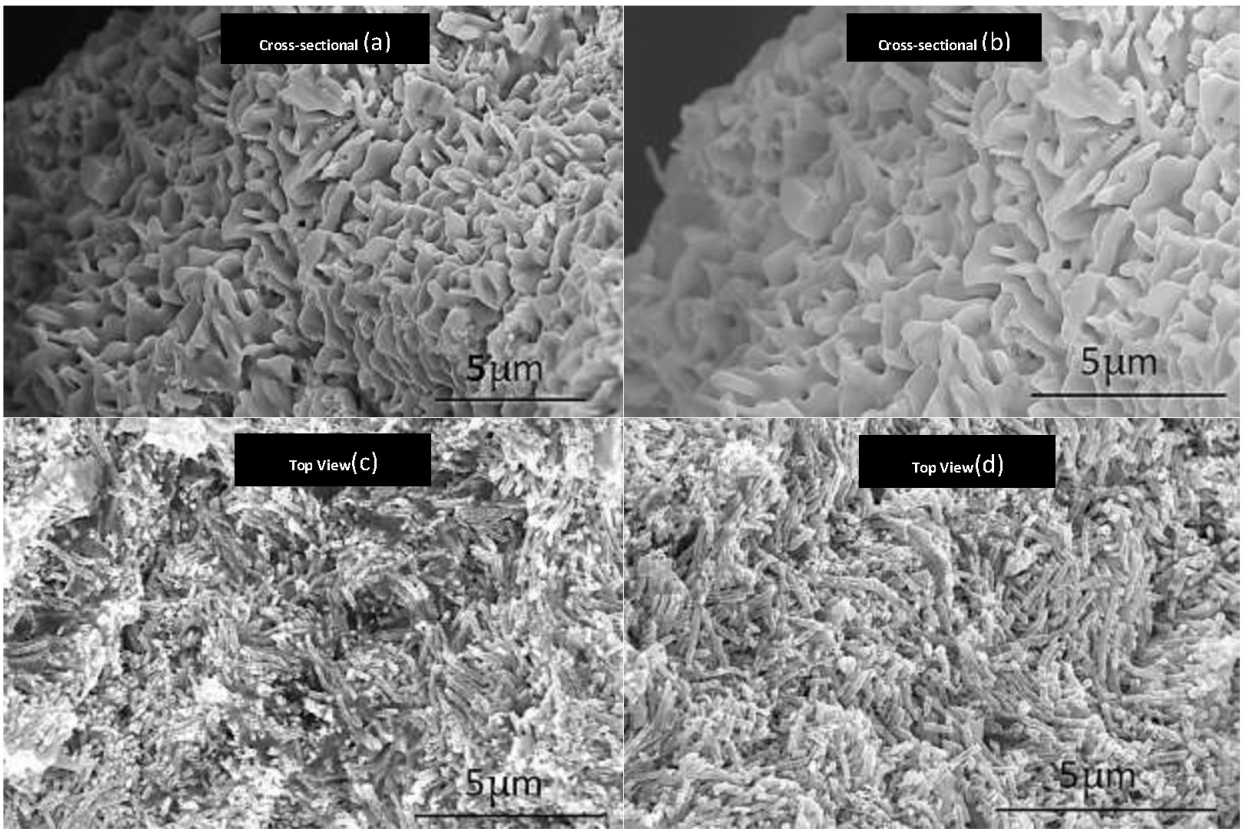

Fig. 5.16(a-b)Cross-sectional and (c-d)top view FESEM images of the broken 0.8NW-10mg.rGO CD4 cold-pressed pallet sample.

Also, this results evidence that very little damage to the morphology of bismuth telluride nanomaterials(nanowires) (as shown in Fig. 5.6(c-d))as compared to the ball-milling process(as shown in Fig. 5.14(d)). It isalso found from the cross-sectional FESEM images(Fig. 5.16(a-c)) that the nanowires are closely packed layer by layer with higher porosity. The presence of porosity possibly reduces the movement of charge carriers in the cold-pressed sample, and hence,the electrical conductivity is very poor. In contrast, the porosity likely helps to reduce the thermal conductivity and therefore, all the cold-pressed samples possess very low value.

It is possible to improve the electrical conductivity by using different sample preparation process or using a binder to reduce the porosity in the sample. More investigation is still required by using a binder or another sample preparation process to improve the electrical conductivity so that higher ZT can be achieved. This work is the future scope of this thesis work.

5.7 Conclusion

All the synthesized processes to obtain the neat and GO/rGO incorporated bismuth telluride nanomaterials have been discussed in previous chapters. This chapter presents thestudy of the thermophysical properties like density, thermal conductivity, Seebeck coefficient and electrical conductivity of these cold-pressed samples. Experimental results indicate that all the cold-pressed samples possess very low density as compared to the standard value due to porous in nature. However, the experimental results also suggest that the morphology(nanowires and nanotubes) of the starting materials impacts the density of the samples due to the different stacking arrangement(from the FESEM images of broken pallet samples) after the cold-pressed process.

The experimental results suggest that the starting bismuth telluride nanomaterials morphology(nanowires/nanotubes) impacts the thermophysical properties; therefore it is possible to achieve higher ZT by properly tuning the morphology of the starting source nanomaterials. Also, it indicates that the larger diameter bismuth telluride mechanically alloyed with rGO based cold-pressed TE material shows improvement in the thermo-physical properties and ZT. Moreover, experimental results also evidence that the addition of a higher concentration of rGO improves the thermo-physical properties and ZT in both the mechanically alloy and in-situ chemical dopping processes. However, the electrical conductivity of all the cold-pressed samples is very poor due to the porosity in the samples. It can be improved by using a suitable sample preparation process or addition of binder, so that morphology of the nanomaterials can be retained with minimizing the porosity. Thus a higher ZT value can be achieved.

Chapter 6

Summary, Conclusion and future scope

- In the present work, different bismuth telluride 1D nanomaterials such as nanowires, larger and smaller size nanotubes were successfully synthesized by using a wet chemical rational design method by varying the amount of reducing agent. Graphene oxide(GO)was synthesized by using the modified Hummers method and reducedgraphene oxide(rGO) was successfully obtained by thermal and chemical reduction. Different characterization methods were carried out to analyze the structure, composition, morphology of all the as-obtained 1D bismuth telluride, GO and rGO samples. For instance, XRD, RAMAN and TEM analysis results evidenced the formation of GO and rGO. FESEM and TEM results indicated that three different morphologies of the bismuth telluride(Bi_2Te_3)nanostructures such as nanowires, larger diameter nanotubes, and smaller diameter nanotubes were successfully obtained by varying the amount of the reducing agent during the rational design approach. The XRD patterns of all the three samples have indicated that all the crystal planes are in good agreement with the standard diffraction planes of bismuth telluride.Elemental analysis of these three different morphological bismuth telluride nanomaterials i.e., 0.8NW, 3.2NT and 8NT have shown Bi and Te contents; however 0.8NW sample is Te-rich, 3.2NT sample is Bi-rich and 8NT sample is close to stoichiometry. EDS-TEM results indicate that the reducing agent plays a key role inthe synthesized stoichiometry ofBi_2T_3 sample. Furthermore, FTIR analysis results indicated the formation of bismuth telluride nanomaterials and Raman analysis result have shown the molecular vibration of different bands which are missing in the bulk bismuth telluride samples indicating the formation of 1D nanomaterials.

- In the second part of this thesis work, three different morphologiesof bismuth telluride (Bi_2Te_3)nanostructures such as nanowires, larger diameter nanotubes, and smaller diameter nanotubes were employed to fabricate a set of GO/rGO-Bi_2Te_3 nanostructured

materials by the mechanical alloying process. All the synthesized GO/rGO-Bi_2Te_3 nanocomposite materials were characterized by XRD, EDS, FESEM, FTIR and Raman spectroscopy for structural, compositional, morphology and molecular structure analysis. The FESEM and TEM results indicated that the high energetic ball milling process breaks the larger diameter nanotubular structures during the process and possibly help to establish a strong contact between the nanofiller and matrix material as compared to the smaller diameter nanotubes. However, the nanowire or smaller diameter nanotubular structures are mostly decorated on the surface of the reduced graphene oxide that leads to no-perfect contact between the filler and matrix material. The RAMAN spectra shown characteristics peaks of the GO and rGO, the D peak appears at 1366 cm^{-1} and the G peak at about 1600 cm^{-1} in all the samples. This results clearly evidence the formation of the GO/rGO-Bi_2Te_3 nanocomposites and further have shown very good agreement with the FT IR analysis results

- In the next part of this work, GO and rGO doped bismuth telluride nanostructures were synthesized by using the in-situ chemical rational approach.For this purpose, two different amount of GO and rGO such as 5 mg and 10 mg were used as dopants to investigate the impacts of chemical doping process on the structure, morphology and composition of the GO and rGO doped bismuth telluride nanostructures.Different morphologies 1D TE nanomaterials such as nano-screws, nanoplates/nanowires, and rough surface thick wall nanotubes are obtained by controlling the concentration of the dopants(GO/rGO). XRD and Raman analysis results clearlyindicated that for few samples, GOs are mostly reduced to rGO during the in-situ doping synthesis process. RAMAN spectra of obtained GO/rGO-doped bismuth telluride show the corresponding peaks of GO/rGO at 1300 cm^{-1} to 1650 cm^{-1} which confirms the formation of GO and rGO doped bismuth telluride nanostructures. HRTEM analysis also shows the embedment of GO/rGO in the matrix bismuth telluride nanostructures.FT IR analysis results further evidence the formation of GO/rGO-bismuth telluride nanomaterials.

- Final part of this work presents the investigation of the thermo-physical properties such as density, Seebeck coefficient, thermal conductivity and electrical conductivity of all 0.8NW neat, 3.2NT neat, 8NT neat, GO/rGO based bismuth telluride nanomaterials prepared by mechanical alloying and in-situ doping process to ensure the best synthesis process to obtain high figure of merit(ZT) and also to study the impacts of different morphological source bismuth-telluride 1D nanomaterials on the thermo-physical properties. For this purpose, all the obtained samples in the powder form were cold-pressed into disk-shaped pellets. 0.8NW-10mg-rGO-CD4 sample has shown higher density, higher electrical conductivities and higher Seebeck coefficient.3.2 mL RA bismuth telluride mechanically alloyed with rGO have shown higher Seebeck coefficient value due to the improvement in the contact area between the large diameter nanotubes and the rGO sheets. These samples show lower thermal conductivity due to the presence of phonon blocking barriers(GO/rGO) or inclusion of GO or rGO. The figure of merit(ZT) for all the cold-pressed nanostructured samples was estimated and it is found that two samples such as 3.2NT-rGO-BM4 and 0.8NW-10mg-rGO-CD4 have shown the higher figure of merit(ZT) value as compared to the remaining samples.
- These experimental findings suggested that the inclusion of the higher amount of rGO either by ball-milling or in-situ chemically doping process improves the figure of merit(ZT). Further, these experimental results suggest that the morphology(nanowires, smaller or larger nanotubes) of the starting nanomaterials play a crucial role for improvement in the thermophysical properties of the TE
- The present work opens apathway to carry out further work in this area to achieve an efficient TE material for future energy harvesting applications.

Future Scope of the present thesis work

The future scope of this thesis work is outlined as follows

- More study on the influence of the higher amount of rGO consisting of mono or bilayer graphene is still required to find the influence of higher concentration on the thermos-physical properties.

- Different sample preparation approaches needto be investigated without destroying the incorporated nanostructures to improve the density and also to minimize the porosity so that electrical property can be improved.
- Also, new additive elements with smaller size particles (1-10nm) can be utilized that can improve the carrier concentration and hence the electrical properties can be improved. Ultimately, higher ZT can be achieved.
- Detailed electrical characterizations such that Hall-effect measurement needs to be carried out to investigate the mobility and charger carrier concentration that help to pave a pathway for improving the preparation process for improving the electrical properties.

Chapter 7

References

[1] S. Leblanc, "Thermoelectric generators : Linking material properties and systems engineering for waste heat recovery applications," *Sustain. Mater. Technol.*, vol. 1–2, pp. 26–35, 2014.

[2] B. Orr, A. Akbarzadeh, M. Mochizuki, and R. Singh, "A review of car waste heat recovery systems utilising thermoelectric generators and heat pipes," *Appl. Therm. Eng.*, vol. 101, pp. 490–495, 2016.

[3] M. F. Remeli, L. Kiatbodin, B. Singh, K. Verojporn, and A. Date, "Power generation from waste heat using Heat Pipe and Thermoelectric Generator," *Energy Procedia*, vol. 75, pp. 645–650, 2015.

[4] F. J. Disalvo, "Thermoelectric Cooling and Power Generation," *Energy*, vol. 285, no. JULY, pp. 703–707, 1999.

[5] O. Caballero-calero and M. Martín-gonzález, "Thermoelectric nanowires : A brief prospective," *Scr. Mater.*, vol. 111, pp. 54–57, 2016.

[6] L. E. Bell, "Cooling, Heating, Generating Power, and Recovering Waste Heat with Thermoelectric Systems," *Science (80-.).*, vol. 321, no. 5895, pp. 1457–1462, 2008.

[7] H. Zhang and D. V Talapin, "Thermoelectric Tin Selenide : The Beauty of Simplicity **," *Angew. Chemie - Int. Ed.*, vol. 53, pp. 9126–9127, 2014.

[8] H. B. and L. L. Yunqiang Chen, Kaiwu Chen, "Electrochemically reduced graphene porous material as light absorber for light-driven thermoelectric generator," *J. Mater. Chem.*, vol. 22, pp. 17800–17804, 2012.

[9] G. J. Snyder and E. S. Toberer, "Complex thermoelectric materials," *Nat. Mater.*, vol. 7, no. February, pp. 105–114, 2008.

[10] Y. Gelbstein, "Thermoelectric power and structural properties in two-phase Sn/SnTe alloys," *J. Appl. Phys.*, vol. 105, no. 2, pp. 10–15, 2009.

[11] V. P. Vedeneev, S. P. Krivoruchko, and E. P. Sabo, "Tin telluride based thermoelectrical alloys," *Semiconductors*, vol. 32, no. 3, pp. 241–244, 1998.

[12] O. Appel, T. Zilber, S. Kalabukhov, O. Beeri, and Y. Gelbstein, "Morphological effects on the thermoelectric properties of $Ti_{0.3}Zr_{0.35}Hf_{0.35}Ni_{1+\delta}Sn$ alloys following phase separation," *J. Mater. Chem. C*, vol. 3, no. 44, pp. 11653–11659, 2015.

[13] J. Shuai, J. Mao, S. Song, Q. Zhang, G. Chen, and Z. Ren, "Recent progress and future

challenges on thermoelectric Zintl materials," *Mater. Today Phys.*, vol. 1, pp. 74–95, 2017.

[14] G. Rogl *et al.*, "In-doped multifilled n-type skutterudites with ZT = 1.8," *Acta Mater.*, vol. 95, pp. 201–211, 2015.

[15] H. Zhao *et al.*, "High thermoelectric performance of MgAgSb-based materials," *Nano Energy*, vol. 7, pp. 97–103, 2014.

[16] Y. Gelbstein, Z. Dashevsky, and M. P. Dariel, "Highly efficient bismuth telluride doped p-type Pb0.13Ge 0.87Te for thermoelectric applications," *Phys. Status Solidi - Rapid Res. Lett.*, vol. 1, no. 6, pp. 232–234, 2007.

[17] Y. Gong *et al.*, "Extremely low thermal conductivity and enhanced thermoelectric performance of polycrystalline SnSe by Cu doping," *Scr. Mater.*, vol. 147, pp. 74–78, 2018.

[18] D. Park, H. Ju, and J. Kim, "Preparation and thermoelectric properties of two types of nanostructured tellurium with multi-walled carbon nanotubes," *J. Alloys Compd.*, vol. 748, pp. 305–313, 2018.

[19] C. Meng, C. Liu, and S. Fan, "A promising approach to enhanced thermoelectric properties using carbon nanotube networks," *Adv. Mater.*, vol. 22, no. 4, pp. 535–539, 2010.

[20] S. D. Kang *et al.*, "Enhanced stability and thermoelectric figure-of-merit in copper selenide by lithium doping," *Mater. Today Phys.*, vol. 1, pp. 7–13, 2017.

[21] N. P. Gorbachuk, A. S. Bolgar, V. R. Sidorko, and L. V Goncharuk, "HEAT CAPACITY AND ENTHALPY OF Bi 2 Si 3 AND Bi2Te3 IN THE TEMPERATURE RANGE 58-1012 K," *Powder Metall. Met. Ceram.*, vol. 43, pp. 284–290, 2004.

[22] C. Hwang, "Effects of excess Te on the thermoelectric properties of p -type 25 % Bi 2 Te 3 -75 % Sb 2 Te 3 single crystal and hot-pressed sinter," *Scr. Mater.*, vol. 6, pp. 3291–3297, 2001.

[23] S. Jung *et al.*, "Impurity-free , mechanical doping for the reproducible fabrication of the reliable n -type Bi 2 Te 3 -based thermoelectric alloys," *Acta Mater.*, vol. 150, pp. 153–160, 2018.

[24] H. S. Dow *et al.*, "Effect of Ag or Sb addition on the thermoelectric properties of PbTe," *J. Appl. Phys.*, vol. 108, no. 11, 2010.

[25] R. He *et al.*, "Improved thermoelectric performance of n-type half-Heusler MCo 1-x Ni x Sb (M = Hf, Zr)," *Mater. Today Phys.*, vol. 1, pp. 24–30, 2017.

[26] L. P. Hu *et al.*, "Enhanced figure of merit in antimony telluride thermoelectric materials

by In-Ag co-alloying for mid-temperature power generation," *Acta Mater.*, vol. 85, pp. 270–278, 2015.

[27] K. Romanjek, S. Vesin, L. Aixala, T. Baffie, and J. Dufourcq, "High-Performance Silicon – Germanium-Based Thermoelectric Modules for Gas Exhaust Energy Scavenging," *Electron. Mater.*, vol. 44, no. 6, pp. 2192–2202, 2015.

[28] M. Hamid *et al.*, "A review on thermoelectric renewable energy : Principle parameters that affect their performance," *Renew. Sustain. Energy Rev.*, vol. 30, pp. 337–355, 2014.

[29] P. K. Rawat and B. Paul, "Simple design for Seebeck measurement of bulk sample by 2-probe method concurrently with electrical resistivity by 4-probe method in the temperature range 300 – 1000 K," *Measurement*, vol. 91, pp. 613–619, 2016.

[30] S. Li and C. Persson, "Thermal Properties and Phonon Dispersion of Bi2Te3 and CsBi4Te6 from First-Principles Calculations," *Appl. Math. Phys.*, vol. 3, pp. 1563–1570, 2015.

[31] H. Wu, P. Wei, H. Cheng, J. Deng, and Y. Chen, "Ultralow thermal conductivity in n - type Ge-doped AgBiSe 2 thermoelectric materials," *Acta Mater.*, vol. 141, pp. 217–229, 2017.

[32] H. Wu and W. Yen, "High thermoelectric performance in Cu-doped Bi2Te3 with carrier-type transition," *Acta Mater.*, vol. 157, pp. 33–41, 2018.

[33] Z. L. Wang, T. Onda, Z. C. Chen, and T. Akao, "Microstructure and thermoelectric properties of Bi-Sb-Te bulk materials fabricated from rapidly solidified powders," *Scr. Mater.*, vol. 136, pp. 111–114, 2017.

[34] H. J. Goldsmid, "Bismuth telluride and its alloys as materials for thermoelectric generation," *Materials (Basel).*, vol. 7, no. 4, pp. 2577–2592, 2014.

[35] S. V. Faleev and F. Léonard, "Theory of enhancement of thermoelectric properties of materials with nanoinclusions," *Phys. Rev. B - Condens. Matter Mater. Phys.*, vol. 77, no. 21, pp. 1–9, 2008.

[36] X. H. Ji, X. B. Zhao, Y. H. Zhang, B. H. Lu, and H. L. Ni, "Synthesis and properties of rare earth containing Bi 2 Te 3 based thermoelectric alloys," *J. Alloys Compd.*, vol. 387, pp. 282–286, 2005.

[37] C. Zhou and L. Li, "Electronic structures and thermoelectric properties of La or Ce-doped Bi 2 Te 3 alloys from fi rst principles calculations," *J. Phys. Chem. Solids*, vol. 85, pp. 239–244, 2015.

[38] M. S. Dresselhaus *et al.*, "New directions for low-dimensional thermoelectric materials," *Adv. Mater.*, vol. 19, no. 8, pp. 1043–1053, 2007.

[39] Y. Liu, M. Zhou, and J. He, "Towards higher thermoelectric performance of Bi 2 Te 3 via defect engineering," *Scr. Mater.*, vol. 111, pp. 39–43, 2016.

[40] H. Fang, T. Feng, H. Yang, X. Ruan, and Y. Wu, "Synthesis and Thermoelectric Properties of Compositional- Modulated Lead Telluride − Bismuth Telluride Nanowire Heterostructures," *Nano Lett.*, vol. 13, p. 2058−2063, 2013.

[41] C. L. Chen *et al.*, "Fabrication and characterization of electrodeposited bismuth telluride films and nanowires," *J. Phys. Chem. C*, vol. 114, no. 8, pp. 3385–3389, 2010.

[42] M. Tan, Y. Hao, Y. Deng, and J. Chen, "High thermoelectric properties of (Sb,Bi)2Te3 nanowire arrays by tilt-structure engineering," *Appl. Surf. Sci.*, vol. 443, pp. 11–17, 2018.

[43] N. Mntungwa, P. V. S. R. Rajasekhar, K. Ramasamy, and N. Revaprasadu, "Superlattices and Microstructures A simple route to Bi 2 Se 3 and Bi 2 Te 3 nanocrystals," *Superlattices Microstruct.*, vol. 69, pp. 226–230, 2014.

[44] H. Xu and W. Wang, "Synthesis and Characterization of CNTs / Bi 2 Te 3 Thermoelectric Nanocomposites," *Int. J. Electrochem. Sci.*, vol. 8, pp. 6686–6691, 2013.

[45] F. Wu, H. Song, J. Jia, and X. Hu, "Effects of Ce, Y, and Sm doping on the thermoelectric properties of Bi2Te3alloy," *Prog. Nat. Sci. Mater. Int.*, vol. 23, no. 4, pp. 408–412, 2013.

[46] F. Wu, W. Wang, X. Hu, and M. Tang, "Thermoelectric properties of I-doped n-type Bi 2 Te 3 -based material prepared by hydrothermal and subsequent hot pressing," *Prog. Nat. Sci. Mater. Int.*, vol. 27, no. 2, pp. 203–207, 2017.

[47] K. Ahmad and C. Wan, "Enhanced thermoelectric performance of Bi 2 Te 3 through uniform dispersion of single wall carbon nanotubes," *Nanotechnology*, vol. 28, p. 415402, 2017.

[48] X. Qi, W. Ma, X. Zhang, and C. Zhang, "Raman characterization and transport properties of morphology-dependent two-dimensional Bi 2 Te 3 nano fi lms," *Appl. Surf. Sci.*, vol. 457, pp. 41–48, 2018.

[49] T. Ludwig *et al.*, "Mechanism of bismuth telluride exfoliation in an ionic liquid solvent," *Langmuir*, vol. 31, no. 12, pp. 3644–3652, 2015.

[50] Y. Q. Cao, T. J. Zhu, and X. B. Zhao, "Thermoelectric Bi2Te3nanotubes synthesized by low-temperature aqueous chemical method," *J. Alloys Compd.*, vol. 449, no. 1–2, pp. 109–112, 2008.

[51] M. T. Pettes, J. Maassen, I. Jo, M. S. Lundstrom, and L. Shi, "Effects of surface band bending and scattering on thermoelectric transport in suspended bismuth telluride nanoplates," *Nano Lett.*, vol. 13, no. 11, pp. 5316–5322, 2013.

[52] Y. Zhao, R. W. Hughes, Z. Su, W. Zhou, and D. H. Gregory, "One-step synthesis of

bismuth telluride nanosheets of a few quintuple layers in thickness," *Angew. Chemie - Int. Ed.*, vol. 50, no. 44, pp. 10397–10401, 2011.

[53] X. B. Zhao, X. H. Ji, Y. H. Zhang, T. J. Zhu, J. P. Tu, and X. B. Zhang, "Bismuth telluride nanotubes and the effects on the thermoelectric properties of nanotube-containing nanocomposites," *Appl. Phys. Lett.*, vol. 86, no. 6, pp. 1–3, 2005.

[54] I. Bejenari, V. Kantser, and A. A. Balandin, "Thermoelectric properties of electrically gated bismuth telluride nanowires," *Phys. Rev. B - Condens. Matter Mater. Phys.*, vol. 81, no. 7, pp. 1–14, 2010.

[55] D. Kong *et al.*, "Few-layer nanoplates of Bi2Se3and Bi2Te3with highly tunable chemical potential," *Nano Lett.*, vol. 10, no. 6, pp. 2245–2250, 2010.

[56] Y. H. Zhang, T. J. Zhu, J. P. Tu, and X. B. Zhao, "Flower-like nanostructure and thermoelectric properties of hydrothermally synthesized La-containing Bi2Te3based alloys," *Mater. Chem. Phys.*, vol. 103, no. 2–3, pp. 484–488, 2007.

[57] F. Ren, H. Wang, P. A. Menchhofer, and J. O. Kiggans, "Thermoelectric and mechanical properties of multi-walled carbon nanotube doped $Bi_{0.4}Sb_{1.6}Te_3$ thermoelectric material," *Appl. Phys. Lett.*, vol. 103, no. 22, p. 221907, 2013.

[58] Y. Q. Cao, T. J. Zhu, X. B. Zhao, X. B. Zhang, and J. P. Tu, "Nanostructuring and improved performance of ternary Bi-Sb-Te thermoelectric materials," *Appl. Phys. A Mater. Sci. Process.*, vol. 92, no. 2, pp. 321–324, 2008.

[59] B. Poudel *et al.*, "High-Thermoelectric Performance of Nanostructured Bismuth Antimony Telluride Bulk Allys," *Sci.* , vol. 320, no. 5876, pp. 634–638, 2008.

[60] X. Tang, W. Xie, H. Li, W. Zhao, Q. Zhang, and M. Niino, "Preparation and thermoelectric transport properties of high-performance p-type Bi2Te3 with layered nanostructure," *Appl. Phys. Lett.*, vol. 90, no. 1, pp. 1–4, 2007.

[61] J. He, S. N. Girard, J. C. Zheng, L. Zhao, M. G. Kanatzidis, and V. P. Dravid, "Strong phonon scattering by layer structured PbSnS2 in PbTe based thermoelectric materials," *Adv. Mater.*, vol. 24, no. 32, pp. 4440–4444, 2012.

[62] J. He *et al.*, "On the origin of increased phonon scattering in nanostructured pbte based thermoelectric materials," *J. Am. Chem. Soc.*, vol. 132, no. 25, pp. 8669–8675, 2010.

[63] A. I. Hochbaum *et al.*, "Enhanced thermoelectric performance of rough silicon nanowires," *Nature*, vol. 451, no. 7175, pp. 163–167, 2008.

[64] K. Biswas *et al.*, "Strained endotaxial nanostructures with high thermoelectric figure of merit," *Nat. Chem.*, vol. 3, no. 2, pp. 160–166, 2011.

[65] J. Jaćimović *et al.*, "Synthesis, electrical resistivity, thermo-electric power and

magnetization of cubic ZnMnO3," *Solid State Commun.*, vol. 151, no. 6, pp. 487–490, 2011.

[66] H. Karamitaheri, M. Pourfath, M. Pazoki, R. Faez, and H. Kosina, "Graphene-Based Antidots for Thermoelectric Applications," *J. Electrochem. Soc.*, vol. 158, no. 12, p. K213, 2011.

[67] M. Tan, Y. Deng, and Y. Wang, "Ordered structure and high thermoelectric properties of Bi2(Te,Se)3nanowire array," *Nano Energy*, vol. 3, pp. 144–151, 2014.

[68] H. Bark, J.-S. Kim, H. Kim, J.-H. Yim, and H. Lee, "Effect of multiwalled carbon nanotubes on the thermoelectric properties of a bismuth telluride matrix," *Curr. Appl. Phys.*, vol. 13, pp. S111–S114, 2013.

[69] J. Hwang, J. Kim, H. Kim, S. Kim, and K. H. Lee, "Effect of Dislocation Arrays at Grain Boundaries on Electronic Transport Properties of Bismuth Antimony Telluride : Unified Strategy for High Thermoelectric Performance," *Adv. Energy Mater.*, vol. 8, p. 1800065, 2018.

[70] P. Srivastava and K. Singh, "Graphene-Like Bismuth Telluride Nanostructures : Template-Free Solvothermal Synthesis and Characterizations," *Nanosci. Nanotechnol. Lett.*, vol. 4, pp. 1177–1180, 2012.

[71] W. Liu, J. Hu, S. Zhang, M. Deng, C.-G. Han, and Y. Liu, "New trends, strategies and opportunities in thermoelectric materials: A perspective," *Mater. Today Phys.*, vol. 1, pp. 50–60, 2017.

[72] C. Yu, S. Hyun, S. Yeol, J. Ryoun, and Y. Seok, "Graphene embedded form stable phase change materials for drawing the thermo-electric energy harvesting," *Energy Convers. Manag.*, vol. 169, pp. 88–96, 2018.

[73] H. Ju and J. Kim, "The effect of temperature on thermoelectric properties of n-type Bi_2Te_3 nanowire/graphene layer-by-layer hybrid composites," *Dalt. Trans.*, vol. 44, no. 26, pp. 11755–11762, 2015.

[74] F. Tu, J. Xie, G. Cao, and X. Zhao, "Self-Assembly of Bi 2Te 3-nanoplate/graphene-nanosheet hybrid by one-pot route and its improved Li-storage properties," *Materials (Basel).*, vol. 5, no. 7, pp. 1275–1284, 2012.

[75] D. Suh, S. Lee, and H. Mun, "Enhanced thermoelectric performance of Bi0.5Sb1.5Te3-expanded graphene composites by simultaneous modulation of electronic and thermal carrier transport," *Nano Energy*, 2015.

[76] A. H. Li *et al.*, "Electronic structure and thermoelectric properties of Bi2Te3crystals and graphene-doped Bi2Te3," *Thin Solid Films*, vol. 518, no. 24 SUPPL., pp. 57–60, 2010.

[77] B. Feng, J. Xie, G. Cao, T. Zhu, and X. Zhao, "Enhanced thermoelectric properties of p-

type CoSb3/graphene nano composite," *J. Mater. Chem. A*, vol. 1, pp. 13111–13119, 2013.

[78] B. Liang, Z. Song, M. Wang, L. Wang, and W. Jiang, "Fabrication and Thermoelectric Properties of Graphene / Bi 2 Te 3 Composite Materials," *J. nano Mater.*, vol. 2013, pp. 210767, 5, 2013.

[79] C. Li *et al.*, "Simultaneous increase in conductivity and phonon scattering in a graphene nanosheets/(Bi2Te3)0.2(Sb2Te3)0.8thermoelectric nanocomposite," *J. Alloys Compd.*, vol. 661, pp. 389–395, 2016.

[80] E. S. Kim, J. Hwang, K. H. Lee, H. Ohta, and Y. H. Lee, "Graphene Substrate for van der Waals Epitaxy of Layer-Structured Bismuth Antimony Telluride Thermoelectric Film," *Adv. Mater.*, vol. 29, p. 1604899, 2017.

[81] C. W. Lee *et al.*, "Improvement of thermoelectric properties of Bi2Te3 and Sb2Te3 films grown on graphene substrate," *Phys. Status Solidi - Rapid Res. Lett.*, vol. 1700029, no. 6, pp. 2–5, 2017.

[82] J. Dong, W. Liu, H. Li, X. Su, X. Tang, and C. Uher, "In situ synthesis and thermoelectric properties of PbTe – graphene nanocomposites by utilizing a facile and novel wet chemical method," *J. Mater. Chem. A*, vol. 1, pp. 12503–12511, 2013.

[83] H. Ju, M. Kim, and J. Kim, "Preparation of graphene sheets into one-dimensionally nanostructured bulk bismuth telluride for enhancing thermoelectric power factor," *J. Mater. Sci. Mater. Electron.*, vol. 27, no. 4, pp. 3427–3434, 2016.

[84] T. Chen, P. Chen, and C. Chen, "Laser co-ablation of bismuth antimony telluride and diamond-like carbon nanocomposites for enhanced thermoelectric performance," *J. Mater. Chem. A*, vol. 6, pp. 982–990, 2018.

[85] W. Ho *et al.*, "Enhanced thermoelectric performance of reduced graphene oxide incorporated bismuth-antimony-telluride by lattice thermal conductivity reduction," *J. Alloys Compd.*, vol. 718, pp. 342–348, 2017.

[86] B. Trawiński, B. Bochentyn, N. Gostkowska, M. Łapiński, T. Miruszewski, and B. Kusz, "Structure and thermoelectric properties of bismuth telluride—Carbon composites," *Mater. Res. Bull.*, vol. 99, pp. 10–17, 2018.

[87] K. Agarwal, V. Kaushik, D. Varandani, A. Dhar, and B. R. Mehta, "Nanoscale thermoelectric properties of Bi2Te3-Graphene nanocomposites: conducting atomic force, scanning thermal and kelvin probe microscopy studies," *J. Alloys Compd.*, vol. 16, 2016.

[88] and A. A.-M. Mohamed S. El-Asfoury Mohamed N. A. Nasr, Koichi Nakamura, "Thermoelectric power factor performance of Bi85Sb15/graphene composite," *Jpn. J. Appl. Phys.*, vol. 55, p. 45802, 2016.

[89] H. Ju and J. Kim, "Preparation and structure dependent thermoelectric properties of nanostructured bulk bismuth telluride with graphene," *J. Alloys Compd.*, vol. 664, pp. 639–647, 2016.

[90] J. Il Kim, E. S. Lee, J. Y. Kim, S. M. Choi, K. H. Lee, and W. S. Seo, "Thermoelectric properties of unoxidized graphene/Bi2Te2.7Se0.3composites synthesized by exfoliation/re-assembly method," *Phys. Status Solidi - Rapid Res. Lett.*, vol. 8, no. 4, pp. 357–361, 2014.

[91] V. D. Blank *et al.*, "Thermoelectric properties of Bi0.5Sb1.5Te3/C60 nanocomposites," *Phys. Rev. B*, vol. 75426, pp. 1–8, 2012.

[92] H. Ju, M. Kim, and J. Kim, "A facile fabrication of n-type Bi 2 Te 3 nanowire / graphene layer-by-layer hybrid structures and their improved thermoelectric performance," *Chem. Eng. J.*, vol. 275, pp. 102–112, 2015.

[93] D. Xie and J. Xu, "Synergistic Optimization of Thermoelectric," *energies*, pp. 1–9, 2016.

[94] A. A. A. Rahman, A. A. Umar, X. Chen, M. M. Salleh, and M. Oyama, "Enhanced thermoelectric properties of bismuth telluride–organic hybrid films via graphene doping," *Appl. Phys. A Mater. Sci. Process.*, vol. 122, no. 2, pp. 1–8, 2016.

[95] R. R. Y. and N. K. sunil kumar, simrjit singh, punit kumar dhawan, "Effect of Graphene nanofillers on the enhanced thermoelectric properties of Bi2Te3 nanosheets: Elucidating the role of interface in de-coupling the electrical and thermal characteristics," *Nanotechnology*, 2018.

[96] B. Y. Lan, A. J. Minnich, G. Chen, and Z. Ren, "Enhancement of Thermoelectric Figure-of-Merit by a Bulk Nanostructuring Approach," *Adv. Funct. Mater.*, vol. 2, pp. 357–376, 2010.

[97] M. Hajji, H. Absike, H. Labrim, H. Ez-zahraouy, M. Benaissa, and A. Benyoussef, "Strain effects on the electronic and thermoelectric properties of Bi2Te3 : A fi rst principles study," *Comput. Condens. Matter*, vol. 16, p. e00299, 2018.

[98] D. Li, R. Sun, and X. Qin, "Improving thermoelectric properties of p-type Bi 2 Te 3 - based alloys by spark plasma sintering," *Prog. Nat. Sci. Mater. Int.*, vol. 21, pp. 336–340, 2011.

[99] E. Song *et al.*, "Manipulating thermal and electronic transports in thermoelectric Bi2Te3 nanowires by porphyrin adsorption," *AIP Adv.*, vol. 8, p. 105010, 2018.

[100] H. Fang and Y. Wu, "Telluride nanowire and nanowire heterostructure- based thermoelectric energy harvesting," *Mater. Chem. A*, vol. 2, pp. 6004–6014, 2014.

[101] A. Danine, K. Termentzidis, S. Schaefer, S. Li, W. Ensinger, and C. Boulanger, "Synthesis of bismuth telluride nanotubes and their simulated thermal properties,"

Superlattices Microstruct., vol. 122, pp. 587–595, 2018.

[102] J. A. Martinez, P. P. Provencio, S. T. Picraux, J. P. Sullivan, and B. S. Swartzentruber, "Enhanced thermoelectric figure of merit in SiGe alloy nanowires by boundary and hole-phonon scattering," *Appl. Phys.*, vol. 110, p. 74317, 2011.

[103] S. Fan, J. Zhao, J. Guo, Q. Yan, J. Ma, and H. H. Hng, "p-type bi0.4sb1.6Te3 nanocomposites with enhanced figure of merit," *Appl. Phys. Lett.*, vol. 96, p. 182104, 2010.

[104] H. Y. Lv, H. J. Liu, J. Shi, X. F. Tang, and C. Uher, "Optimized thermoelectric performance of Bi2Te3 nanowires," *J. Mater. Chem. A*, vol. 1, pp. 6831–6838, 2013.

[105] Y. Luo *et al.*, "n-Type SnSe 2 Oriented-Nanoplate-Based Pellets for High Thermoelectric Performance," *Adv. Energy Mater.*, vol. 8, p. 1702167(1 to 6), 2018.

[106] G. J. S. and J. Z. Min Hong, Thomas C. Chasapis, Zhi-Gang Chen, Lei Yang, Mercouri G. Kanatzidis, "n-Type Bi2Te3−Se Nanoplates with Enhanced Thermoelectric Efficiency Driven by Wide- Frequency Phonon Scatterings and Synergistic Carrier Scatterings," *ACS Nano*, vol. 10, pp. 4719–4727, 2016.

[107] Z. Chen, G. Han, L. Yang, L. Cheng, and J. Zou, "Nanostructured thermoelectric materials : Current research and future challenge," *Prog. Nat. Sci. Mater. Int.*, vol. 22, no. 6, pp. 535–549, 2012.

[108] V. A. Online, W. Shi, S. Yu, P. Liu, and W. Fan, "Hydrothermal synthesis and thermoelectric transport properties of Sb2Te3 –Te heterogeneous nanostructures," *crystengcomm*, vol. 15, pp. 2978–2985, 2013.

[109] Y. Liu, Q. Wang, J. Pan, Y. Sun, L. Zhang, and S. Song, "Hierarchical Bi 2 Te 3 Nanostrings : Green Synthesis and Their Thermoelectric Properties," *Nano Lett.*, vol. 24, pp. 9765–9768, 2018.

[110] M. Hong, Z. Chen, L. Yang, and J. Zou, "Enhancing thermoelectric performance of Bi2Te3-based nanostructures through rational structure design," *Nanoscale*, vol. 8, pp. 8681–8686, 2016.

[111] H. He, D. Huang, X. Zhang, and G. Li, "Characterization of hexagonal Bi2Te3 nanosheets prepared by solvothermal method," *Solid State Commun.*, vol. 152, no. 9, pp. 810–815, 2012.

[112] S. Vinoth, T. Balaganapathi, B. Kaniamuthan, T. Arun, and I. P. Muthuselvam, "Bi2Te3 thin hexagonal nanoplatelets : Synthesis and its characterization studies," *Phys. E Low-dimensional Syst. Nanostructures*, vol. 92, no. April, pp. 17–22, 2017.

[113] R. Gunda, B. Suresh, M. Raj, and K. Dash, "Synthesis of graphene oxide and reduced graphene oxide using volumetric method by a novel approach without - NaNO2 or -

NaNO3," *Appl. Nanosci.*, 2018.

[114] D. B. Dommisa and R. K. Dash, "Effect of the precursor graphite on the structure and morphology of graphite oxide and reduced graphene oxide," *Adv. Mater. Lett.*, vol. 8, no. 3, pp. 315–321, 2017.

[115] A. C. Ferrari *et al.*, "Raman Spectrum of Graphene and Graphene Layers," *Phys. Rev. Lett.*, vol. 97, p. 187401, 2006.

[116] B. D. CULLITY, *ELEMENTS OF X-RAY DIFFRACTION*. Notre Dame, Indiana: ADDISON-WESLY PUBLISHING COMPANY, Inc., 1956.

[117] Y. Feutelais, B. Legendre, N. Rodier, and V. Agafonov, "A study of the phases in the bismuth-tellurium system," *Mater. Res. Bull.*, vol. 28, no. c, pp. 591–596, 1993.

[118] P. Srivastava and K. Singh, "Low temperature reduction route to synthesise bismuth telluride (Bi2Te3) nanoparticles : structural and optical studies," *J. Exp. Nanosci.*, vol. 9, no. 10, pp. 1064–1074, 2014.

[119] M. Han, Y. Jin, D.-H. Lee, and S.-J. Kim, "Thermoelectric Properties of Bi 2 Te 3 : CuI and the Effect of Its Doping with Pb Atoms," *Materials (Basel).*, vol. 10, p. 1235, 2017.

[120] G. D. Mahan, L. Lindsay, and D. A. Broido, "The Seebeck coefficient and phonon drag in silicon," *Appl. Phys.*, vol. 116, p. 245102, 2014.

[121] "www.hotdiskinstruments.com." .

[122] D. Song, W. Ma, and X. Zhang, "Lattice thermal conductivity of Si / Ge composite thermoelectric material : Effect of Si particle distribution," *Int. J. energy Res.*, vol. 43, pp. 379–390, 2019.

[123] Z. Y. Zhang, C. H. Jin, X. L. Liang, Q. Chen, and L. M. Peng, "Current-voltage characteristics and parameter retrieval of semiconducting nanowires," *Appl. Phys. Lett.*, vol. 88, p. 73102, 2006.

[124] A. Bar-Lev, *Semiconductors and electronic devices*. 1984.

[125] L. D. Hicks, "Thermoelectric figure of merit of a one-dimensional conductor," *Phys. Rev. B*, vol. 47, no. 24, pp. 8–11, 1993.

Development of Graphene-Bismuth telluride based nanostructured materials for thermoelectric energy harvesting

by Naveen Nischal Pillala

Development of Graphene-Bismuth telluride based nanostructured materials for thermoelectric energy harvesting

ORIGINALITY REPORT

8%	3%	5%	7%
SIMILARITY INDEX	INTERNET SOURCES	PUBLICATIONS	STUDENT PAPERS

PRIMARY SOURCES

1	worldwidescience.org Internet Source	1%
2	Submitted to Indian Institute of Science, Bangalore Student Paper	<1%
3	www.ijert.org Internet Source	<1%
4	Submitted to Queen Mary and Westfield College Student Paper	<1%
5	K.N. Venkatachalaiah, H. Nagabhushana, G.P. Darshan, R.B. Basavaraj, B. Daruka Prasad, S.C. Sharma. "Blue light emitting Y 2 O 3 :Tm 3+ nanophosphors with tunable morphology obtained by bio-surfactant assisted sonochemical route", Spectrochimica Acta Part A: Molecular and Biomolecular Spectroscopy, 2017 Publication	<1%
	Submitted to UT, Dallas	

6	Student Paper	<1%
7	A. Selvakumar, P. V. Mohanram. "Analysis of effective thermal conductivity for mineral cast material structures with varying epoxy content using TPS method", Materials Research, 2012 Publication	<1%
8	res.mdpi.com Internet Source	<1%
9	Submitted to Indian Institute of Technology, Kanpur Student Paper	<1%
10	Submitted to SASTRA University Student Paper	<1%
11	dlib.bc.edu Internet Source	<1%
12	Submitted to Higher Education Commission Pakistan Student Paper	<1%
13	Hong-xia Liu, Shu-ping Deng, De-cong Li, Lan-xian Shen, Shu-kang Deng. " Thermal stability and electrical transport properties of Ge/Sn-codoped single crystalline -Zn Sb prepared by the Sn-flux method ", Chinese Physics B, 2017 Publication	<1%

14	M.Y. Cui, X.Q. Yao, W.J. Dong, K. Tsukamoto, C.R. Li. "Template-free synthesis of CuO–CeO2 nanowires by hydrothermal technology", Journal of Crystal Growth, 2010 Publication	<1%
15	Atchudan, Raji, Thomas Nesakumar Jebakumar Immanuel Edison, Suguna Perumal, Dhanapalan Karthikeyan, and Yong Rok Lee. "Facile synthesis of zinc oxide nanoparticles decorated graphene oxide composite via simple solvothermal route and their photocatalytic activity on methylene blue degradation", Journal of Photochemistry and Photobiology B Biology, 2016. Publication	<1%
16	Submitted to Indian Institute of Technology, Madras Student Paper	<1%
17	Submitted to Thapar University, Patiala Student Paper	<1%
18	Submitted to BITS, Pilani-Dubai Student Paper	<1%
19	Submitted to Texas Christian University Student Paper	<1%
20	Y. Xu, Z.W. Liu, Y.L. Xu, Y.Y. Zhang, J.L. Wu. "Preparation and characterisation of	<1%

graphene/ZnS nanocomposites via a surfactant-free method", Journal of Experimental Nanoscience, 2012
Publication

---

21 Sarkardei, S.. "The effects of freeze-drying and storage on the FT-Raman spectra of Atlantic mackerel (Scomber scombrus) and horse mackerel (Trachurus trachurus)", Food Chemistry, 2007 <1%
Publication

---

22 Ashis K. Sarker, Jong-Dal Hong. "Layer-by-Layer Self-Assembled Multilayer Films Composed of Graphene/Polyaniline Bilayers: High-Energy Electrode Materials for Supercapacitors", Langmuir, 2012 <1%
Publication

---

23 Thiagarajan, Suraj Joottu, Wei Wang, and Ronggui Yang. "NANOCOMPOSITES AS HIGH EFFICIENCY THERMOELECTRIC MATERIALS", Annual Review of Nano Research, 2009. <1%
Publication

---

24 Sunil Kumar, Simrjit Singh, Punit Kumar Dhawan, R R Yadav, Neeraj Khare. " Effect of graphene nanofillers on the enhanced thermoelectric properties of Bi Te nanosheets: elucidating the role of interface in de-coupling <1%

the electrical and thermal characteristics ", Nanotechnology, 2018
Publication

---

25 Daniyal Younas, Qurat-ul-Ain Javed, Sabeen Fatima, Riffat Kalsoom, Hussain Abbas, Yaqoob Khan. "Drude conductivity exhibited by chemically synthesized reduced graphene oxide", Materials Research Express, 2017 <1%
Publication

---

26 "Development of Thermoelectric Technology from Materials to Generators", Advanced Materials for Clean Energy, 2015. <1%
Publication

---

27 Khalid Bin Masood, Pushpendra Kumar, jai singh, R. A. Singh. "Odyssey of thermoelectric materials: foundation of the complex structure", Journal of Physics Communications, 2018 <1%
Publication

---

28 Submitted to Kookmin University <1%
Student Paper

---

29 Chahrour, Khaled M., Naser M. Ahmed, M.R. Hashim, Nezar G. Elfadill, W. Maryam, M.A. Ahmad, and M. Bououdina. "Effects of the voltage and time of anodization on modulation of the pore dimensions of AAO films for nanomaterials synthesis", Superlattices and Microstructures, 2015. <1%

	Publication	
30	Jinfeng Han, Ying Ha, Mingyu Guo, Peipei Zhao, Qingling Liu, Caixia Liu, Chunfeng Song, Na Ji, Xuebin Lu, Degang Ma, Zhenguo Li. "Synthesis of zeolite SSZ-13 from coal gangue via ultrasonic pretreatment combined with hydrothermal growth method", Ultrasonics Sonochemistry, 2019 Publication	<1%
31	Submitted to King Saud University Student Paper	<1%
32	mdpi.com Internet Source	<1%
33	mrs.org Internet Source	<1%
34	www.arredobagno360.it Internet Source	<1%
35	Izhar-Ul-Haq. "Simultaneous measurement of thermal conductivity and thermal diffusivity of rock-marbles using transient plane source (TPS) technique", Heat Recovery Systems and CHP, 1991 Publication	<1%
36	www.scribd.com Internet Source	<1%

37	Bartosz Trawiński, Beata Bochentyn, Natalia Gostkowska, Marcin Łapiński, Tadeusz Miruszewski, Bogusław Kusz. "Structure and thermoelectric properties of bismuth telluride—Carbon composites", Materials Research Bulletin, 2018 Publication	<1%
38	Mingzhi Yu. "Influence of moisture content on measurement accuracy of porous media thermal conductivity", Heat Transfer-Asian Research, 2009 Publication	<1%
39	Flavio Pendolino, Nerina Armata. "Graphene Oxide in Environmental Remediation Process", Springer Science and Business Media LLC, 2017 Publication	<1%
40	Airul Azha Abd Rahman, Akrajas Ali Umar, Xiaomei Chen, Muhamad Mat Salleh, Munetaka Oyama. "Enhanced thermoelectric properties of bismuth telluride–organic hybrid films via graphene doping", Applied Physics A, 2016 Publication	<1%
41	Submitted to Imperial College of Science, Technology and Medicine Student Paper	<1%
	Fu Li, Jing-Feng Li, Jian-Hui Li, Fang-Zhou Yao.	

42	"The effect of Cu substitution on microstructure and thermoelectric properties of LaCoO3 ceramics", Physical Chemistry Chemical Physics, 2012 Publication	<1%
43	sustainenvironres.biomedcentral.com Internet Source	<1%
44	Submitted to University of Ulster Student Paper	<1%
45	Lingzhu Yu, Lichun Zhang, Hongjie Song, Xiaoming Jiang, Yi Lv. "Hierarchical SnO2 architectures: controllable growth on graphene by atmospheric pressure chemical vapour deposition and application in cataluminescence gas sensor", CrystEngComm, 2014 Publication	<1%
46	Submitted to Universiti Sains Islam Malaysia Student Paper	<1%
47	Submitted to Jawaharlal Nehru University (JNU) Student Paper	<1%
48	Submitted to University of Central Florida Student Paper	<1%
49	link.springer.com Internet Source	<1%
50	Lusheng Su, Yong X.. "Chapter 6 Advances in	<1%

Thermoelectric Energy Conversion Nanocomposites", IntechOpen, 2011

Publication

Exclude quotes	On	Exclude matches	< 14 words
Exclude bibliography	On		